

# Identifying compact symmetric objects with high-precision VLBI and *Gaia* astrometry

T. An<sup>1,★</sup>, Y. Zhang<sup>1</sup>, S. Frey<sup>2,3,4</sup>, W.A. Baan<sup>5,1,6</sup> and A. Wang<sup>1</sup>

<sup>1</sup> Shanghai Astronomical Observatory, Key Laboratory of Radio Astronomy, CAS, 80 Nandan Road, Shanghai 200030, China

<sup>2</sup> Konkoly Observatory, HUN-REN Research Centre for Astronomy and Earth Sciences, Konkoly Thege Miklós út 15-17, H-1121 Budapest, Hungary

<sup>3</sup> CSFK, MTA Centre of Excellence, Konkoly Thege Miklós út 15-17, H-1121 Budapest, Hungary

<sup>4</sup> Institute of Physics and Astronomy, ELTE Eötvös Loránd University, Pázmány Péter sétány 1/A, H-1117 Budapest, Hungary

<sup>5</sup> Xinjiang Astronomical Observatory, CAS, 150 Science-1 Street, Ürümqi, Xinjiang 830011, P.R. China

<sup>6</sup> Netherlands Institute for Radio Astronomy, ASTRON, Oude Hoogeveensedijk 4, 7991PD Dwingeloo, The Netherlands

Received 2025; accepted 2025

## ABSTRACT

**Context.** Compact symmetric objects (CSOs) represent a key early stage in the evolution of radio galaxies, but their reliable identification is challenging due to the difficulty of detecting their radio cores and distinguishing them from other compact radio sources.

**Aims.** We develop and validate a new method to unambiguously identify CSOs by combining *Gaia*'s high-precision optical astrometry with the high-resolution radio imaging of very long baseline interferometry (VLBI).

**Methods.** We analyze 40 CSO candidates by overlaying *Gaia* DR3 positions on VLBI maps to pinpoint their central engines. CSOs are confirmed when their *Gaia* positions lie between symmetric radio lobes. In contrast, core-jet sources are identified when the optical position coincides with one end of the radio structure. To verify CSO classifications, we also analyze spectral index maps, source variability, and jet kinematics using multi-epoch VLBI observations spanning up to 25 years.

**Results.** Our method successfully identified 22 genuine CSOs and 10 core-jet sources, while 8 other objects remain ambiguous due to significant optical-radio positional offsets. The confirmed CSOs display diverse properties, with kinematic ages ranging from 20 years to over 1000 years, and hotspot advance speeds typically below  $0.5 c$ , although some sources show mildly relativistic expansion. Their spectral and variability characteristics support classification as young, evolving radio galaxies. Notably, five nearby CSOs show systematic optical-radio offsets despite strong CSO morphological evidence, highlighting the influence of the host galaxy environment.

**Conclusions.** The *Gaia*-VLBI method provides a powerful new tool for reliably identifying CSOs. Our sample reveals a diverse distribution of radio powers, confirming both high-power and low-power CSOs and suggesting the existence of multiple evolutionary paths. High-power CSOs may evolve into large-scale radio galaxies, while many low-power CSOs show evidence of being confined by their host galaxy environments. Our findings suggest that CSO evolution is not only affected by the intrinsic jet power but also by environment, the duration and sustainability of the central engine activity. Future high-sensitivity observations of low-power CSOs are crucial for understanding the full range of formation mechanisms and evolutionary paths of radio galaxies.

**Key words.** galaxies: active — galaxies: nuclei — galaxies: jets — quasars: general — radio continuum: galaxies — astrometry

## 1. Introduction

Compact symmetric objects (CSOs) represent a key early stage in radio galaxy evolution, characterized by symmetric double-loped morphology within a projected size of  $\lesssim 1$  kiloparsec (kpc) (Phillips & Mutel 1980, 1982; Pearson & Readhead 1981, 1988). These compact radio sources offer unique insights into the complex interplay between active galactic nuclei (AGN) activity and their host environments and have become laboratories for studying jet-ISM interactions and AGN feedback mechanisms (Tadhunter 2016; Bicknell et al. 2018; O'Dea & Saikia 2021).

The physical nature of CSOs has been debated through three primary theoretical frameworks. The *Young Radio Galaxy Model* suggests CSOs represent the earliest evolutionary stage of radio galaxies (e.g. Phillips & Mutel 1980; Readhead et al. 1996a; Owsianik & Conway 1998), supported by the observed “luminosity-size” relationship (Baldwin 1982) that indicates progression from CSOs to larger-scale radio sources (e.g. Fanti

et al. 1995; Snellen et al. 2000; Kunert-Bajraszewska et al. 2010; An & Baan 2012). However, this evolutionary path may account for only a small fraction of the overall CSO population, primarily those with high-power jets, while the fate of those with lower-power and unstable jets is uncertain.

The *Frustrated Radio Galaxy Model* proposes that CSOs are impeded by dense interstellar medium (ISM) in their host galaxies (e.g. van Breugel et al. 1984; Wilkinson et al. 1984; O'Dea et al. 1991; De Young 1993), particularly relevant for low-radio-power sources that may never evolve into Fanaroff–Riley type I or II radio galaxies (Fanaroff & Riley 1974). Recent observations of FR 0 radio galaxies (Baldi et al. 2018, 2019) and even lower-power radio sources (Chilufya et al. 2024) suggest a potential link to previously unexplored low-power CSO population, where jet-ISM interactions significantly shape radio morphology.

The *Transient Phenomenon Model* suggests some CSOs may be short-lived, resulting from intermittent or episodic AGN activity. Here, it is important to distinguish between “intermittent” activity (repeating cycles caused by accretion disk instabilities,

\* Corresponding author: antao@shao.ac.cn

e.g., Janiuk et al. 2002; Czerny et al. 2009; Siemiginowska et al. 2010; Wu 2009) and “episodic” events (one-time phenomena such as tidal disruption events, TDEs, Readhead et al. 1996b, 2024). While this episodic TDE model can explain certain short-lived sources, it struggles to account for CSOs that evolve into larger radio galaxies or show multiple activity episodes (e.g. Schoenmakers et al. 2000; Kaiser et al. 2000; Marecki & Szablewski 2009; Joshi et al. 2011; Mahatma et al. 2019; Orienti et al. 2023). The presence of double-double radio lobes or remnant emission suggests that CSOs may undergo recurrent activity cycles (Machalski et al. 2010; Konar & Hardcastle 2013), necessitating models that can explain both transient and long-term evolutionary processes.

To connect our understanding of radio galaxy formation, precise quantification of CSO dynamics, ages, and triggering rates is crucial to establish their relationship to large-scale radio galaxies. CSOs provide unique insights into the birth and evolution of radio galaxies through several key aspects: their compact size and youth provide direct windows into early-stage jet activity and jet–ISM interactions, while their symmetric double-lobed morphology, typically oriented close to the sky plane, minimizes relativistic beaming effects and reveals intrinsic jet properties.

CSOs are particularly critical to understanding AGN feedback mechanisms and galaxy evolution. They serve as laboratories for studying three critical processes: initial jet–ISM coupling in galactic nuclei, jet physics with minimal projection effects, and diverse evolutionary pathways spanning from high-power sources evolving into large radio galaxies to confined low-power sources. These characteristics make CSOs fundamental to understanding how AGN feedback operates in practice and influences galaxy evolution across cosmic time.

Despite their importance, the identification and physical nature of CSOs remain challenging areas of investigation. The primary difficulty lies in detecting their radio cores, which are often weak or obscured (Gugliucci et al. 2005) due to several factors. First, minimal relativistic beaming effects due to large inclination angles result in reduced core emission (Peck et al. 1999; Orienti et al. 2006; Marr et al. 2001; Orienti & Dallacasa 2008; An et al. 2012; Wu et al. 2013). Second, dense ionized gas in nuclear regions can cause significant attenuation through synchrotron self-absorption or free-free absorption (O’Dea 1998; Fanti 2009). Third, frequency-dependent opacity effects can shift apparent core positions, complicating their identification in VLBI observations.

Traditional CSO identification has relied heavily on morphological and spectral criteria derived from high-resolution very long baseline interferometry (VLBI) observations. Key indicators include symmetric double-lobed structure, steep-spectrum lobes, and low variability (e.g., Taylor et al. 1996; Peck & Taylor 2000; Healey et al. 2007). However distinguishing genuine CSOs from core–jet sources exhibiting similar structures remains difficult in the absence of clear core detection. While radio spectral indices from multi-frequency VLBI observations provide supplementary evidence, uncertainties in the CSO variability, dynamics and life cycles limit our ability to construct complete, unbiased CSO samples.

To address these challenges, we introduce a new method that combines high-precision optical astrometry of the *Gaia* space mission (Gaia Collaboration et al. 2016) with high-resolution VLBI imaging to unambiguously identify genuine CSOs. *Gaia* Data Release 3 (DR3, Gaia Collaboration et al. 2023) provides unprecedented astrometric precision ( $\sim 0.04$  mas for bright sources with apparent optical magnitude  $G < 14^{\text{mag}}$ , and  $\sim 0.7$  mas at  $G = 20^{\text{mag}}$ ) for approximately 1.6 million quasar-like

objects. When overlaid on VLBI maps, these precise optical positions can effectively pinpoint AGN central engines, even when radio cores are weak or undetectable.

This study applies this method to 40 CSO candidates selected from existing VLBI surveys (see details in Section 2). By overlaying *Gaia* DR3 positions on multi-epoch, multi-frequency VLBI maps, we can definitively classify these objects and study their properties in unprecedented detail.

The structure of this paper is as follows: Section 3 presents the identification of CSOs and core–jet sources using the so-called *Gaia*+VLBI method. Section 4 discusses the radio properties of the confirmed CSOs. The results are summarized in Section 5. Throughout this paper, we assume a standard flat  $\Lambda$  Cold Dark Matter cosmology with  $H_0 = 70 \text{ km s}^{-1} \text{ Mpc}^{-1}$ ,  $\Omega_m = 0.3$ , and  $\Omega_\Lambda = 0.7$ .

## 2. Method and samples

### 2.1. CSO identification criteria

Traditional identification of CSOs relies on several key characteristics that distinguish them from other compact radio sources. These diagnostic criteria include:

- **Compact and symmetric radio structure:** projected linear size  $< 1 \text{ kpc}$ ; double lobes with symmetric brightness distribution (brightness ratio  $< 10:1$ ); lobes positioned on opposite sides of a central core, forming a mirror-symmetric appearance.
- **Spectral properties:** sources typically exhibit convex or steep radio spectrum, peaking at GHz frequencies; lobes have steep spectra (with power-law spectral index  $\alpha > 0.5$ , where  $S_\nu \propto \nu^{-\alpha}$ ); the core has a flat or inverted spectrum.
- **Low variability:** typical variability level  $< 20\%$ ;
- **Sub-relativistic hotspot advance speeds:** generally  $< 0.5 c$ , where  $c$  denotes the speed of light.

However, comprehensive data satisfying all these criteria simultaneously remains challenging to obtain for most candidate sources, necessitating new approaches to CSO identification.

### 2.2. VLBI CSO sample

The COINS (CSOs Observed in the Northern Sky) sample contributed 52 CSOs and candidates from a VLBI continuum survey of approximately 2000 compact radio sources (Peck & Taylor 2000). An & Baan (2012) provided 46 CSOs and candidates with kinematic measurements for 24 sources, enabling statistical analysis of their dynamical properties. The VLBA Imaging and Polarimetry Survey (VIPS) at 5 GHz yielded 103 CSO candidates from observations of 1127 sources (Taylor et al. 2005; Helmboldt et al. 2007), from which Tremblay et al. (2016) identified 24 CSOs and 33 new candidates.

Our CSO candidate sample combines data from these three CSO studies, yielding over 140 candidates based on symmetric morphology and steep or convex radio spectra (Appendix A). After removing redundant sources (Fig. 1), we established a consolidated sample of 105 CSO candidates (Appendix B). While not comprehensive in sky coverage or flux density limits, this dataset comprises the most credible CSOs and candidates confirmed through multiple criteria (primarily morphology and radio spectra) in previous studies, providing an effective testbed for our CSO identification technique.

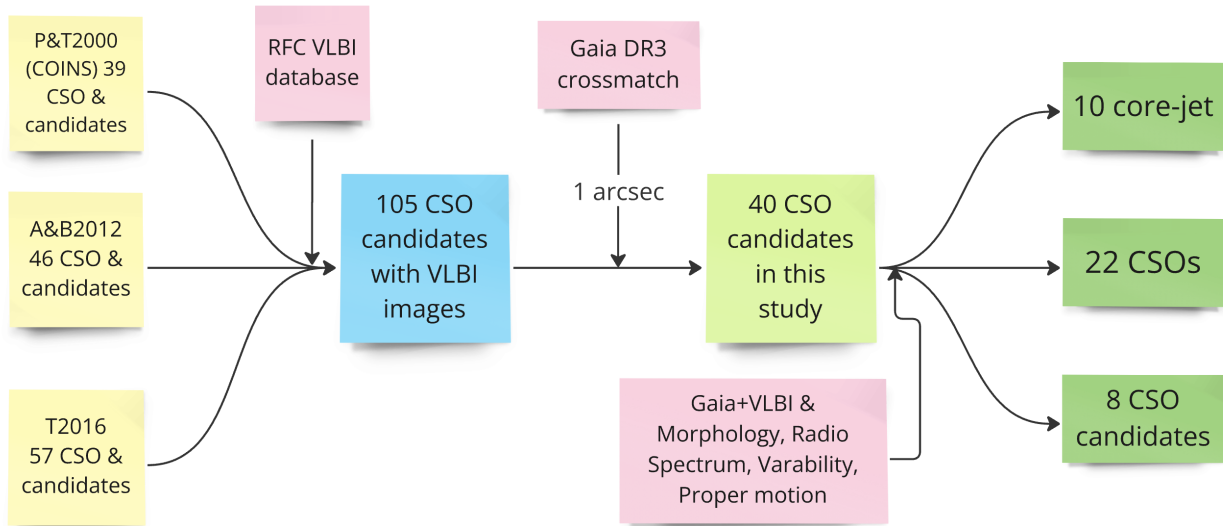


**Fig. 1.** The flowchart of our sample selection procedure. P&T2000: Peck & Taylor (2000); A&B2012: An & Baan (2012); T2016: Tremblay et al. (2016). RFC VLBI database: the Radio Fundamental Catalog (Astrogeo, <http://astrogeo.org/rfc/>, Petrov & Kovalev 2025). Gaia DR3: <https://www.cosmos.esa.int/web/gaia/data-release-3>.

### 2.3. Gaia+VLBI sample

We introduce a novel approach that combines high-precision optical astrometry from *Gaia* with high-resolution VLBI imaging to unambiguously identify CSO cores. While previous studies comparing *Gaia* and VLBI astrometry focused mainly on radio-optical offsets in core-jet sources (Petrov & Kovalev 2017), our work represents the first systematic applications of this methodology to a large CSO sample, directly addressing the persistent challenge of identifying CSO cores.

By cross-matching our VLBI sample with the *Gaia* DR3 catalogue using a 1'' search radius, we identified 40 optical counterparts (Table 1) from 105 CSO candidates (Appendix C). The *Gaia* optical centroid corresponds to the immediate vicinity of the accretion disk and central supermassive black hole (SMBH), providing a reliable reference point for the AGN core position. When combined with VLBI's sub-millarcsecond (mas) resolution, this allows precise localization of the central engine in these young radio sources, even when the radio core is faint or obscured. The modest match rate (38%) suggests that most CSO nuclei are optically faint or obscured.

The cross-matched sample includes a heterogeneous mix of quasars ( $\sim 40\%$ ), radio galaxies, and other AGN types (Table 1 and Fig. B.1). Most CSOs and candidates cluster at low and moderate redshifts ( $z < 1.0$ ), while core-jet sources show a broader redshift range. This methodological approach offers significant advantages over traditional techniques:

- precise core localization even when radio emission is weak or obscured
  - unambiguous discrimination between CSOs and core-jet sources
  - independent verification of radio structure orientation
  - enhanced accuracy in kinematic measurements by establishing a fixed reference point

The combination of *Gaia*'s unprecedented astrometric precision ( $\sim 0.04$  mas for bright sources,  $\sim 0.7$  mas at  $G = 20^{\text{mag}}$ ) with VLBI's sub-mas resolution creates a powerful tool for studying the birth and evolution of radio galaxies.

### 3. Results

Our application of the *Gaia*+VLBI method yielded definitive classifications for 32 of 40 CSO candidates, demonstrating the effectiveness of combining high-precision optical astrometry with radio imaging. We confirmed 22 sources as genuine CSOs (Fig. B.2), identified 10 as core-jet AGN (Fig. B.3), while 8 sources (Fig. B.4) remain ambiguous due to significant radio-optical positional discrepancies.

### 3.1. Confirmed CSOs

Among 22 confirmed CSOs, 17 show direct *Gaia*+VLBI positional alignment, with 5 supported by additional morphological and spectral evidence despite larger positional offsets (Fig B.2). These sources display diverse morphologies that provide crucial insights into their physical nature and evolutionary stages.

The majority exhibit classic double-lobed structures with symmetric hotspots, exemplified by J1111+1955 and J1326+3154. Several sources show complex morphologies that reveal rich jet-ISM interactions. For example, J0832+1832 and J1815+6127 feature multiple hotspots in their radio lobes and large misalignment, suggesting jet deflection or multiple impact sites at the jet-ISM interface. The dramatically bent jet in J1158+2450 presents compelling evidence of environmental influence, while the elongated, clumpy structure of J1244+4048 indicates jet instabilities driven by ISM entrainment.

Our multi-frequency approach proves crucial for reliable CSO identification. The 2.3-GHz observations of J0741+2706, J0832+1832, J1256+5652, and J2355+4950 reveal extended emission structures invisible at higher frequencies, providing critical evidence for their CSO classification. This frequency-dependent effect occurs because steep-spectrum components, particularly counter-lobes, become too faint to detect at 5 and 8.4 GHz due to the combined effects of spectral steepening and Doppler deboosting.

The spectral properties of our sample offer valuable insights into CSO physics. Most sources display the characteristic steep-spectrum lobes ( $\alpha > 0.5$ ) consistent with aging relativistic electron populations. Central regions generally show flatter spectra,

steepening toward the lobes, indicating continuous particle acceleration near the core. Of particular interest are the jet–ISM interaction regions, which often exhibit distinctly flat or even inverted spectra, as seen in the southern lobe of J0943+1702 and the northeastern jet of J1158+2450. These spectral features provide direct evidence of ongoing particle acceleration in interaction zones.

Kinematic analysis (Table 2) reveals diverse hotspot separation speeds in our CSO sample. Most sources display sub-relativistic motions ( $< 0.5 c$ ), characteristic of symmetric jet expansion in young radio galaxies (Peck & Taylor 2000; Kawakatu & Kino 2006; An & Baan 2012). However, two quasars (J0943+1702 and J1602+2418) show mildly relativistic hotspot advance speeds of  $(1.05 \pm 0.5)c$  and  $(1.27 \pm 0.22)c$ , respectively, though with substantial uncertainties. While J1111+1955, a galaxy-type CSO, appears to show an unusually high apparent speed, this measurement is based on limited data spanning only three epochs over three years and requires confirmation with longer-term monitoring. The measured proper motions yield kinematic age estimates spanning from  $\sim 40$  years (J1111+1955) to over 1600 years (J1234+4753), revealing diverse evolutionary stages. Three sources (J1110+4817, J1256+5652, J1815+6127) show apparent negative speeds, likely arising from complex changes in emission structure or projection effects (An et al. 2012).

Notably, five nearby ( $z \leq 0.1$ ) CSOs — J0048+3157 (NGC 262, Mrk 348), J1247+6723, J1407+2827, J1511+0518, and J1945+7055 — show systematic radio–optical offsets despite strong morphological and spectral evidence supporting their CSO nature. This includes well-studied sources like J1407+2827 (OQ 208, Stanghellini et al. 1997; An et al. 2012; Wu et al. 2013), where the *Gaia* position coincides with a radio lobe rather than the core, likely due to bright optical emission from jet–ISM interaction regions. These cases highlight how environmental effects in host galaxies can complicate optical position interpretation. In starburst or merging host galaxies, significant dust extinction and complex optical structures can lead to substantial *Gaia* positioning uncertainties. While illustrating limitations of the *Gaia*+VLBI method for nearby galaxies with weak or obscured optical nuclei, their CSO classification remains secure based on comprehensive morphological and spectral evidence.

Our confirmed CSO sample spans a broad range of redshifts (0.015 to 1.791, median 0.269) and projected linear sizes (3.6 to 290 pc), all below the conventional 1 kpc limit for CSOs (Table 1). This diversity facilitates investigation of different aspects of CSO evolution, from initial jet propagation to the development of large-scale radio structure.

### 3.2. Core–jet sources

We identified 10 sources as core–jet AGN based on distinctive characteristics that clearly differentiate them from CSOs (Fig. B.3). The key identifier is the alignment of *Gaia* optical positions with the brightest components at the ends of the elongated radio structures, a hallmark of relativistically beamed emission.

A key phenomenon observed in these sources is the core shift effect — the systematic change in apparent core position with observing frequency due to synchrotron self-absorption gradients along the jet (Lobanov & Zensus 1999). At higher frequencies, we observe regions closer to the SMBH, while optical emission originates even closer (Kovalev et al. 2008). In several core–jet sources (e.g., J0753+4231, J1311+1417), the optical peak associates with a weaker upstream component

rather than the brightest radio feature, indicating the true core location obscured by synchrotron self-absorption at radio frequencies. In J0003+2129, the *Gaia* position coincides with the counter-jet region, which remains invisible due to Doppler deboosting. In most sources, the optical–radio offsets are less than 1 mas, consistent with astrometric uncertainties. An exception is J2022+6136, where the flat-spectrum radio component is offset by more than 13 mas from the *Gaia* position, likely associated with an optically bright hotspot downstream of the jet.

Kinematic analysis (Fig. B.3 and Table B.5) provides crucial evidence for the relativistic nature of these jets. Proper motion measurements for six sources reveal apparent jet speeds ranging from  $0.68 c$  to  $5.43 c$ , significantly higher than the sub-relativistic speeds typical of CSOs.

### 3.3. CSO candidates

Eight sources (Fig. B.4) defy straightforward classification, as these objects exhibit significant discrepancies between their *Gaia* optical positions and VLBI radio structures, with positional offsets exceeding combined astrometric uncertainties. This suggests that *Gaia* detections may correspond to physically unrelated foreground/background objects or extended host galaxy features rather than the AGN cores (Bailer-Jones et al. 2019).

J0831+4608 and J1254+1856 have been observed only at a single epoch and frequency, limiting definitive classification. While their morphology suggests CSO characteristics, confirmation requires multi-epoch multi-frequency VLBI observations to reveal their spectral properties and proper motions.

J1559+5924 displays a triple structure with a central bright component and two extended features, resembling a mini FR I galaxy. It remains a CSO candidate, potentially belonging to a subclass of low-power CSOs with weak, two-sided jets. Further investigation of this source could provide insights into the diversity of CSO morphologies.

J0119+3210, J0906+4636, and J1148+5924 exhibit complex radio emission without the compact, edge-brightened lobes typical of CSOs. Their extended emission may result from nuclear star formation, supernova remnants, or diffuse jets. The significant offsets between their optical and radio emission centers suggest complex interactions between the AGN and host galaxy environment.

J0650+6001 challenges conventional classification schemes with its unusual combination of properties. While its *Gaia* position near the southernmost component suggests a core–jet source, it displays an overall gigahertz-peaked spectrum (GPS) and relatively slow jet motion ( $0.35 c$ , Lister et al. 2019). However, its notable variability contradicts typical CSO characteristics, making its true nature uncertain.

These ambiguous cases manifest the limitations of current classification schemes and highlight the importance of comprehensive multi-criteria analysis in understanding the full diversity of compact radio sources. Their study may reveal new subclasses or evolutionary stages bridging established categories, advancing our understanding of radio galaxy evolution.

## 4. Discussion

### 4.1. Efficacy and validation of the *Gaia*+VLBI method

The integration of *Gaia* optical astrometry with VLBI radio imaging provides a powerful new approach for identifying AGN cores in compact radio sources. Our successful confirmation of

22 CSOs demonstrates this method's effectiveness in addressing a fundamental challenge in CSO identification. The key strengths of this method include precise core localization even when radio emission is weak or obscured, unambiguous discrimination between CSOs and core-jet sources, independent verification of radio structure orientation, and enhanced accuracy in kinematic measurements.

Our method complements recent comprehensive studies such as the ‘bona fide’ CSO catalogue (Kiehlmann et al. 2024a). While their catalogue of 79 CSOs, including 43 edge-brightened CSOs (their ‘CSO 2’ class) with redshifts, relies on strict radio-based criteria, our method introduces precise optical–radio correlation as an additional diagnostic tool. The ~60% overlap (13 out of 22) between our confirmed CSOs and Kiehlmann’s catalogue validates our approach while highlighting potentials for new insights. Two sources we classify as core-jet (J1816+3457, J2022+6136) are listed as CSOs by Kiehlmann et al. (2024a), demonstrating the complexity of CSO identification.

However, several important limitations must be considered:

- Source confusion from foreground or background objects and extended emission from host galaxies can affect centroid positions.
- Optical emission from jets or hotspots may dominate over core emission in some cases (e.g. J1407+2827), potentially leading to misidentification.
- Reduced effectiveness for nearby galaxies where extended optical structure affects *Gaia* measurements (e.g. J1511+0518).
- Potential bias against heavily obscured AGN due to systematic offsets from dust obscuration.
- Inherent limitation to optically bright sources, restricting application to radio-quiet or very compact sources, particularly at high redshifts.

To mitigate these limitations, we recommend a multi-wavelength approach combining data across different bands, careful assessment of host galaxy properties, and integration with traditional radio-based classification methods. Despite these constraints, the *Gaia*+VLBI method represents a significant advance in CSO identification, particularly in their earliest stages where traditional methods often prove inadequate. Future work will expand this pilot study by cross-matching *Gaia* with over 20,000 Astrogeo VLBI sources. This extensive dataset will illuminate selection effects, environmental factors, and CSO evolutionary pathways across diverse populations.

## 4.2. Radiation characteristics of CSOs

### 4.2.1. Radio Morphology and Spectral Properties

Our high-resolution VLBI observations combined with *Gaia* astrometry reveal diverse morphological and spectral properties that provide key insights into CSO physics and evolution.

The majority (~ 70%) of confirmed CSOs exhibit classical double-lobed structure with edge-brightened hotspots (e.g., J1111+1955, J1358+4737, J1602+2418, and J1823+7938) supporting theoretical models where young jets propagate symmetrically through dense interstellar medium. The emission typically becomes detectable when the jet terminates in a shock, efficiently converting kinetic energy into relativistic particles (Blandford & Rees 1974; Begelman et al. 1984; Scheuer 1995; Meisenheimer et al. 1989). For high-power jets, the kinetic energy is rarely lost as radiation during jet propagation, which often makes the core and inner jet invisible.

Only six CSOs (J0741+2706, J1158+2450, J1234+4754, J1244+4048, J1256+5652, and J1310+3403) are detected with central radio components, which likely represent unresolved inner jet regions rather than cores. Several CSOs display complex morphologies indicating strong jet–ISM interactions. For example, J0832+1832 and J1815+6127 show multiple hotspots suggesting jet deflection or impact with dense ISM clouds (Men-doza & Longair 2002), or jet head impacting multiple sites of the interface (Carvalho & O’Dea 2002; An et al. 2012).

The dramatically bent jet in J1158+2450 provides direct evidence of how strong jet–ISM interactions can sculpt the CSO morphology (Mukherjee et al. 2016). Similarly, the elongated, clumpy jet structure in J1244+4048 likely results from jet instabilities induced by entrainment of the ISM (e.g. Bicknell 1984). In J1256+5652 (Mrk 231), we observe an east–west oriented jet within 2 mas of the core, but extended emission at 20–30 mas scales (Wang et al. 2021). This structure hints at multiple episodes of AGN activity, offering a rare glimpse into the duty cycle of these young radio sources and challenging simple, monotonic evolution models (Saikia & Jamrozy 2009; Brock-sopp et al. 2011; Orienti & Dallacasa 2020; Brocksopp et al. 2007). Such recurrent activity (Section 4.2.3), observed in numerous compact radio sources, reveals key aspects of both AGN feedback processes and long-term evolution of radio galaxies (Schoenmakers et al. 2000; Konar et al. 2012; Nandi et al. 2019).

The spectral properties provide additional information on the physical conditions in these sources. The overall radio spectra typically show a convex shape with a turnover near 5 GHz, attributed to synchrotron self-absorption in compact, high-density regions (O’Dea 1998). This characteristic is not limited to our low-redshift sample but also observed in high-redshift CSOs (Sotnikova et al. 2021).

The central regions generally exhibit flatter spectra, steepening towards the lobes (e.g., J1234+4753 and J1244+4048), consistent with theoretical models of continuous particle acceleration in central regions, followed by spectral aging as the plasma flows outward (Pacholczyk 1970). Regions of jet–ISM interaction often show flat or inverted spectra (e.g., the southern lobe of J0943+1702), indicating ongoing particle acceleration in these interaction zones (Godfrey et al. 2009).

The observed morphological and spectral diversity indicates that CSOs are not merely scaled-down versions of larger radio galaxies (An & Baan 2012), but represent crucial laboratories for studying jet–ISM interactions, shock physics, and AGN feedback in action (Tadhunter 2016).

### 4.2.2. Brightness temperatures and Doppler boosting

Our VLBI observations reveal a distinct contrast between CSOs and other radio-loud AGN classes in their relativistic beaming properties. CSO components typically exhibit moderate brightness temperatures ( $T_b \sim 10^7 - 10^{10}$  K), well below the inverse Compton limit of  $\sim 10^{12}$  K (Kellermann & Pauliny-Toth 1969; Readhead 1994). This, combined with derived Doppler-boosting factor  $< 1$ , distinguishes CSOs from highly beamed sources like blazars (Kovalev et al. 2005; Jorstad et al. 2005; Homan et al. 2006; Hovatta et al. 2009; Liodakis et al. 2018; Cheng et al. 2020). Unlike flat-spectrum radio quasars with core  $T_b > 10^{11}$  K and Doppler factors  $> 10$  (Pushkarev & Kovalev 2012), our CSO sample consistently fall below these thresholds (Readhead et al. 1996b; Polatidis & Conway 2003; An & Baan 2012), reinforcing their interpretation as young, intrinsically symmetric sources.

The combination of moderate brightness temperatures and minimal Doppler boosting in CSOs allow direct measurement

of intrinsic source properties without the complicating effects of relativistic beaming, making CSOs as critical probes of fundamental AGN jet physics and early evolution.

#### 4.2.3. Variability

Despite limited multi-epoch data, CSOs in our sample exhibit remarkably low variability, fundamentally distinguishing them from more variable radio sources like flat-spectrum radio quasars (FSRQs). While FSRQs commonly show variations exceeding factors of 2–20 due to relativistic beaming effects (e.g. III Zw 2, Wang et al. 2023a), CSOs remain notably steady (Fassnacht & Taylor 2001; Sotnikova et al. 2024). This stability reflects the dominance of lobe emission that was energized over large time scales, representing the adiabatic expansion and steady growth of radio galaxies (O’Dea 1998; Orienti 2016).

#### 4.2.4. Hotspot advance speeds and kinematical ages

Our kinematic analysis spans over two decades and reveals hotspot separation speeds ranging from  $0.06c$  to  $2.54c$ , with most sources exhibiting sub-relativistic speeds. This velocity distribution strongly supports models of young radio source evolution (Kawakatu & Kino 2006; Bicknell et al. 2018).

We exclude J1111+1955 from our kinematic analysis due to conflicting measurements. Our 2015–2018 VLBI data shows an unusually high apparent speed ( $\sim 5.5c$ ), strongly contrasting with previous sub-relativistic measurements ( $< 0.19c$ ) from 1997–2002 (Gugliucci et al. 2005). This discrepancy requires caution, especially as this source resides in a Seyfert II galaxy at  $z = 0.299$  (Urry & Padovani 1995), where large viewing angles typically produce lower apparent speeds. Our limited observation epochs prevent definitive conclusions about this anomaly. Long-term monitoring with consistent temporal sampling is needed to reliably determine its kinematics.

Two high-redshift ( $z > 1.5$ ) quasars (J0943+1702 and J1602+2418) display apparent hotspot separation speeds exceeding  $2c$ , though with considerable uncertainties in their measurements. These CSOs likely represent a subpopulation with mildly relativistic jets oriented at small angles to our line of sight, creating an intermediate class between traditional CSOs and more strongly beamed sources. Their detection at high redshifts may reflect an observational bias, as only the most powerful and possibly more beamed sources are likely to be detected in flux-density-limited samples.

Two sources, J1110+4817 and J1815+6127, show apparent contraction (negative speeds) with bent jet heads, suggesting projection effects where three-dimensional jet paths curve relative to our line of sight (An et al. 2012).

In CSOs with detected radio cores, we observe systematic asymmetries in hotspot advance speeds relative to the core. These asymmetries likely reflect environmental differences on opposite sides of the nucleus (Jeyakumar et al. 2005; Orienti & Dallacasa 2014), providing direct evidence for the role of host galaxy properties in shaping CSO evolution.

All these exceptional cases reflect the complexity of CSO kinematics and the necessity for long-term monitoring to accurately determine their evolutionary status (Scheuer 1995; Owsianik & Conway 1998).

The kinematic measurements reveal CSO ages spanning from 80 to over 1800 years (Table 2). Notably, the youngest sources in our sample are associated with those two high-redshift quasars discussed above, possibly reflecting an obser-

vational bias in flux-density-limited samples. The broad distribution of ages suggests that we are observing CSOs at various stages of early evolution (Polatidis & Conway 2003; Gugliucci et al. 2005; An & Baan 2012) and supports a scenario where the CSO population comprises two distinct classes: genuine young and growing radio galaxies that will eventually evolve into large-scale radio sources, and older systems where radio lobes are either dying out or frustrated by dense surrounding media.

### 4.3. Nature and Evolution of CSOs

#### 4.3.1. Evolutionary Tracks and Classification

The kinematic properties of our well-characterized sample provide strong evidence for distinct evolutionary paths in the CSO population. Our statistical analysis combines 24 CSOs from An & Baan (2012) with 10 additional sources from the current study, all having measured redshifts and hotspot separation speeds (Table 3). The relationships shown in Fig. 2 are derived for this subset of sources, offering insights into the connections between radio power, size, velocity, and age in young radio galaxies.

The power–size correlation (Fig. 2-a) demonstrates a clear dichotomy in the CSO population, supporting our previous proposition (An & Baan 2012) of two distinct evolutionary tracks. While the predicted radio power would vary with projected source size as  $P_{\text{rad}} \propto D^4$ , our analysis reveals a clear division at a threshold radio power of approximately  $10^{26.5} \text{ W Hz}^{-1}$  (e.g., Kunert-Bajraszewska et al. 2010). Above this threshold power, CSOs exhibit a relatively tight correlation, suggesting efficient conversion of jet power into source expansion. Below this threshold, sources show a more scattered distribution with limited size growth, indicating their evolution is significantly influenced by their host galaxy environment.

The dichotomy mirrors the established FR I/II division in extended radio galaxies (Fanaroff & Riley 1974; Hardcastle & Croston 2020) and reflects theoretical models where high-power jets penetrate the ambient medium while lower-power jets are more susceptible to environmental effects that can impede or redirect their expansion. Although our sample may favor powerful sources due to proper motion measurement requirements, the consistency of this division across multiple observational parameters suggests it represents a fundamental aspect of CSO evolution rather than selection bias.

Figure 2 panels *b–f* illustrate systematic differences between high-power (red symbols) and low-power (black symbols) CSOs. High-power sources display systematically larger sizes, higher hotspot advance speeds, and a broader distribution of kinematic ages. Radio powers in panels *a* and *d* follow the theoretical predictions  $P_{\text{rad}} \propto D^{2/3}$  and  $P_{\text{rad}} \propto T^{2/5}$  (where  $D$  is projected size and  $T$  is age), indicating increasing efficiency in converting jet kinetic energy to radio emission during the CSO phase as adiabatic losses in the lobes dominate energy dissipation. Additionally, An & Baan (2012) predict an inverse relationship between hotspot velocity and radiative power ( $V \propto P^{-1}$ ) for sources with constant power (dashed arrows).

High-power CSOs ( $P > 10^{26.5} \text{ W Hz}^{-1}$ ) typically achieve higher hotspot advance speeds  $> 0.2c$ , with velocities that tend to increase with source size (Fig. 2-b and 2-c). This behavior characterizes young radio galaxies possessing sufficient energy flux to effectively penetrate their host galaxy environment (Kawakatu & Kino 2006). In contrast, low-power CSOs show consistently slower speeds ( $< 0.1c$ ) regardless of size, suggesting their expansion is significantly influenced by interaction with the ISM (O’Dea & Saikia 2021).

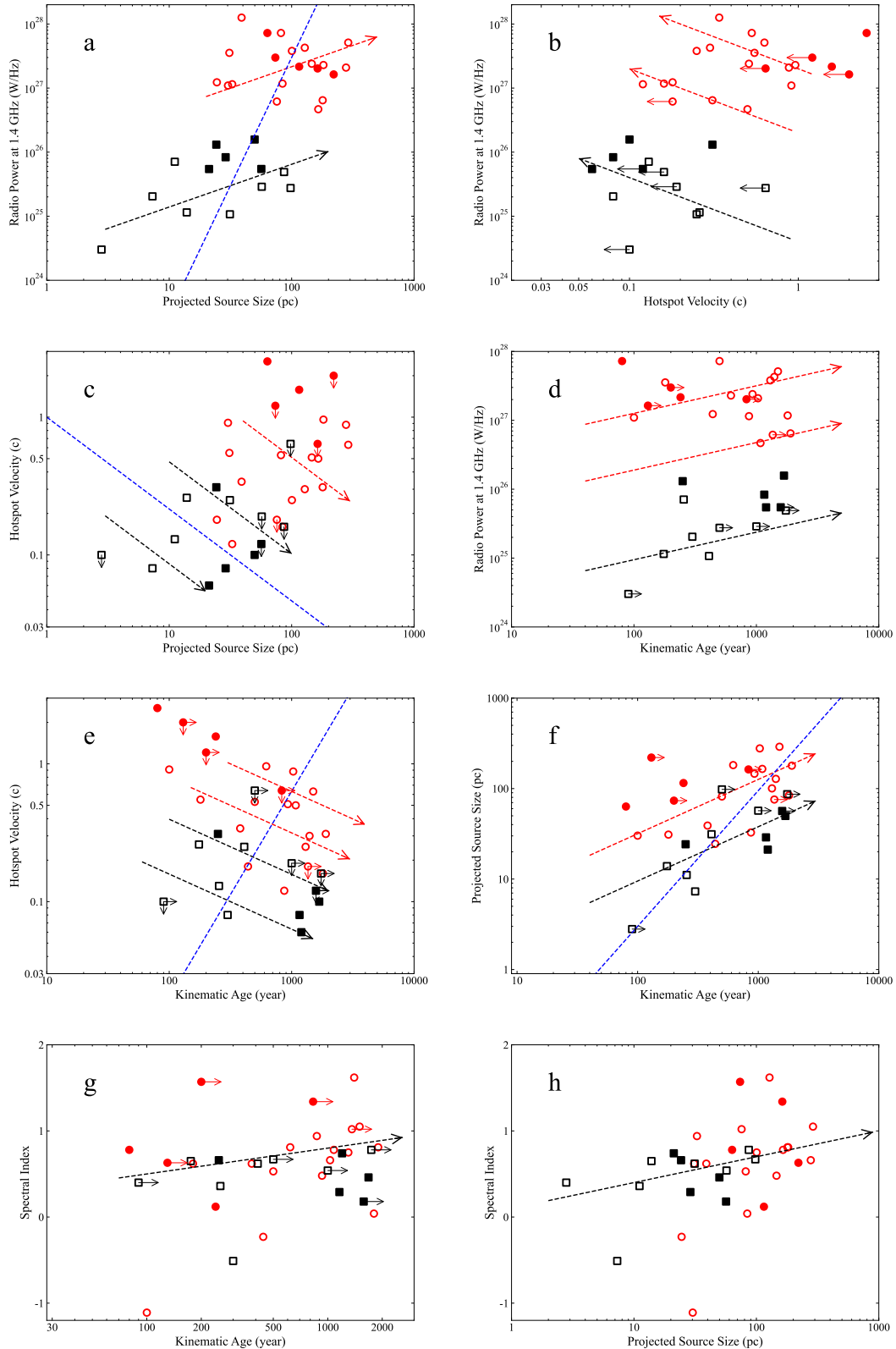


**Fig. 2.** The parameter distributions of the sample of 34 CSO sources combined with model predictions. Black symbols denote low-power CSOs ( $P < 10^{26.5}$  W Hz $^{-1}$ ) and red symbols represent high-power CSOs. The filled symbols are from the current study and the open symbols are from An & Baan (2012). Red and black dashed arrows relate to evolutionary trend for high- and low-power source distributions. The blue dashed lines in panels a, c, and f show the general power trend trend of the groups as a whole. The blue dashed line in panel b shows the expected survival threshold for low power sources. Panel a: The red and black dashed arrows denote the predicted  $P_{\text{rad}} \propto D^{2/3}$  adiabatic-loss-dominated evolution of a source with constant power, and the blue dashed line indicates the predicted Power-Size distribution  $P_{\text{rad}} \propto D^4$ . Panel b: Red and black dashed arrows show the predicted inverse relationship between radio power and hotspot velocity  $P \propto V^{-1}$ . Panel c: The hotspot velocity varies with the projected source size as  $V_{\text{rad}} \propto D^{-2/3}$ . Panel d: Dashed arrows show the predicted evolutionary relation of  $P_{\text{rad}} \propto T^{3/5}$ . Panels e and f: Dashed arrows indicate the predicted evolution following  $V_{\text{HS}} \propto T^{-2/5}$  and  $D \propto T^{3/5}$ . Panels g and h: The relatively flat distribution of the spectral index shows a slight steepening towards  $\alpha = 1$  with increasing Kinematic Age  $T$  and with projected Source Size  $D$ .

The variation of spectral index with both kinematic age and projected source size (Fig. 2 panels *g* and *h*) reveals a systematic pattern. The youngest and smallest CSOs typically exhibit relatively flat spectra ( $\alpha \approx 0.3 - 0.5$ ), indicating strong synchrotron self-absorption in compact regions. As sources age and expand, their spectra systematically steepen, with spectral indices approaching  $\alpha \approx 1.0$  for the oldest and largest CSOs, reflecting the decreasing importance of synchrotron self-absorption as source components expand and energy density decreases.

#### 4.3.2. Evolutionary Pathways and Feedback Mechanisms

The CSO population exhibits distinct evolutionary pathways corresponding to their power classification. High-power CSOs can maintain sustained growth with jets that effectively penetrate dense ambient media, allowing them to evolve through the complete CSO–MSO–LSO sequence (here MSO and LSO stand for medium-sized and large-sized symmetric objects, respectively). Their broader age distribution indicates longer survival while maintaining double-lobe characteristics. These sources provide mechanical feedback by clearing out nuclear environments and potentially influencing galactic evolution on larger scales (Tadhunter 2016; O’Dea & Saikia 2021).

In contrast, low-power CSOs typically have smaller sizes and slower expansion speeds, likely constrained by environments (Baan & An 2025), potentially preventing expansion beyond the ISM. Their narrower size distribution coupled with broader age distribution suggests periods of stalled or intermittent growth, extending their time in the CSO phase. These sources contribute primarily to localized thermal feedback and ISM regulation. Recent studies of low-power radio galaxies (Baldi 2023; Chilufya et al. 2024) further suggest that AGN feedback operates through multiple channels depending on jet power, with important implications for galaxy evolution models.

The substantial population of identified lower-power CSOs supports a *frustrated* or *confined* evolutionary scenario, where weaker jets interact repeatedly with the dense and clumpy ISM. These sources, while contributing significantly to energy injection in the nuclear regions, may never develop the extended structures characteristic of classical radio galaxies. This distinction between *successful* and *frustrated* jets is consistent with recent observations showing many faint radio sources remaining embedded within galactic tori or circum-nuclear star-forming regions. Such sources may primarily influence their immediate nuclear environment rather than affect the broader galactic halo or intergalactic medium, representing a more localized mode of AGN feedback (Hardcastle & Croston 2020).

Low-power CSOs present a complex evolutionary picture. Their weaker jets often interact with the interstellar medium, leading to external material entrainment and mechanical energy losses (Norman et al. 1982; Kawakatu et al. 2008; Wang et al. 2009). Initially showing CSO morphology, they may rapidly lose defined lobes as jets fragment. These sources potentially connect to radio-weak AGN (Sadler et al. 2002; Croston et al. 2019; Drake et al. 2024), supporting the “frustrated” jet model. They are primarily observable in nearby galaxies such as J0048+3157 (NGC 262) and J2355+4950, and recent observations of radio-quiet quasars reveal weak radio sources with low-power CSO-like morphologies (e.g. Alhosani et al. 2022; Chen et al. 2023a; Wang et al. 2023b).

These failed sources continue to evolve slowly, exerting significant feedback on their host galaxies (Bicknell et al. 2003; Shabala & Alexander 2009; Mukherjee et al. 2016; Morganti & Oosterloo 2018; Santoro et al. 2020; Tadhunter et al. 2021;

Kukreti et al. 2023). Some high-power CSOs may deviate from their evolutionary path due to changes in AGN activity or environmental interactions, becoming dying CSOs or MSOs (Kunert-Bajraszewska et al. 2010; An & Baan 2012). These failed CSOs may share observational features with CSO class 2.2, as described by Readhead et al. (2024).

#### 4.4. Classification and Origin Mechanisms

Recently, Kiehlmann et al. (2024a) proposed a CSO classification scheme similar to our power-based dichotomy, describing an edge-dimmed, low-luminosity class (CSO 1), and an edge-brightened, high-luminosity class (CSO 2). Regarding low-power CSOs (or weak-jet CSOs), we align with the CSO 1 classification of Readhead et al. (2024). These likely constitute the majority of radio galaxies, including numerous young sources only recently identified through low-frequency surveys (e.g., Hardcastle & Croston 2020; O’Dea & Saikia 2021).

Readhead et al. (2024) further propose that the transient nature of most high-power CSOs could be explained by ignition in Tidal Disruption Events (TDEs) of giant stars (Rees 1988). Our analysis suggests that intermittent TDEs are unlikely to be the primary mechanism for most high-power CSOs, supported by several critical factors: (1) The host galaxy demographics differ significantly. TDEs predominantly occur in spiral-type galaxies with pseudobulges (Law-Smith et al. 2017; French et al. 2020), whereas CSOs are typically hosted by luminous elliptical or ultraluminous infrared galaxies with classical bulges and higher central black hole masses (Willett et al. 2010; Tadhunter et al. 2011; Kosmaczewski et al. 2020; Liao & Gu 2020). The preference for post-merger systems among CSO hosts further distinguishes them from typical TDE hosts. (2) The continuous radiation structures in many CSOs directly contradict expectations for transient events. VLBI observations reveal smoothly connected emission from inner jets to terminal hotspots, with inner jets often displaying higher velocities than the hotspots (Taylor et al. 2000; An et al. 2012). This pattern indicates a continuous supply of energy from the central engine rather than the rapidly decaying energy injection expected from TDEs. (3) The timescale discrepancy is substantial. CSO lifetimes span 20–2000 years based on hotspot kinematic measurements (the present paper), drastically exceeding the typical TDE accretion timescales of months to years (Rees 1988; Gezari 2021). Even considering longer-lived TDE disks recently proposed, their maximum duration of  $\sim 10$  years remains orders of magnitude shorter than observed CSO lifetimes (Metzger & Stone 2016). (4) Energy requirements present a fundamental challenge to the TDE scenario. CSOs require sustained jet powers of  $10^{43} - 10^{47}$  erg s $^{-1}$  over centuries to millennia, corresponding to total energy budgets up to  $7 M_{\odot}c^2$  (Readhead et al. 2024). This vastly exceeds the available energy from typical TDEs ( $\sim 0.1 M_{\odot}c^2$ ), even considering complete disruption of massive stars (Stone & Metzger 2016). The required disruption of multiple massive stars in rapid succession lacks observational support and seems physically implausible. (5) Birth rate statistics strongly contradict TDE-driven formation. The CSO birth rate, estimated at  $3 \times 10^{-5}$  Gpc $^{-3}$  yr $^{-1}$  (Readhead et al. 1996b, 2024), falls at least two orders of magnitude below the observed TDE rate of  $10^{-5}$  Mpc $^{-3}$  yr $^{-1}$  (van Velzen 2018; Sazonov et al. 2021). Even considering that only 10% of TDEs might produce relativistic jets (Alexander et al. 2020), the discrepancy remains substantial and difficult to reconcile with the TDE scenario.

However, our interpretation of high-power CSO evolution differs from their view. While Kiehlmann et al. (2024b) suggest

that most high-power CSOs (their CSO 2 class) do not evolve into larger jetted AGN throughout their life cycles, characterized by sizes of  $D \leq 500$  pc and ages of  $T \leq 5000$  years, our data suggest these CSOs represent early-stage FR II radio galaxies, with some potentially evolving to kpc–Mpc scales. Some CSOs older than 1000 years and larger than 500 pc show continued growth with edge-brightened lobes, despite moderate hotspot advance speeds (Polatidis & Conway 2003; An & Baan 2012).

Moreover, many CSOs exhibit other AGN characteristics that align with long-lived activity rather than transient phenomena. These include prominent emission lines in optical spectra (Gelderman & Whittle 1994), significant infrared excess indicating dust heating by persistent AGN activity (Tadhunter et al. 2011), and X-ray properties consistent with obscured AGN rather than TDE remnants (Guainazzi et al. 2006; Siemiginowska et al. 2016; Sobolewska et al. 2019). The detection of extended radio emission beyond the CSO scale in some sources (e.g., 0108+388, 1511+0518) provides compelling evidence for recurrent AGN activity spanning much longer timescales than individual TDE events (Baum et al. 1990; Orienti & Dallacasa 2008; Kunert-Bajraszewska et al. 2010).

A more plausible explanation for CSO energetics involves standard AGN accretion processes driven by gas inflow during galaxy mergers or bar-induced instabilities (Hopkins & Quataert 2010; Storchi-Bergmann & Schnorr-Müller 2019). This aligns with the frequent observation of CSOs in merging or interacting systems and explains their significant fraction among infrared-luminous galaxies.

While we cannot rule out that some individual CSOs might be powered by exceptional TDEs, such as the disruption of extremely massive stars by intermediate-mass black holes or unusual multiple-star disruption events, the overall CSO population characteristics strongly favor conventional AGN mechanisms. The CSOs detected by *Gaia* in our sample may be subject to certain selection biases, particularly favoring optically brighter and lower-redshift sources. However, the radio properties and evolutionary characteristics we observe appear consistent across both *Gaia*-detected and non-detected populations, suggesting our conclusions about CSO physics remain robust.

The upcoming Square Kilometre Array (SKA) and its precursors will be crucial in detecting weaker CSOs and better understanding sources with low and intermediate powers ( $\leq 10^{25}$  W Hz $^{-1}$ ), which may represent a critical transition point between evolutionary pathways. Recent discoveries by SKA pathfinders have enhanced our understanding of CSO evolution through comprehensive flux-density-limited samples of FR I and FR II galaxies (e.g., Hardcastle et al. 2019; Mingo et al. 2019; White et al. 2020; Sejake et al. 2023).

Given their complex evolutionary properties, studying the entire CSO population, rather than focusing only on the brightest or peculiar subsets, is essential for fully understanding extragalactic radio galaxy evolution. Such comprehensive study will likely reveal more complex and diverse evolutionary paths than previously recognized, providing critical insights into both radio galaxy evolution and AGN feedback processes.

## 5. Summary

In this study, we have developed and validated a new method combining *Gaia* optical astrometry with multi-frequency VLBI observations to identify and characterize CSOs. Our main findings are:

1. Our innovative *Gaia*+VLBI approach has decisively classified 32 of 40 CSO candidates, confirming 22 genuine CSOs (17 through direct positional alignment of *Gaia* with symmetric radio structures, 5 through compelling morphological and spectral evidence despite larger positional offsets), and identifying 10 as core-jet sources. Eight sources remain ambiguous due to significant radio-optical discrepancies. This methodology effectively overcomes the long-standing challenge of detecting faint or absorbed radio cores in young radio galaxies.
2. We provide robust observational evidence for a two-track evolutionary paradigm in the CSO population. High-power CSOs ( $P_{\text{rad}} > 10^{26.5}$  W Hz $^{-1}$ ) demonstrate the potential to evolve into large-scale radio galaxies, exhibiting moderate relativistic hotspot advance speeds (typically 0.2 – 0.5 c) and systematic spectral gradients. In contrast, lower-power CSOs show characteristics consistent with the *Frustrated Radio Galaxy* concept, remaining confined within sub-kiloparsec scales with slower expansion speeds (< 0.1 c) and showing significant environmental impact on their morphology and spectral properties.
3. The quantitative relationships between radio power, kinematic age, hotspot velocity, and projected source size align remarkably well with theoretical predictions, revealing distinct evolutionary trajectories for high- and low-power CSOs. This confirms our earlier proposed evolutionary model where initial radio power significantly determines a source's developmental pathway and ultimate fate.
4. Our comprehensive analysis of CSO properties strongly challenges isolated TDE-driven formation as the primary origin mechanism for most CSOs. The observed extended timescales (up to  $\sim 2000$  years), persistent symmetrical jet structures, and substantial energy requirements are inconsistent with typical TDE characteristics but align with standard AGN accretion processes driven by gas infall during galaxy mergers or bar-induced instabilities.
5. Beyond radio power, we demonstrate that CSO evolution is governed by a complex interplay of environmental factors. The ambient medium density distribution, magnetohydrodynamic conditions in surrounding gas, intermittent accretion episodes, and central engine activity duration collectively shape CSO morphology, spectral signatures, and evolutionary trajectories, explaining the diverse observed characteristics within our sample.
6. CSOs serve as crucial laboratories for studying AGN feedback mechanisms across different power scales. High-power sources generate significant mechanical feedback on relatively large physical scales, while lower-power sources contribute predominantly to localized heating and ISM disruption in galactic cores, often without developing large-scale radio structures. This diversity reveals multiple channels of AGN feedback relevant to galaxy evolution models.
7. Future applications of our *Gaia*+VLBI methodology to larger samples will significantly advance our understanding of radio galaxy evolution. Particularly valuable would be high-sensitivity observations targeting low-power CSOs with next-generation facilities like SKA, which could reveal previously undetected populations and provide deeper insights into AGN feedback, the prevalence of frustrated sources, and complex interplay between radio sources and their host environments throughout cosmic history.

## 6. Data availability

The VLBI datasets underlying this article were derived from the public domain in the Astrogeo archive (<http://astrogeo.org/>).

**Acknowledgements.** This work is supported by the National Key R&D Programme of China (2022SKA0120102). TA and WAB acknowledge the support from the Xinjiang Tianchi Talent Program. YKZ is supported by the China Scholarship Council (No. 202104910165), the Shanghai Sailing Program under grant number 22YF1456100, and the Strategic Priority Research Program of the Chinese Academy of Sciences (Grant No. XDA0350205). YKZ thanks for the warm hospitality and the helpful comments from Ivy Wong in CSIRO Space&Astronomy in Australia. YKZ thanks for the valuable suggestions and comments from Krisztina Éva Gabányi in Konkoly Observatory, Hungary. SF thanks the Hungarian National Research, Development and Innovation Office (NKFIH, grant no. OTKA K134213) for support. This work was also supported by the NKFIH excellence grant TKP2021-NKTA-64. The authors acknowledge the use of Astrogeo Center database maintained by L. Petrov. This work has made use of data from the European Space Agency (ESA) mission *Gaia* (<https://www.cosmos.esa.int/gaia>), processed by the *Gaia* Data Processing and Analysis Consortium (DPAC, <https://www.cosmos.esa.int/web/gaia/dpac/consortium>). This work has made use of the NASA Astrophysics Data System Abstract Service, and the NASA/IPAC Extragalactic Database (NED), which is operated by the Jet Propulsion Laboratory, California Institute of Technology, under contract with the National Aeronautics and Space Administration. The National Radio Astronomy Observatory are facilities of the National Science Foundation operated under cooperative agreement by Associated Universities, Inc. This work has made use of data from the European Space Agency (ESA) mission *Gaia* (<https://www.cosmos.esa.int/gaia>), processed by the *Gaia* Data Processing and Analysis Consortium (DPAC, <https://www.cosmos.esa.int/web/gaia/dpac/consortium>). Funding for the DPAC has been provided by national institutions, in particular the institutions participating in the *Gaia* Multilateral Agreement.

- Fabricius, C., Luri, X., Arenou, F., et al. 2021, A&A, 649, A5  
 Fanaroff, B. L. & Riley, J. M. 1974, MNRAS, 167, 31P  
 Fanti, C. 2009, Astronomische Nachrichten, 330, 120  
 Fanti, C., Fanti, R., Dallacasa, D., et al. 1995, A&A, 302, 317  
 Fassnacht, C. D. & Taylor, G. B. 2001, AJ, 122, 1661  
 Fomalont, E. B. 1999, in Astronomical Society of the Pacific Conference Series, Vol. 180, Synthesis Imaging in Radio Astronomy II, ed. G. B. Taylor, C. L. Carilli, & R. A. Perley, 301  
 Fomalont, E. B., Petrov, L., MacMillan, D. S., Gordon, D., & Ma, C. 2003, AJ, 126, 2562  
 French, K. D., Wevers, T., Law-Smith, J., Graur, O., & Zabludoff, A. I. 2020, Space Sci. Rev., 216, 32  
 Gaia Collaboration, Prusti, T., de Bruijne, J. H. J., et al. 2016, A&A, 595, A1  
 Gaia Collaboration, Vallenari, A., Brown, A. G. A., et al. 2023, A&A, 674, A1  
 Gelderman, R. & Whittle, M. 1994, ApJS, 91, 491  
 Gezari, S. 2021, ARA&A, 59, 21  
 Godfrey, L. E. H., Bicknell, G. V., Lovell, J. E. J., et al. 2009, ApJ, 695, 707  
 Guainazzi, M., Siemiginowska, A., Stanghellini, C., et al. 2006, A&A, 446, 87  
 Gugliucci, N. E., Taylor, G. B., Peck, A. B., & Giroletti, M. 2005, ApJ, 622, 136  
 Hardcastle, M. J. & Croston, J. H. 2020, New A Rev., 88, 101539  
 Hardcastle, M. J., Williams, W. L., Best, P. N., et al. 2019, A&A, 622, A12  
 Healey, S. E., Romani, R. W., Taylor, G. B., et al. 2007, ApJS, 171, 61  
 Helmboldt, J. F., Taylor, G. B., Tremblay, S., et al. 2007, ApJ, 658, 203  
 Homan, D. C., Kovalev, Y. Y., Lister, M. L., et al. 2006, ApJ, 642, L115  
 Hopkins, P. F. & Quataert, E. 2010, MNRAS, 407, 1529  
 Hovatta, T., Valtaoja, E., Tornikoski, M., & Lähteenmäki, A. 2009, A&A, 494, 527  
 Hwang, H.-C., Shen, Y., Zakamska, N., & Liu, X. 2020, ApJ, 888, 73  
 Janiuk, A., Czerny, B., & Siemiginowska, A. 2002, ApJ, 576, 908  
 Jeyakumar, S., Wiita, P. J., Saikia, D. J., & Hooda, J. S. 2005, A&A, 432, 823  
 Jorstad, S. G., Marscher, A. P., Lister, M. L., et al. 2005, AJ, 130, 1418  
 Joshi, S. A., Nandi, S., Saikia, D. J., Ishwara-Chandra, C. H., & Konar, C. 2011, MNRAS, 414, 1397  
 Kaiser, C. R., Schoenmakers, A. P., & Röttgering, H. J. A. 2000, MNRAS, 315, 381  
 Kawakatu, N. & Kino, M. 2006, MNRAS, 370, 1513  
 Kawakatu, N., Nagai, H., & Kino, M. 2008, ApJ, 687, 141  
 Kellermann, K. I. & Owen, F. N. 1988, in Kellermann, K. I. and Verschuur, G. L., eds, Galactic and Extragalactic Radio Astronomy, 2nd edition, ed. K. I. Kellermann & G. L. Verschuur, Springer-Verlag (Springer-Verlag, Berlin-New York), 563–602  
 Kellermann, K. I. & Pauliny-Toth, I. I. K. 1969, ApJ, 155, L71  
 Kellermann, K. I., Sramek, R. A., Schmidt, M., Green, R. F., & Shaffer, D. B. 1994, AJ, 108, 1163  
 Kiehlmann, S., Lister, M. L., Readhead, A. C. S., et al. 2024a, ApJ, 961, 240  
 Kiehlmann, S., Readhead, A. C. S., O'Neill, S., et al. 2024b, ApJ, 961, 241  
 Konar, C. & Hardcastle, M. J. 2013, MNRAS, 436, 1595  
 Konar, C., Hardcastle, M. J., Jamrozy, M., Croston, J. H., & Nandi, S. 2012, MNRAS, 424, 1061  
 Kosmaczewski, E., Stawarz, Ł., Siemiginowska, A., et al. 2020, ApJ, 897, 164  
 Kovalev, Y. Y., Kellermann, K. I., Lister, M. L., et al. 2005, AJ, 130, 2473  
 Kovalev, Y. Y., Lobanov, A. P., Pushkarev, A. B., & Zensus, J. A. 2008, A&A, 483, 759  
 Kovalev, Y. Y., Petrov, L., Fomalont, E. B., & Gordon, D. 2007, AJ, 133, 1236  
 Kukreti, P., Morganti, R., Tadhunter, C., & Santoro, F. 2023, A&A, 674, A198  
 Kunert-Bajraszewska, M., Gawroński, M. P., Labiano, A., & Siemiginowska, A. 2010, MNRAS, 408, 2261  
 Law-Smith, J., Ramirez-Ruiz, E., Ellison, S. L., & Foley, R. J. 2017, ApJ, 850, 22  
 Liao, M. & Gu, M. 2020, MNRAS, 491, 92  
 Lindegren, L., Hernández, J., Bombrun, A., et al. 2018, A&A, 616, A2  
 Lindegren, L., Lammers, U., Hobbs, D., et al. 2012, A&A, 538, A78  
 Liodakis, I., Hovatta, T., Huppenkothen, D., et al. 2018, ApJ, 866, 137  
 Lister, M. L., Homan, D. C., Hovatta, T., et al. 2019, ApJ, 874, 43  
 Lobanov, A. P. 1998, A&A, 330, 79  
 Lobanov, A. P. & Zensus, J. A. 1999, ApJ, 521, 509  
 Machalski, J., Jamrozy, M., & Konar, C. 2010, A&A, 510, A84  
 Mahatma, V. H., Hardcastle, M. J., Williams, W. L., et al. 2019, A&A, 622, A13  
 Marecki, A. & Szablewski, M. 2009, A&A, 506, L33  
 Marr, J. M., Taylor, G. B., & Crawford, F. I. 2001, ApJ, 550, 160  
 Meisenheimer, K., Roser, H. J., Hiltner, P. R., et al. 1989, A&A, 219, 63  
 Mendoza, S. & Longair, M. S. 2002, MNRAS, 331, 323  
 Metzger, B. D. & Stone, N. C. 2016, MNRAS, 461, 948  
 Mingo, B., Croston, J. H., Hardcastle, M. J., et al. 2019, MNRAS, 488, 2701  
 Morganti, R. & Oosterloo, T. 2018, A&A Rev., 26, 4  
 Mukherjee, D., Bicknell, G. V., Sutherland, R., & Wagner, A. 2016, MNRAS, 461, 967  
 Nandi, S., Saikia, D. J., Roy, R., et al. 2019, MNRAS, 486, 5158  
 Norman, M. L., Winkler, K. H. A., Smarr, L., & Smith, M. D. 1982, A&A, 113, 285

- O'Dea, C. P. 1998, PASP, 110, 493  
 O'Dea, C. P., Baum, S. A., & Stanghellini, C. 1991, ApJ, 380, 66  
 O'Dea, C. P. & Saikia, D. J. 2021, A&A Rev., 29, 3  
 Orienti, M. 2016, Astronomische Nachrichten, 337, 9  
 Orienti, M. & Dallacasa, D. 2008, A&A, 487, 885  
 Orienti, M. & Dallacasa, D. 2014, MNRAS, 438, 463  
 Orienti, M. & Dallacasa, D. 2020, MNRAS, 499, 1340  
 Orienti, M., Dallacasa, D., Tinti, S., & Stanghellini, C. 2006, A&A, 450, 959  
 Orienti, M., Murgia, M., Dallacasa, D., Migliori, G., & D'Ammando, F. 2023, MNRAS, 522, 3877  
 Owsianik, I. & Conway, J. E. 1998, A&A, 337, 69  
 Pacholczyk, A. G. 1970, Radio astrophysics. Nonthermal processes in galactic and extragalactic sources  
 Pearson, T. J. & Readhead, A. C. S. 1981, ApJ, 248, 61  
 Pearson, T. J. & Readhead, A. C. S. 1988, ApJ, 328, 114  
 Peck, A. B. & Taylor, G. B. 2000, ApJ, 534, 90  
 Peck, A. B., Taylor, G. B., & Conway, J. E. 1999, ApJ, 521, 103  
 Petrov, L. 2016, arXiv e-prints, arXiv:1610.04951  
 Petrov, L. & Kovalev, Y. Y. 2017, MNRAS, 467, L71  
 Petrov, L., Kovalev, Y. Y., Fomalont, E., & Gordon, D. 2005, AJ, 129, 1163  
 Petrov, L., Kovalev, Y. Y., Fomalont, E. B., & Gordon, D. 2006, AJ, 131, 1872  
 Petrov, L., Kovalev, Y. Y., Fomalont, E. B., & Gordon, D. 2008, AJ, 136, 580  
 Petrov, L., Kovalev, Y. Y., & Plavin, A. V. 2019, MNRAS, 482, 3023  
 Petrov, L. Y. & Kovalev, Y. Y. 2025, ApJS, 276, 38  
 Phillips, R. B. & Mutel, R. L. 1980, ApJ, 236, 89  
 Phillips, R. B. & Mutel, R. L. 1982, A&A, 106, 21  
 Polatidis, A. G. & Conway, J. E. 2003, PASA, 20, 69  
 Porcas, R. W. 2009, A&A, 505, L1  
 Pushkarev, A. B. & Kovalev, Y. Y. 2012, A&A, 544, A34  
 Readhead, A. C. S. 1994, ApJ, 426, 51  
 Readhead, A. C. S., Ravi, V., Blandford, R. D., et al. 2024, ApJ, 961, 242  
 Readhead, A. C. S., Taylor, G. B., Pearson, T. J., & Wilkinson, P. N. 1996a, ApJ, 460, 634  
 Readhead, A. C. S., Taylor, G. B., Xu, W., et al. 1996b, ApJ, 460, 612  
 Rees, M. J. 1988, Nature, 333, 523  
 Sadler, E. M., Jackson, C. A., Cannon, R. D., et al. 2002, MNRAS, 329, 227  
 Saikia, D. J. & Jamrozy, M. 2009, Bulletin of the Astronomical Society of India, 37, 63  
 Santoro, F., Tadhunter, C., Baron, D., Morganti, R., & Holt, J. 2020, A&A, 644, A54  
 Scheuer, P. A. G. 1995, MNRAS, 277, 331  
 Schoenmakers, A. P., de Bruyn, A. G., Röttgering, H. J. A., & van der Laan, H. 2000, MNRAS, 315, 395  
 Schwartzman, E., Clarke, T. E., Nyland, K., et al. 2024, ApJ, 961, 233  
 Sejake, P. K., White, S. V., Heywood, I., et al. 2023, MNRAS, 518, 4290  
 Shabala, S. & Alexander, P. 2009, ApJ, 699, 525  
 Shen, Y., Chen, Y.-C., Hwang, H.-C., et al. 2021, Nature Astronomy, 5, 569  
 Shepherd, M. C. 1997, Astronomical Society of the Pacific Conference Series, Vol. 125, Difmap: an Interactive Program for Synthesis Imaging, ed. G. Hunt & H. Payne, 77  
 Siemiginowska, A., Czerny, B., Janiuk, A., et al. 2010, in Astronomical Society of the Pacific Conference Series, Vol. 427, Accretion and Ejection in AGN: a Global View, ed. L. Maraschi, G. Ghisellini, R. Della Ceca, & F. Tavecchio, 326  
 Siemiginowska, A., Sobolewska, M., Migliori, G., et al. 2016, ApJ, 823, 57  
 Snellen, I. A. G., Schilizzi, R. T., Miley, G. K., et al. 2000, MNRAS, 319, 445  
 Sobolewska, M., Siemiginowska, A., Guainazzi, M., et al. 2019, ApJ, 871, 71  
 Sotnikova, Y., Mikhailov, A., Mufakharov, T., et al. 2024, Galaxies, 12, 25  
 Sotnikova, Y., Mikhailov, A., Mufakharov, T., et al. 2021, MNRAS, 508, 2798  
 Sovers, O. J., Fanselow, J. L., & Jacobs, C. S. 1998, Reviews of Modern Physics, 70, 1393  
 Stanghellini, C., Bondi, M., Dallacasa, D., et al. 1997, A&A, 318, 376  
 Stone, N. C. & Metzger, B. D. 2016, MNRAS, 455, 859  
 Storchi-Bergmann, T. & Schnorr-Müller, A. 2019, Nature Astronomy, 3, 48  
 Tadhunter, C. 2016, A&A Rev., 24, 10  
 Tadhunter, C., Holt, J., González Delgado, R., et al. 2011, MNRAS, 412, 960  
 Tadhunter, C., Morganti, R., Santoro, F., & Bernhard, E. 2021, Astronomische Nachrichten, 342, 1200  
 Taylor, G. B., Fassnacht, C. D., Sjouwerman, L. O., et al. 2005, ApJS, 159, 27  
 Taylor, G. B., Marr, J. M., Pearson, T. J., & Readhead, A. C. S. 2000, ApJ, 541, 112  
 Taylor, G. B., Readhead, A. C. S., & Pearson, T. J. 1996, ApJ, 463, 95  
 Tremblay, S. E., Taylor, G. B., Ortiz, A. A., et al. 2016, MNRAS, 459, 820  
 Urry, C. M. & Padovani, P. 1995, PASP, 107, 803  
 van Breugel, W., Miley, G., & Heckman, T. 1984, AJ, 89, 5  
 Wang, A., An, T., Guo, S., et al. 2023a, ApJ, 944, 187  
 Wang, A., An, T., Jaiswal, S., et al. 2021, MNRAS, 504, 3823  
 Wang, A., An, T., Zhang, Y., et al. 2023b, MNRAS, 525, 6064  
 Wang, H.-C., Wang, J.-X., Gu, M.-F., & Liao, M. 2023c, MNRAS, 524, L38  
 Wang, Y., Kaiser, C. R., Laing, R., et al. 2009, MNRAS, 397, 1113  
 White, S. V., Franzen, T. M. O., Riseley, C. J., et al. 2020, PASA, 37, e018  
 Wilkinson, P. N., Booth, R. S., Cornwell, T. J., & Clark, R. R. 1984, Nature, 308, 619  
 Willett, K. W., Stocke, J. T., Darling, J., & Perlman, E. S. 2010, ApJ, 713, 1393  
 Wu, F., An, T., Baan, W. A., et al. 2013, A&A, 550, A113  
 Wu, Q. 2009, ApJ, 701, L95

**Table 1.** The CSO candidate sample collected in this paper.

Source name	Right ascension (h m s), declination ( $^{\circ}$ ' '')	$z$	Type	Ref.	Classification
J0003+2129	00:03:19.350009 +21:29:44.50822	0.450	Q	2	CJ
J0005+0524	00:05:20.215504 +05:24:10.80305	1.887	Q	2	CJ
J0048+3157	00:48:47.141485 +31:57:25.08483	0.015	G	2	CSO
J0119+3210	01:19:35.001084 +32:10:50.06103	0.0602	G	2	CSOc
J0650+6001	06:50:31.254327 +60:01:44.55477	0.455	Q	1,2	CSOc
J0741+2706	07:41:25.732847 +27:06:45.39211	0.772	Q	3	CSO
J0753+4231	07:53:03.337437 +42:31:30.76470	3.594	Q	1,3	CJ
J0831+4608	08:31:39.802592 +46:08:00.77140	0.131	G	3	CSOc
J0832+1832	08:32:16.040301 +18:32:12.13265	0.154	G	3	CSO
J0906+4636	09:06:15.539809 +46:36:19.02416	0.0847	G	3	CSOc
J0943+1702	09:43:17.223952 +17:02:18.96252	1.600	Q	3	CSO
J1110+4817	11:10:36.324124 +48:17:52.44997	0.742	Q	3	CSO
J1111+1955	11:11:20.065601 +19:55:36.00040	0.299	G	1,2,3	CSO
J1148+5924	11:48:50.358181 +59:24:56.38223	0.0108	G	1,3	CSOc
J1148+5254	11:48:56.569098 +52:54:25.32250	1.638	Q	2	CJ
J1158+2450	11:58:25.787561 +24:50:17.96392	0.203	G	3	CSO
J1234+4753	12:34:13.330774 +47:53:51.23687	0.373	Q	3	CSO
J1244+4048	12:44:49.187531 +40:48:06.16239	0.814	Q	1,3	CSO
J1247+6723	12:47:33.329586 +67:23:16.44894	0.107	G	2	CSO
J1254+1856	12:54:33.271499 +18:56:01.90866	0.125	G	3	CSOc
J1256+5652	12:56:14.233979 +56:52:25.23760	0.0417	G	2	CSO
J1309+4047	13:09:41.508928 +40:47:57.23878	2.908	Q	2	CSOc
J1310+3403	13:10:04.433638 +34:03:09.10854	0.960	G	3	CSO
J1311+1417	13:11:07.824225 +14:17:46.64778	1.955	Q	1	CJ
J1326+3154	13:26:16.511702 +31:54:09.52057	0.368	G	2,3	CSO
J1335+4542	13:35:21.962189 +45:42:38.23218	2.451	Q	2	CJ
J1358+4737	13:58:40.666477 +47:37:58.31155	0.230	G	3	CSO
J1407+2827	14:07:00.394417 +28:27:14.69011	0.077	G	2	CSO
J1511+0518	15:11:41.266365 +05:18:09.25931	0.084	G	2	CSO
J1559+5924	15:59:01.701929 +59:24:21.83416	0.060	G	2,3	CSOc
J1602+2418	16:02:13.838513 +24:18:37.79350	1.791	Q	3	CSO
J1616+0459	16:16:37.556823 +04:59:32.73651	3.215	Q	2	CJ
J1755+6236	17:55:48.435228 +62:36:44.12661	0.0276	G	2	CSO
J1815+6127	18:15:36.792244 +61:27:11.64744	0.601	Q	1	CSO
J1816+3457	18:16:23.901115 +34:57:45.74704	0.245	G	1,2	CJ
J1823+7938	18:23:14.108654 +79:38:49.00188	0.224	Q	1,2	CSO
J1945+7055	19:45:53.519774 +70:55:48.72880	0.101	G	1,2	CSO
J2022+6136	20:22:06.681748 +61:36:58.80472	0.227	G	1,2	CJ
J2245+0324	22:45:28.284742 +03:24:08.86404	1.350	Q	1	CJ
J2355+4950	23:55:09.458159 +49:50:08.33951	0.238	G	1,2	CSO

Column (1): source name. Column (2): Equatorial coordinates from Astrogeo (Petrov & Kovalev 2025). Column (3): Spectroscopic or photometric redshifts collected from the NASA/IPAC Extragalactic Database (<https://ned.ipac.caltech.edu/>) or SIMBAD (<https://simbad.u-strasbg.fr/>). Column (4) lists the optical identification of the source type from SIMBAD. Q – quasar; G – galaxy. Column (5) lists the references of the sources. Column (6) presents the classification of the radio morphology:

CSO – confirmed CSO with *Gaia*-identified AGN between two radio components; CJ – one-sided core–jet with *Gaia*-identified AGN at the end of the radio structure; CSO candidate – sources with large optical–radio offset remain as CSO candidates.

References: 1 – Peck & Taylor (2000); 2 – An & Baan (2012); 3 – Tremblay et al. (2016).

**Table 2.** Proper motions in the CSO sample.

Name	Comp.	$\mu_{\text{rad}}$ (mas yr $^{-1}$ )	$\beta_{\text{app}}$ (c)	$\text{PA}_{\text{var}}$ (° yr $^{-1}$ )	Age (yr)
J0832+1832	W-E	0.006±0.004	0.06±0.04	-0.01±0.06	1200±820
J0943+1702	N-S1	0.029±0.014	2.11±1.00	0.05±0.05	150±70
	S2-N	0.022±0.015	1.58±1.08	0.07±0.03	240±160
J1110+4817	SW-NE1	-0.078±0.015	-3.22±0.64	-0.02±0.08	>830
J1111+1955	W-E	0.295±0.062	5.55±1.16	-0.02±0.31	
J1158+2450	NE-C	0.001±0.006	0.01±0.08	-0.53±0.07	>1160
	NW-C	0.032±0.007	0.42±0.09	0.06±0.21	80±20
J1234+4753	SE-C	0.002±0.003	0.06±0.08	-0.01±0.06	>1840
	SE-NW	0.004±0.004	0.10±0.08	-0.02±0.05	1680±1400
J1244+4048	SW2-C	0.025±0.045	1.10±2.00	0.15±0.25	>130
J1247+6723	SE-NW	0.046±0.010	0.33±0.07	0.03±0.15	160±30
J1358+4737	W-E	0.021±0.004	0.31±0.06	0.07±0.10	250±50
J1407+2827	W-E	0.042±0.003	0.22±0.02	-0.24±0.04	160±10
J1511+0518	W-E	0.010±0.002	0.06±0.01	0.04±0.09	480±100
J1602+2418	W-E	0.033±0.006	2.54±0.45	0.43±0.12	80±10
J1815+6127	SW-NE1	-0.082±0.033	-2.88±1.16	-0.78±0.44	>160
	NE2-SW	-0.073±0.035	-2.56±1.21	-0.27±0.35	>200
J1823+7938	W2-E	0.006±0.008	0.09±0.12	-0.03±0.10	>1580
J1945+7055	SW2-NE3	0.021±0.006	0.14±0.04	-0.01±0.02	1030±270
	SW1-NE2	0.013±0.004	0.08±0.03	-0.13±0.06	720±220
	SW2-NE2	0.058±0.006	0.38±0.04	-0.08±0.03	280±30

Column (1): source name; Column (2): selected component with respect to the reference component used for proper motion measurement; Column (3): radial proper motion; positive values mean the components moving away from each other; Column (4): apparent radial separation speed measured in the units of  $c$  in the source rest frame; Column (5): position angle change, measured from north to east; Column (6): dynamical age of the component; if a component has negative or negligible proper motion, we used  $1-\sigma$  of the separation velocity to derive a lower limit (see [An et al. 2012](#)). The fitted proper motion plots are shown in Fig. B.5.

**Table 3.** CSO parameters used in Fig. 2.

Name	Radio power log(W Hz <sup>-1</sup> )	Projected size (pc)	Hotspot velocity (c)	Kinematic age (year)	Spectral index	Ref
J0038+2302	25.03	31.3	0.25	410	0.62	2
J0111+3906	28.10	39.0	0.34	380	0.62	2
J0119+3210	25.44	98.0	$\leq 0.64$	$\geq 500$	0.67	2
J0713+4349	27.38	146.0	0.51	930	0.48	2
J0832+1832	25.74	21.2	0.06	1200	0.74	1
J0943+1702	27.33	115.2	1.58	240	0.12	1
J1035+5628	27.36	181.8	0.96	620	0.81	2
J1110+4817	27.31	162.9	$\leq 0.64$	$\geq 830$	1.34	1
J1111+1955	26.79	75.7	$\leq 0.18$	$\geq 1360$	1.02	1,2
J1158+2450	25.92	28.9	0.08	1160	0.29	1
J1234+4753	26.20	49.9	0.10	1680	0.46	1
J1244+4048	27.21	220.4	$\leq 2.00$	$\geq 130$	0.63	1
J1247+6723	25.06	13.9	0.26	175	0.65	1,2
J1324+4048	27.06	32.7	0.12	870	0.94	2
J1326+3154	27.32	278.1	0.88	1030	0.66	1,2
J1335+5844	27.07	84.2	0.16	1800	0.04	2
J1358+4737	26.12	24.3	0.31	250	0.66	1
J1407+2827	25.85	11.1	0.13	255	0.36	1,2
J1414+4554	25.69	86.7	$\leq 0.16$	$\geq 1740$	0.78	2
J1415+1320	27.04	30.2	0.91	100	-1.11	2
J1511+0518	25.31	7.3	0.08	300	-0.51	1,2
J1602+2418	27.86	63.4	2.54	80	0.78	1
J1609+2641	27.71	290.0	0.63	1500	1.05	2
J1723+6500	24.48	2.8	$\leq 0.10$	$\geq 90$	0.4	2
J1734+0926	27.58	100.5	0.25	1300	0.75	2
J1815+6127	27.48	73.6	$\leq 1.21$	$\geq 200$	1.57	1
J1823+7938	25.74	56.5	$\leq 0.12$	$\geq 1580$	0.18	1
J1845+3541	27.55	31.0	0.55	180	0.62	2
J1939-6342	27.63	128.0	0.30	1400	1.62	2
J1944+5448	26.67	165.0	0.50	1080	0.78	2
J1945+7055	25.46	57.0	$\leq 0.19$	$\geq 1000$	0.54	1,2
J2022+6136	27.09	24.5	0.18	440	-0.23	2
J2203+1007	27.86	81.8	0.53	500	0.53	2
J2355+4950	26.81	179.2	0.31	1900	0.81	1,2

Column (1): source name; Column (2): radio power at 1.4 GHz; Column (3): projected linear size in pc; Column (4): hotspot separation velocity in c; Column (5): kinematic age; Column (6): spectral index calculated from 2–8 GHz from this paper or 5–8 GHz from [An & Baan \(2012\)](#); Column (7): references: 1 – this paper, 2 – [An & Baan \(2012\)](#); Note: Five sources in the *Gaia*+VLBI CSO sample are also included in [An & Baan \(2012\)](#), and for these sources, the data from [An & Baan \(2012\)](#) is used.

## Appendix A: Detailed sample construction

Our sample is constructed from three major CSO surveys and studies.

The COINS (CSOs Observed in the Northern Sky) sample was constructed in the early 1990s from a VLBI continuum survey of approximately 2000 compact radio sources, identifying 52 CSOs and candidates (Peck & Taylor 2000). This study included follow-up multi-frequency VLBI polarimetric observations of 33 sources from the COINS sample. They confirmed 10 CSOs, identified 29 candidates, and rejected 13 sources as core-jet quasars. High-quality VLBI images from this study distinguished CSOs from other AGN types by their well-defined lobes, edge-brightened hotspots, steep-spectrum emission, and symmetry in brightness between two lobes.

An & Baan (2012) compiled a sample of 46 CSOs and candidates from the literature and provided proper motion measurements for 24 sources, enabling the first statistical kinematic study of CSOs, offering valuable insights into their dynamical properties and evolutionary stages.

The VLBA Imaging and Polarimetry Survey (VIPS) at 5 GHz targeted 1127 sources, including COINS sample re-observations, and identified 103 CSO candidates (Taylor et al. 2005; Helmboldt et al. 2007). Tremblay et al. (2016) revisited the VIPS sample and confirmed 24 CSOs and 33 new candidates.

By integrating these studies and removing redundant sources, we achieved a comprehensive sample of 105 CSO candidates. While this merged sample inherits certain selection biases from its parent surveys, it represents the largest collection of well-studied CSO candidates to date.

The selection of sources was primarily based on:

- Symmetric radio morphology on parsec scales
- Steep spectrum in radio lobes
- Presence of edge-brightened hotspots
- When available, proper motion measurements consistent with young radio sources

Our approach of combining multiple surveys helps mitigate individual survey biases while maintaining a high standard for source inclusion. The resulting sample, though not strictly complete in a statistical sense, provides a robust foundation for studying CSO properties and testing new identification methods.

## Appendix B: Additional tables and figures

This section includes comprehensive tables detailing source properties, imaging parameters, and model-fitting results for our CSO classification. The full CSO candidate sample with coordinates, redshifts, optical identifications, and classifications are referred to Table 1. Table B.1 provides detailed astrometric measurements including angular scales, optical-radio position offsets, and *Gaia* quality metrics critical for our classification methodology. Tables B.2–B.4 present technical details of the VLBI imaging and spectral analysis that underpin our classifications.

Figures B.2–B.4 visualize the multi-frequency VLBI images, spectral index distributions, and *Gaia* position overlays that form the empirical foundation of our classification scheme. These reveal the distinct morphological characteristics that differentiate genuine CSOs from core-jet sources, with the *Gaia* positions critically demonstrating whether the optical AGN lies between symmetric radio components (confirming CSO nature) or at one end of the radio structure (indicating a core-jet source).

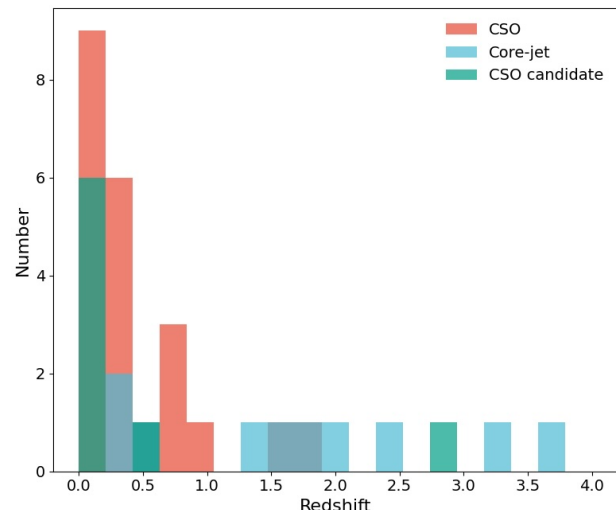


**Fig. B.1.** Redshift distribution of the sample. *Top panel*: Redshift distribution of quasars and galaxies within the sample. *Bottom panel*: Histograms showing the redshift distribution of confirmed CSO, CSO candidate (CSOc), and core-jet (CJ) sources.

## Appendix C: Gaia+VLBI cross-match

We compiled *Gaia* astrometric positions for our sources directly from the *Gaia* database<sup>1</sup>. For VLBI data, we used the Radio Fundamental Catalogue (RFC, Petrov & Kovalev 2025)<sup>2</sup>, which currently includes over 20,000 objects with typically sub-mas precision in absolute VLBI astrometry, achieved through observations from various astrometry and geodesy programmes. This precision makes the RFC an invaluable resource for aligning the optical and radio extragalactic reference frameworks (as demonstrated by Bourda et al. 2008).

In our analysis, we cross-matched the *Gaia* DR3 catalogue (Gaia Collaboration et al. 2016, 2023) with the VLBI sample from Section 2.2, employing a search radius of 1'' to identify optical counterparts to the radio sources (Fig. 1). Out of 105 VLBI-identified CSO candidates, 40 have *Gaia* counterparts (Fig. 1). The modest match rate (38%) provide important physical insight, suggesting that most CSO nuclei are optically faint or obscured, highlighting the fundamental challenge in CSO identification and the value of our combined *Gaia*+VLBI approach. This finding demonstrates why radio-only identification methods have proven insufficient and validates our multi-wavelength strategy. Since both *Gaia* and VLBI catalogues remain in continuous updates, the sample sizes analysed in this paper are slightly larger than in those used in previous studies.

The astrometric precision of both *Gaia* and VLBI is critical for aligning optical and radio positions. *Gaia* DR3 provides unprecedented astrometric precision with typical uncertainties of  $\sim 0.04$  mas for bright sources (apparent optical magnitude  $G < 14^{\text{mag}}$ ) and  $\sim 0.7$  mas for fainter sources ( $G = 20^{\text{mag}}$ ). The RFC delivers sub-mas astrometric accuracy for bright radio AGN, with typical uncertainties ranging from  $\sim 0.1$  to 1 mas. When combining *Gaia* and VLBI positions, the final uncertainty is estimated to be less than 1 mas for most sources, much smaller than the typical separation between the core and hotspots in CSOs (several to tens of mas), providing a robust foundation for the *Gaia*+VLBI method.

<sup>1</sup> <https://gea.esac.esa.int/archive/>

<sup>2</sup> <http://astrogeo.org/>

**Table B.1.** Properties of the CSO candidate sample collected in this paper.

Name	Type	Angular scale (mas)	Scale (pc)	Offset <sub>RA</sub> (mas)	Offset <sub>DEC</sub> (mas)	AEN (mas)	AENS	G (mag)
CSO								
J0048+3157	G	11.70	3.59	10.05±1.98	-40.93±1.30	9.21	418.29	17.95
J0741+2706	G	16.90	125.32	7.05±0.75	-0.04±0.75	0.00	0.00	19.49
J0832+1832	G	7.90	21.15	6.14±2.55	2.30±1.71	7.12	19.90	20.07
J0943+1702	Q	13.60	115.21	-2.07±8.09	7.06±10.00	1.95	0.38	20.88
J1110+4817	Q	22.30	162.87	-6.71±2.62	-10.33±2.63	3.08	1.28	20.73
J1111+1955	G	17.20	76.45	4.06±14.48	-5.80±9.15	18.47	107.18	21.25
J1158+2450	G	8.70	28.89	2.29±1.61	1.51±1.05	4.38	12.81	19.91
J1234+4753	Q	9.70	49.85	-0.97±0.41	0.90±0.38	0.20	2.24	16.84
J1244+4048	Q	29.20	220.43	-0.82±0.62	-0.61±0.80	0.00	0.00	19.75
J1247+6723	G	8.20	16.09	-12.73±5.52	10.37±3.90	18.62	89.49	20.23
J1256+5652	G	47.10	39.19	1.18±0.45	0.11±0.33	0.06	2.55	13.54
J1310+3403	G	15.50	122.88	3.28±6.98	5.62±6.60	9.59	26.84	21.10
J1326+3154	G	56.60	288.74	23.23±2.66	-25.85±2.36	8.56	10.49	20.94
J1358+4737	G	6.60	24.25	-3.15±2.81	1.69±3.19	10.92	101.41	20.59
J1407+2827	G	7.20	10.45	0.95±0.36	0.40±0.48	0.39	9.98	16.35
J1511+0518	G	5.00	7.89	5.74±0.68	-11.01±0.84	2.07	10.69	18.74
J1602+2418	Q	7.50	63.35	-4.92±0.36	1.98±0.53	0.05	0.04	18.02
J1755+6236	G	46.10	25.08	-6.46±2.00	0.40±1.65	2.72	2.17	20.10
J1815+6127	Q	11.00	73.59	0.17±0.95	-3.46±0.79	0.00	0.00	19.95
J1823+7938	Q	15.70	56.54	-3.11±1.51	3.60±0.98	3.24	8.21	19.85
J1945+7055	G	32.70	60.84	24.11±6.28	-22.00±6.23	27.65	225.44	20.85
J2355+4950	G	49.80	188.92	-5.34±5.82	9.04±5.42	26.44	113.70	21.13
Core-Jet								
J0003+2129	Q	4.20	24.19	5.58±4.24	-2.38±2.88	7.13	5.11	21.02
J0005+0524	Q	2.30	19.36	0.10±0.31	-0.24±0.53	0.00	0.00	16.10
J0753+4231	Q	12.00	86.99	0.80±0.44	2.02±0.47	0.22	0.53	17.90
J1148+5254	Q	7.90	66.92	-1.09±0.43	1.04±0.35	0.10	1.13	16.21
J1311+1417	Q	5.20	43.62	1.40±0.85	4.36±0.64	0.87	0.90	19.81
J1335+4542	Q	2.00	16.20	1.01±0.37	-0.47±0.39	0.00	0.00	17.70
J1616+0459	Q	...	...	-0.36±0.55	0.29±0.58	0.00	0.00	19.34
J1816+3457	G	35.90	138.21	-4.72±4.31	1.76±4.50	17.63	22.04	21.16
J2022+6136	G	7.10	25.83	13.18±3.26	12.20±4.54	8.92	13.09	20.68
J2245+0324	Q	10.70	89.96	0.00±0.47	0.21±0.64	0.00	0.00	18.81
CSO candidates								
J0119+3210	G	...	...	-246.77±12.29	58.43±10.31	36.83	193.96	20.37
J0650+6001	Q	6.80	39.41	-0.18±1.25	-3.06±1.33	1.02	0.32	20.72
J0831+4608	G	4.50	10.50	-6.99±6.10	-7.31±4.13	17.68	301.92	20.38
J0906+4636	G	1.70	2.71	-5.69±1.08	7.85±1.06	4.23	30.38	19.26
J1148+5924	G	22.80	5.60	-91.04±10.14	68.36±14.50	33.91	417.58	19.15
J1254+1856	G	3.30	6.90	-11.58±2.19	14.69±1.92	8.64	66.16	19.88
J1309+4047	Q	1.30	10.09	-0.82±1.29	-3.89±1.33	0.14	0.24	18.19
J1559+5924	G	7.80	9.07	25.83±2.40	7.88±2.41	9.98	61.47	19.25

Column (1): source name; Column (2): host galaxy type from SIMBAD. SG, S1G or S2G – Seyfert galaxy or Seyfert 1, 2 galaxy; RG – radio galaxy; Column (3): angular size of the source from our images in mas; Column (4): linear scale of the sources in pc;

Column (5)–(6): angular distance (in mas) between the X-band core (peak) and the *Gaia* position along RA ( $\Delta_{RA}\cos\delta$ ) and DEC( $\Delta_{DEC}$ ); Column (7): astrometric excess noise factor from *Gaia* DR3; Column (8): astrometric excess noise significance from *Gaia* DR3; Column (9): mean G-band magnitude from *Gaia* DR3.

Table B.1 presents the CSO candidate sample collected in this study, detailing key parameters such as host galaxy type, angular scale, and astrometric offsets between VLBI and *Gaia* positions. The majority of the CSOs and candidates in this sample are clustered at moderate redshifts ( $z < 1.0$ ), while core-jet sources show a broader redshift range, often extending to higher redshift values (Fig. B.1). This distribution likely reflects both physical differences in the populations and selection effects, with CSOs lacking the Doppler-boosted emission that makes core-jet sources detectable at higher redshifts.

The cross-matched CSO candidates include a heterogeneous mix of quasars, radio galaxies, and other AGN types, with quasars making up  $\sim 40\%$  of the matches. This prevalence of quasars reflects multiple factors: *Gaia*'s sensitivity to point-like optical sources, the higher intrinsic luminosity of quasars enabling detection at greater distances, and VLBI survey biases favoring sources with compact, bright radio components (Petrov et al. 2019). Understanding these selection effects is crucial when interpreting our results and their implications for CSO evolution.

**Table B.2.** Image parameters of 22 confirmed CSOs shown in Fig. B.2.

Name	Epoch	Freq. (GHz)	$S_{\text{peak}}$ (mJy beam $^{-1}$ )	$\sigma$ (mJy beam $^{-1}$ )	$\theta_{\text{beam}}$ (mas, mas, °)
J0048+3157	2018-09-01	8.7	269.3	0.21	(1.0, 2.1, -7.3)
		2.3	105.7	0.52	(3.6, 8.2, -7.8)
J0741+2706	2018-11-18	8.7	245.3	0.17	(1.1, 2.3, -9.7)
		2.3	732.6	0.55	(3.6, 8.8, -10)
J0832+1832	2017-06-10	8.7	116.7	0.23	(1.1, 2.1, 1.0)
		2.3	231.8	0.48	(3.8, 7.7, 0.0)
J0943+1702	2017-08-05	8.7	188.3	0.21	(1.0, 2.4, -7.8)
		2.3	122.5	0.37	(3.7, 9.1, -9.5)
J1110+4817	2018-02-09	8.7	37.7	0.24	(1.2, 1.7, -21.2)
		2.3	175.5	0.56	(4.5, 6.7, -21.1)
J1111+1955	2018-03-26	8.7	68.9	0.30	(1.1, 2.4, -7.7)
		2.3	498.8	0.85	(3.7, 9.4, -7.0)
J1158+2450	2017-05-01	8.7	301.5	0.31	(1.0, 1.9, -1.5)
		2.3	423.6	0.91	(4.1, 7.5, -3.4)
J1234+4753	2018-06-09	8.7	142.3	0.19	(1.1, 1.5, 1.7)
		2.3	208.9	0.46	(4.1, 5.5, -1.2)
J1244+4048	2018-07-01	8.7	86.8	0.53	(1.1, 1.6, 9.3)
		2.3	142.9	0.69	(3.8, 6.1, 3.3)
J1247+6723	2017-05-27	8.7	57.8	0.22	(1.3, 1.5, -22.7)
		2.3	138.7	0.30	(4.6, 5.4, -20.8)
J1256+5652	2018-12-04	8.7	283.7	0.17	(1.1, 1.3, 13.8)
		2.3	148.2	0.37	(4.3, 5.3, 12.4)
J1310+3403	2006-07-17	4.8	46.6	0.25	(1.9, 2.9, -7.3)
J1326+3154	2011-05-15	8.7	77.1	0.52	(1.1, 2.0, 3.4)
		2.3	459.2	2.72	(3.8, 7.1, -2.1)
J1358+4737	2017-08-12	8.7	172.3	0.25	(1.1, 1.6, 1.8)
		2.3	480.0	0.42	(3.9, 5.7, 0.7)
J1407+2827	2018-08-14	8.7	537.5	2.30	(1.3, 2.7, -23.4)
		2.3	1312.3	1.83	(4.4, 11.2, -27.4)
J1511+0518	2017-02-20	8.7	349.5	0.29	(0.9, 2.0, -0.1)
		2.3	263.0	0.62	(3.4, 7.7, -3.2)
J1602+2418	2018-04-29	8.7	50.3	0.19	(0.9, 1.9, 0.0)
		2.3	214.6	0.54	(3.7, 7.6, -3.1)
J1755+6236	2018-12-20	8.7	26.2	0.23	(1.2, 2.0, 69.2)
		2.3	43.3	0.72	(4.6, 11.6, -45.1)
J1815+6127	2017-01-16	8.7	92.0	0.26	(1.4, 1.7, 24.5)
		2.3	403.9	0.47	(5.4, 6.3, 21.9)
J1823+7938	2000-12-04	8.6	182.4	0.32	(1.1, 1.6, 46.5)
		2.3	185.7	2.62	(4.9, 6.1, 41.3)
J1945+7055	2018-12-10	8.7	65.8	0.28	(1.1, 1.5, 25.1)
		2.3	338.4	0.86	(3.9, 5.3, 20.2)
J2355+4950	2017-04-25	8.6	259.4	0.91	(1.2, 1.5, 57.3)
		2.3	892.3	1.27	(3.7, 4.2, 70.3)

Column (1): source name; Column (2): observing epoch; Column (3): frequency; Column (4): peak intensity; Column (5): rms noise of the post-fit image; Column (6): restoring beam shape (major axis, minor axis, and position angle of the elliptical Gaussian beam; the position angle is measured from north to east).

The astrometric excess noise (AEN) from *Gaia*, presented in Table B.1, offers valuable insights into the host galaxy properties. AEN values for CSOs are consistently larger than those for core-jet sources, while CSO candidates exhibit even higher AEN values than confirmed CSOs. This trend aligns with the observational evidence that CSOs are predominantly hosted by galaxies, whereas core-jet sources are typically associated with quasars, whose compact, bright nuclei dominate their optical emission. The higher AEN values for CSOs likely reflect the extended and complex optical morphologies of their host galaxies, which can introduce additional scatter in *Gaia*'s astrometric measurements. In contrast, the lower AEN values for core-jet sources corre-

spond to the more point-like optical appearance of quasars, dominated by bright nuclear emission. These variations in AEN provide a quantitative measure that complements radio-based classifications and offer important insights into the diverse optical characteristics of AGN hosts.

In typical AGN dominated by compact radio cores, the image centre aligns with the actual source coordinate. However, in CSOs, where emission is dominated by lobes and hotspots, self-calibration in VLBI processing can shift the image centre to the brightest component, which may not be the core. To reconcile *Gaia* positions with VLBI images, we implemented rigorous astrometric corrections, leveraging absolute RFC positions de-

**Table B.3.** Image information of the 10 confirmed core–jet sources shown in Fig. B.3 and B.6.

Name	Epoch	Freq. (GHz)	$S_{\text{peak}}$ (mJy beam $^{-1}$ )	$\sigma$ (mJy beam $^{-1}$ )	$\theta_{\text{beam}}$ (mas, mas, °)
J0003+2129	2018-07-01	8.7	123.4	0.23	(1.7, 2.6, -14.2)
		2.3	160.3	0.44	(3.6, 8.1, -4.5)
J0005+0524	2018-11-03	8.7	74.2	0.21	(1.0, 2.4, -4.4)
		2.3	165.6	0.42	(3.8, 10.1, -7.2)
J0753+4231	2018-06-09	8.7	120.0	0.21	(1.2, 1.7, 10.7)
		2.3	300.1	0.64	(4.0, 6.2, 3.6)
J1148+5254	2017-08-05	8.7	465.9	0.32	(1.2, 1.4, 10.3)
		2.3	241.6	0.46	(4.3, 5.4, 10.0)
J1311+1417	2018-12-10	8.7	75.3	0.15	(2.3, 1.0, -4.4)
		2.3	520.8	0.32	(9.9, 3.4, -9.4)
J1335+4542	2017-07-16	8.7	515.6	0.30	(1.0, 1.5, 3.0)
		2.3	473.1	0.55	(3.8, 5.8, -0.9)
J1616+0459	2009-05-14	8.6	542.7	0.57	(1.1, 2.3, 3.4)
		2.3	592.6	0.61	(4.9, 8.7, 5.0)
J1816+3457	2017-03-23	8.7	52.5	0.57	(1.2, 2.6, 7.5)
		2.3	187.8	0.72	(4.5, 9.0, 5.4)
J2022+6136	2015-08-24	7.6	1268.9	0.76	(1.3, 2.7, -53.4)
		4.3	1114.0	1.81	(2.3, 4.8, -55.9)
J2245+0324	2018-11-18	8.7	176.9	0.23	(1.1, 2.4, 3.5)
		2.3	316.4	0.48	(4.1, 9.3, -1.8)

Column (1): source name; Column (2): observing epoch; Column (3): frequency; Column (4): peak intensity; Column (5): rms noise of the post-fit image; Column (6): restoring beam shape (major axis, minor axis, and position angle of the elliptical Gaussian beam; the position angle is measured from north to east).

**Table B.4.** Image information of the remaining 8 unclassified sources shown in Fig. B.4.

Name	Epoch	Freq. (GHz)	Peak (mJy/b)	$\sigma$ (mJy/b)	$\theta_{\text{beam}}$ (mas, mas, °)
J0119+3210	2017-06-10	8.7	61.6	0.97	(2.3, 1.2, -4.4)
		2.3	220.1	8.54	(4.2, 8.3, -4.5)
J0650+6001	2017-07-16	8.7	573.7	0.52	(1.1, 1.3, 36.8)
		2.3	775.3	0.62	(4.8, 4.2, 33.2)
J0831+4608	2006-05-31	4.8	44.8	0.27	(2.0, 2.6, -12.6)
J0906+4636	2017-07-16	8.7	95.7	0.24	(1.0, 1.5, 11.8)
		2.3	70.6	0.48	(4.0, 5.9, 10.7)
J1148+5924	2017-08-05	8.7	187.7	0.31	(1.2, 1.4, 13.8)
		2.3	115.9	0.71	(4.5, 5.4, 12.3)
J1254+1856	2006-02-25	8.4	78.3	0.22	(1.1, 2.5, 5.3)
		4.8	75.5	0.25	(2.1, 3.4, -3.5)
J1309+4047	2022-07-26	7.6	36.8	0.42	(2.6, 0.9, 4.5)
		2.3	77.1	0.41	(1.5, 4.4, 1.5)
J1559+5924	2017-05-12	8.7	43.4	0.21	(1.2, 1.4, -66.2)
		2.3	113.5	0.43	(4.9, 5.5, -45.9)

Column (1): source name; Column (2): observing epoch; Column (3): frequency; Column (4): peak intensity; Column (5): rms noise of the post-fit image; Column (6): restoring beam shape (major axis, minor axis, and position angle of the elliptical Gaussian beam; the position angle is measured from north to east).

rived from group–delay measurements at S- and X-band (central frequencies at 2.3 and 8.4 GHz) minimally affected by source structure and calibration errors (Porcas 2009). This critical step ensures accurate registration between optical and radio reference frames, forming the foundation of our classification methodology.

Additionally, we account for frequency-dependent core shifts using multi-frequency VLBI data whenever available (Lobanov 1998), where a robust optically thin jet component was used for each source. This correction is essential for accurate VLBI component identification across different observ-

ing frequencies and prevents potential misclassifications due to frequency-dependent position shifts.

This *Gaia*+VLBI method provides a uniquely powerful and precise approach to confirming genuine CSOs, overcoming the fundamental limitations of traditional morphological analyses that relied on detecting often invisible radio cores. By definitively pinpointing the AGN position, our approach enables accurate determination of radio structure orientation and detailed study of jet kinematics, significantly enhancing our understanding of CSO physics and their evolutionary pathways.

**Table B.5.** Proper motions of the core–jet sample in Fig. B.6.

Name	Comp.	$\mu_{\text{rad}}$ (mas yr $^{-1}$ )	$\beta_{\text{app}}$ (c)	$\text{PA}_{\text{var}}$ (° yr $^{-1}$ )
J0003+2129	J2	0.055±0.002	1.50±0.04	0.49±0.01
	J1	0.058±0.008	1.57±0.23	-0.04 ± 0.08
	J1	0.070±0.001	5.55±0.10	-1.36 ± 0.12
J0005+0524	J1	0.031±0.004	2.54±0.32	-0.16 ± 0.07
	J3	0.025±0.001	2.28±0.05	-0.53 ± 0.47
	J2	0.022±0.001	2.03±0.05	0.02±0.05
J1311+1417	J1	0.050±0.001	4.53±0.11	0.02±0.02
	J2-J1	0.083±0.001	1.20±0.01	0.02±0.03
	J1	0.010±0.001	0.67±0.05	-0.14 ± 0.01
J1335+4542				
J2022+6136				
J2245+0324				

Column (1): source name; Column (2): component ID; Column (3): radial proper motion of the component with respect to the core; Column (4): position angle change of the component with respect to the core, measured from north to east.

## Appendix D: VLBI data reduction and analysis

### Appendix D.1: Continuum images

We obtained archive VLBI data for 40 CSO candidates from the Astrogeo database. Most of these data originate from astrometric VLBI projects, such as the VLBA Calibrator Surveys (e.g. Beasley et al. 2002; Fomalont et al. 2003; Petrov et al. 2005, 2006; Kovalev et al. 2007; Petrov et al. 2008; Petrov 2016), and consist of pre-processed and self-calibrated visibility data, often including simultaneous S-band (2.3 GHz) and X-band (8.4 GHz) observations. For these pre-calibrated datasets, we used standard hybrid mapping using the software package DIFMAP (Shepherd 1997), iteratively performing CLEAN deconvolution and self-calibration to refine the imaging quality.

We implemented a rigorous quality control process, inspecting each dataset and selecting epochs with optimal signal-to-noise ratio and  $(u, v)$ -coverage at X-band to ensure the highest possible fidelity in our resulting images. When X-band data were unavailable, we substituted C-band (4.8 GHz) observations, maintaining consistent resolution across the sample. Continuum images were produced for each selected epoch, with *Gaia* DR3 positions overlaid to compare the optical centroid with the VLBI radio structure, focusing on the core identification (Figs. B.2, B.3, and B.4). This approach allows us to directly assess the alignment between the optical and radio emission, aiding in CSO classification and understanding source morphology.

### Appendix D.2: Spectral index map

Accurate spectral index measurements require quasi-simultaneous multi-frequency observations. The simultaneous dual-frequency (2.3/8.4 GHz) VLBI data from the astrometry program provide an ideal opportunity to construct reliable spectral index maps largely free from variability effects, offering critical diagnostic information about emission mechanisms in different regions of the source.

We first produced FITS images from both the S- and X-band data, ensuring same pixel size and map dimensions. If S-band data were unavailable, C-band images were used as a substitute. We then convolved the higher-resolution X-band images with a beam matching that of the lower-frequency images to maintain consistent resolution across frequencies. This is a crucial step for accurate spectral index calculations.

To ensure precise alignment of multi-frequency images, a critical requirement for meaningful spectral analysis, we used optically thin, steep-spectrum components (typically hotspots or lobes) as reference points. These features are less affected

by frequency-dependent position shifts and maintain consistent positions. Only sources with reliable component identification were used for spectral index mapping. The images were shifted based on calculated offsets to guarantee that the same physical components were superimposed across frequencies.

The resulting spectral index distributions for each CSO and core–jet source are shown in Figs. B.2 and B.3. Spectral index maps help distinguish between core and jet components: cores typically exhibit flat or inverted spectra ( $\alpha \lesssim 0.5$ ), while jets and hotspots have steep spectra ( $\alpha \gtrsim 0.5$ ) (Kellermann et al. 1994). This additional spectral information enhances source classification and helps elucidate their physical properties. For J1310+3403, only 4.8-GHz data were available from the archive, so a spectral index map could not be constructed. For the CSOs, we made spectral index maps, except for J0119+3210, J0906+4636 and J0831+4608. The first two sources lack reliable optically thin components for alignments and the last one only has 4.8-GHz data from the archive (see Fig. B.4).

### Appendix D.3: Proper motion analysis

Proper motion measurements help constrain CSO expansion speeds, which are crucial for estimating kinematic ages and understanding evolutionary stages. In core–jet sources, jet speeds provide insights into jet dynamics and relativistic beaming effects. We analyzed the kinematics of CSOs and core–jet sources using multi-epoch VLBI data. In CSOs, we measured the separation speed between terminal hotspots or hotspot–core, while in core–jet sources, we tracked jet components relative to the core.

We used the MODELFIT task in DIFMAP, employing circular Gaussian components to represent emission features. This approach provided a simple and consistent model for the compact structures observed. Given the varying data quality across epochs, we focused on fitting the brightest components that could be reliably identified across all epochs.

If two components were too close or if the deconvolved size was significantly smaller than the restoring beam, we replaced the Gaussian with a point-source model. Our primary concern was determining component positions accurately rather than modeling exact shapes or sizes; thus, using circular Gaussians or point sources did not significantly affect the proper motion results.

Table G.1 lists the model fitting parameters, including integrated flux density ( $S_{\text{tot}}$ ), radial separation ( $R$ ) with respect to the *Gaia* position and the position angle (PA) measured from north to east, component size  $\theta_{\text{FWHM}}$  (full width at half maximum of

the fitted Gaussian), and brightness temperature ( $T_b$ ). The error estimates are described in Appendix E.

Of these identified CSO and core-jet sources, 21 have multiple X-band VLBI epochs, allowing measurement of hotspot separation speeds or jet proper motions over time baselines ranging from a few years to 25 years (the earliest data are from 1994). For sources with more than two epochs available, we derived proper motions using linear regression of component positions over time. For those with only two epochs, we calculated apparent speeds based on positional changes between these epochs.

Two sources (e.g. J1755+6236/NGC 6251, J2355+4950) were excluded from proper motion analysis due to insufficient time baselines, poor data quality, or ambiguous component identification. In some CSOs, we also measured the proper motions of inner jet components in addition to terminal hotspots to gain further insights into kinematics and dynamical evolution.

#### Appendix D.4: Error analysis and identification reliability

To ensure the robustness of our CSO identifications, we conducted a comprehensive error analysis incorporating all potential sources of uncertainty in both *Gaia* and VLBI measurements. *Gaia* position errors range from 0.04 to 0.7 mas. Chromatic errors arising from the wavelength-dependent point-spread function of the *Gaia* optics can shift positions, particularly for AGN with significant ultraviolet or infrared emission (Lindegren et al. 2018). Proper motion and parallax uncertainties were accounted for, though they are generally negligible for distant extragalactic sources (Fabricius et al. 2021).

For VLBI measurements, we accounted for thermal noise, tropospheric delay (introducing position errors of  $\sim 0.1\text{--}1$  mas), and ionospheric effects, which are more pronounced at lower frequencies (Sovers et al. 1998). Source structure effects were critically assessed, as extended or complex radio morphologies can cause significant astrometric shifts if not properly modeled (Charlot 1990; Porcas 2009). This is especially relevant for CSOs, where core emission is often weak or obscured, and dominant emission arises from the lobes or hotspots.

*Gaia* and VLBI position errors were combined in quadrature, providing a conservative estimate of the total uncertainty in optical–radio alignment. We used a Monte Carlo approach, generating 1000 realizations of *Gaia* and VLBI positions for each source, based on Gaussian error distributions. For each realization, we calculated the offset between *Gaia* and VLBI positions, determining the likelihood that the optical position matches a particular radio component.

This comprehensive error analysis enhances the credibility of our results and allows for nuanced interpretation of borderline cases, contributing to refined CSO identification methodologies. By quantifying the reliability of each identification, we provide a solid foundation for subsequent analyses of CSO properties, such as kinematic ages and expansion speeds, and demonstrate the power of combining optical and radio astrometry for future studies.

#### Appendix E: Error analysis of the VLBI components

The errors of the fitted Gaussian components are mainly introduced by Fomalont (1999) and modified for the strong side lobes

of VLBI observations:

$$\text{SNR} = \frac{S_{\text{peak}}}{\sigma_{M,\text{peak}}} \quad (\text{E.1})$$

$$\sigma_{\text{peak}} = \sigma \quad (\text{E.2})$$

$$\sigma_{\text{int}} = \sigma \times \sqrt{1 + \frac{S_{\text{int}}}{S_{\text{peak}}}} \quad (\text{E.3})$$

$$\sigma_{\text{pos}} = \frac{\theta_{\text{beam}}}{2 \text{ SNR}} \quad (\text{E.4})$$

$$\sigma_{\text{size}} = \frac{\theta_{\text{beam}}}{2 \text{ SNR}} \quad (\text{E.5})$$

$$\sigma_{\text{PA}} = \arctan\left(\frac{\sigma_{M,\text{pos}}}{R}\right), \quad (\text{E.6})$$

where  $\text{rms}$  is the post-fit root-mean-square error of the image,  $S_{\text{peak}}$  the peak intensity of the component,  $S_{\text{tot}}$  the total integrated flux density, beam is the full width at half maximum (FWHM) size of the restoring beam,  $\sqrt{b_{\text{maj}} \cdot b_{\text{min}}}$ , and  $R$  the radial distance of the component with respect to the core.

Additional calibration errors depend on the accuracy of the visibility amplitude calibration. According to the VLBA observational status report<sup>3</sup>, the fractional calibration error for flux density is about 5% at 1.5–15 GHz frequency bands. We thus apply 5% as the calibration error for the peak intensities and total flux densities.

#### Appendix F: Core brightness temperature

The brightness temperatures  $T_B$  were calculated using the following equation from Kellermann & Owen (1988):

$$T_B = 1.22 \times 10^{12} \text{ K} \left( \frac{S_{\text{tot}}}{\text{Jy}} \right) \left( \frac{\theta_{\text{FWHM}}}{\text{mas}} \right)^{-2} \left( \frac{\nu}{\text{GHz}} \right)^{-2} (1+z), \quad (\text{F.1})$$

where  $\nu$  is the observing frequency,  $z$  is the redshift,  $\theta_{\text{FWHM}}$  is the component's angular size, and  $S_{\text{tot}}$  is the integrated flux density of the component. We only calculated the brightness temperatures of the core and bright hotspot components.

#### Appendix G: The reliability of *Gaia* positions correlating with VLBI observations

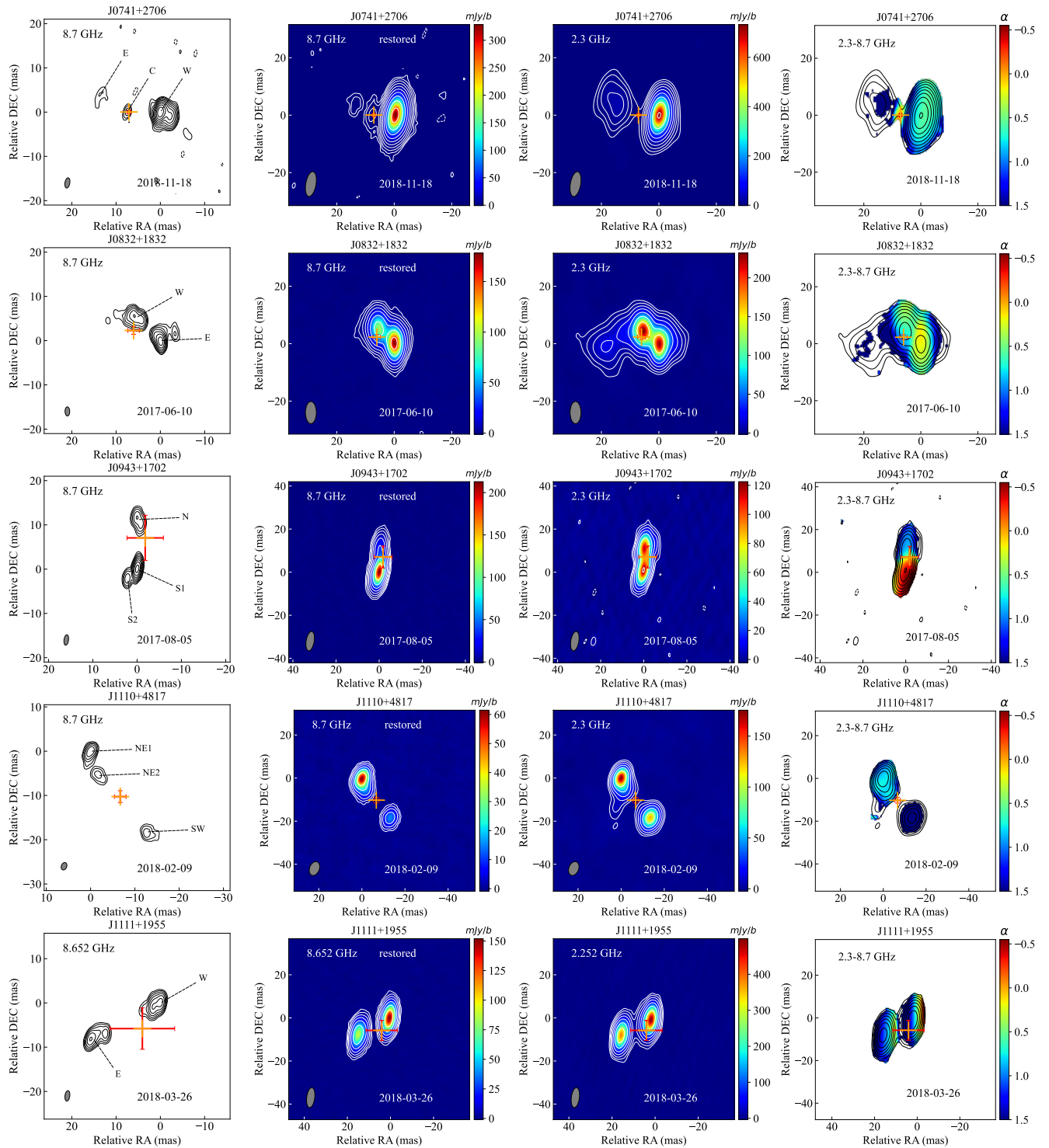
Besides looking for CSOs, *Gaia* astrometry has also been used to search for dual AGN, incorporating radio observations (e.g. Chen et al. 2023b; Schwartzman et al. 2024). In those studies, two special parameters from *Gaia* tables, namely AEN (astrometric excess noise) and AENS (astrometric excess noise significance) characterising the so-called ‘astrometric jittering’, are used to select parent samples for their research by combining with the optical *G*-band magnitudes. In principle, AEN and AENS represent how well the best-fitting standard astrometric model (using five astrometric parameters) agrees with the source observations. From this perspective, if  $AENS \geq 2$  for a given source, then AEN is significant, and it can be inferred that the residuals of the fit exhibits statistically larger values than expected (see Lindegren et al. 2012, and the *Gaia* DR3 documentation<sup>4</sup>). Physically, significant AEN values and large AENS values could be caused by an optically extended host galaxy or optically variable sub-kpc jets and knots. This mainly happens for

<sup>3</sup> <https://science.nrao.edu/facilities/vlba/docs/manuals/oss>

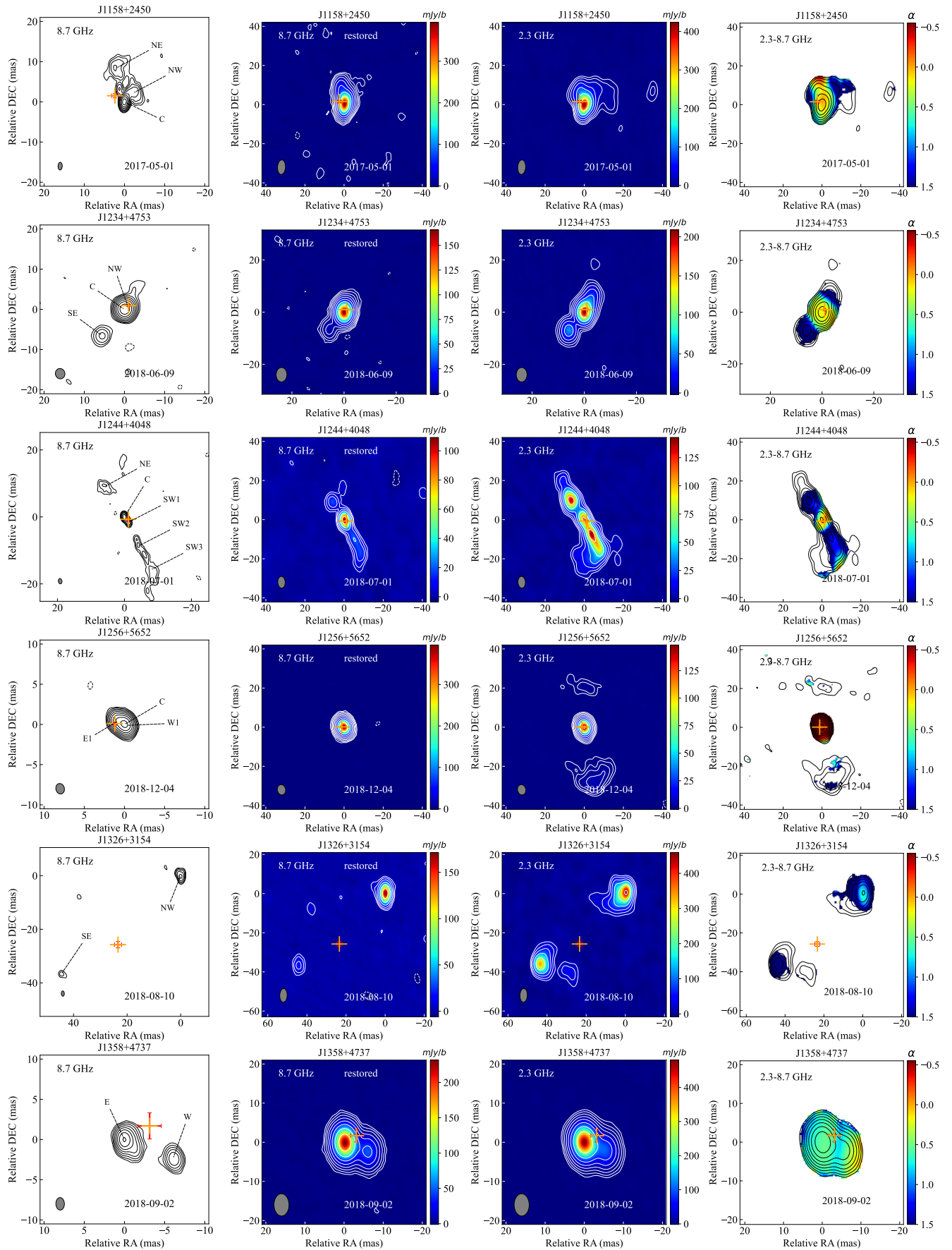
<sup>4</sup> [https://gea.esac.esa.int/archive/documentation/GDR3/pdf/GaiaDR3\\_documentation\\_1.2.pdf](https://gea.esac.esa.int/archive/documentation/GDR3/pdf/GaiaDR3_documentation_1.2.pdf)

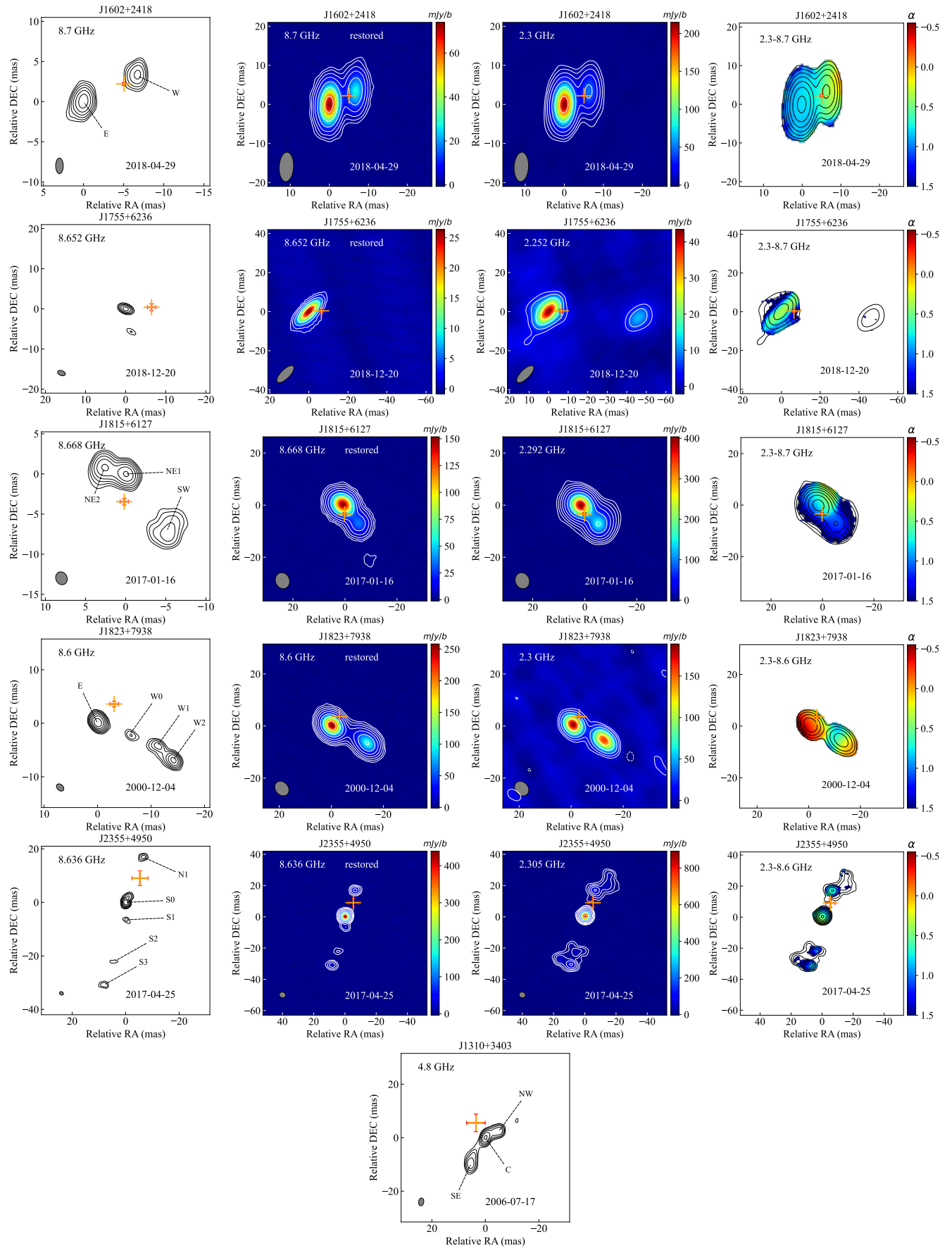
galaxies at low redshifts (e.g.  $z < 0.5$ , Hwang et al. 2020). If the above contamination can be excluded, dual or off-nucleus AGN could be expected (e.g. Hwang et al. 2020; Shen et al. 2021).

In their search for dual AGN candidates, Schwartzman et al. (2024) used AENS  $> 5$ , *Gaia*  $G$  magnitude  $G < 20$ , and redshift  $z > 0.5$  criteria to mitigate the effect of large extended host galaxies which can easily exhibit spurious AENs. Some studies (e.g. Chen et al. 2023b; Wang et al. 2023c) also presented the distribution of the AEN and  $G$  magnitude values in the samples, to give reasonable cutouts for certain subsamples. Our Table B.1 presents the source VLBI scale as well as the AEN, AENS and  $G$  magnitude information. From our sample, we can find that our confirmed CSOs and CSO candidates tend to gather the ‘jittering’ sources, while the confirmed sources with redshift above 0.5 have clear *Gaia* detections. This can be taken as a sign that our selected CSOs and CSO candidates are mostly from extended optical galaxies.



**Fig. B.2.** The *Gaia* position (marked as a cross) overlaid on the VLBI image of confirmed CSOs. Note the different scales of the left panel and middle panels, with the former one highlighting the fine structure of the radio source revealed by the full-resolution 8-GHz VLBI image. In the spectral index map (right panel), the colour scale represents the spectral index distribution, and the contours show the 2.3-GHz intensity. To show clearly, the error bars in *Gaia* positions for J0741+2706, J1244+4048, J1602+2418 are three times of the actual errors, while for J1234+4753 it is 10 times and for J1256+5652 it is 100 times. These sources show *Gaia* positions near the central core location or the geometric centre, offering strong evidence for CSOs. The colour scale and contour levels represent the intensity. The lowest contour denotes 3 times the image noise, and other contours increase by a factor of 2. Four sources (J0048+3157, J1247+6723, J1511+0518, and J1945+7055) show obvious offsets between their *Gaia* positions and VLBI stuctures, their identification of CSO are discussed in Section 3.1. Source J1310+3403 has only C-band (4.8 GHz) image for analysis.


**Fig. B.2.** Continued.

**Fig. B.2.** Continued.

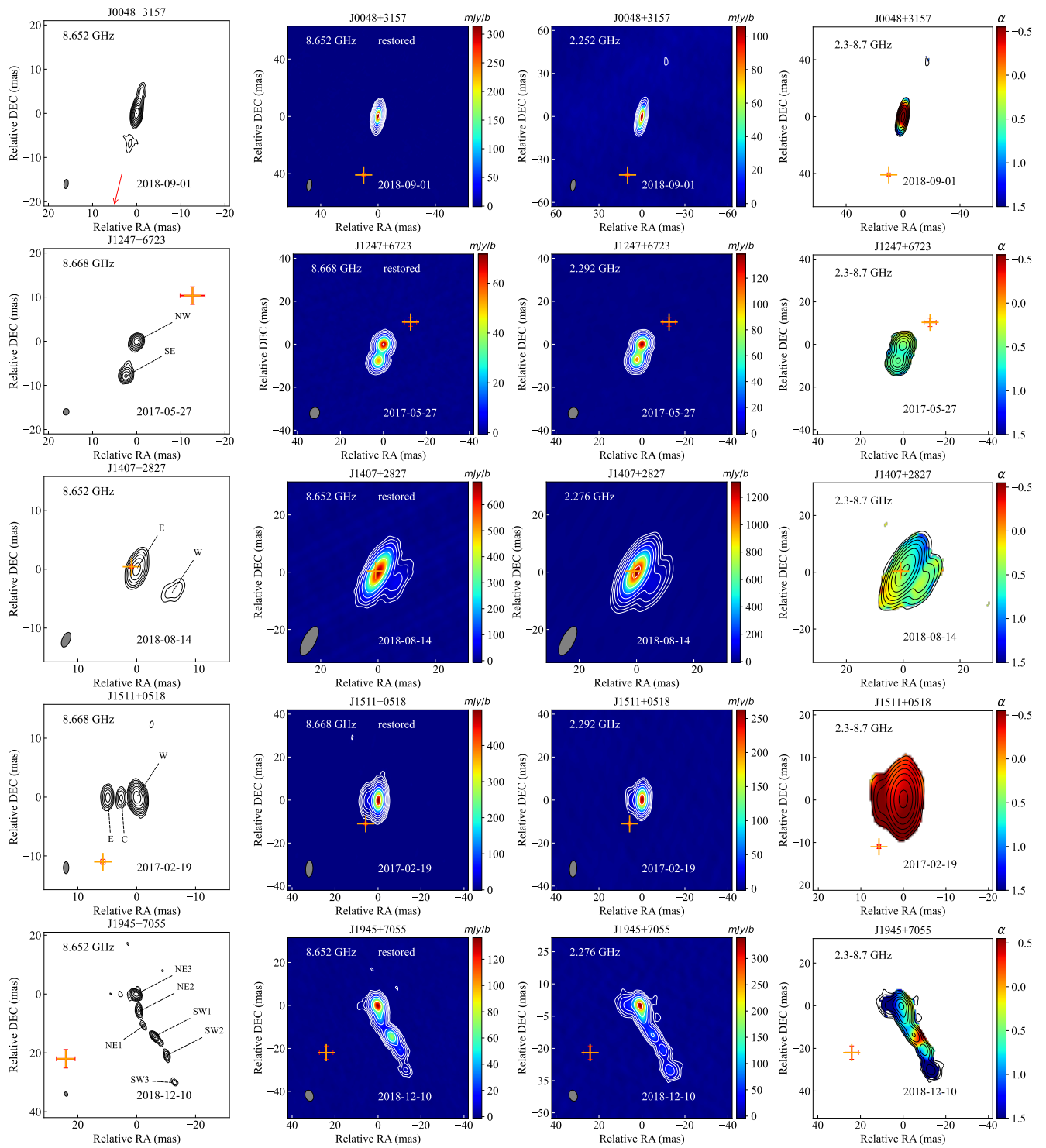
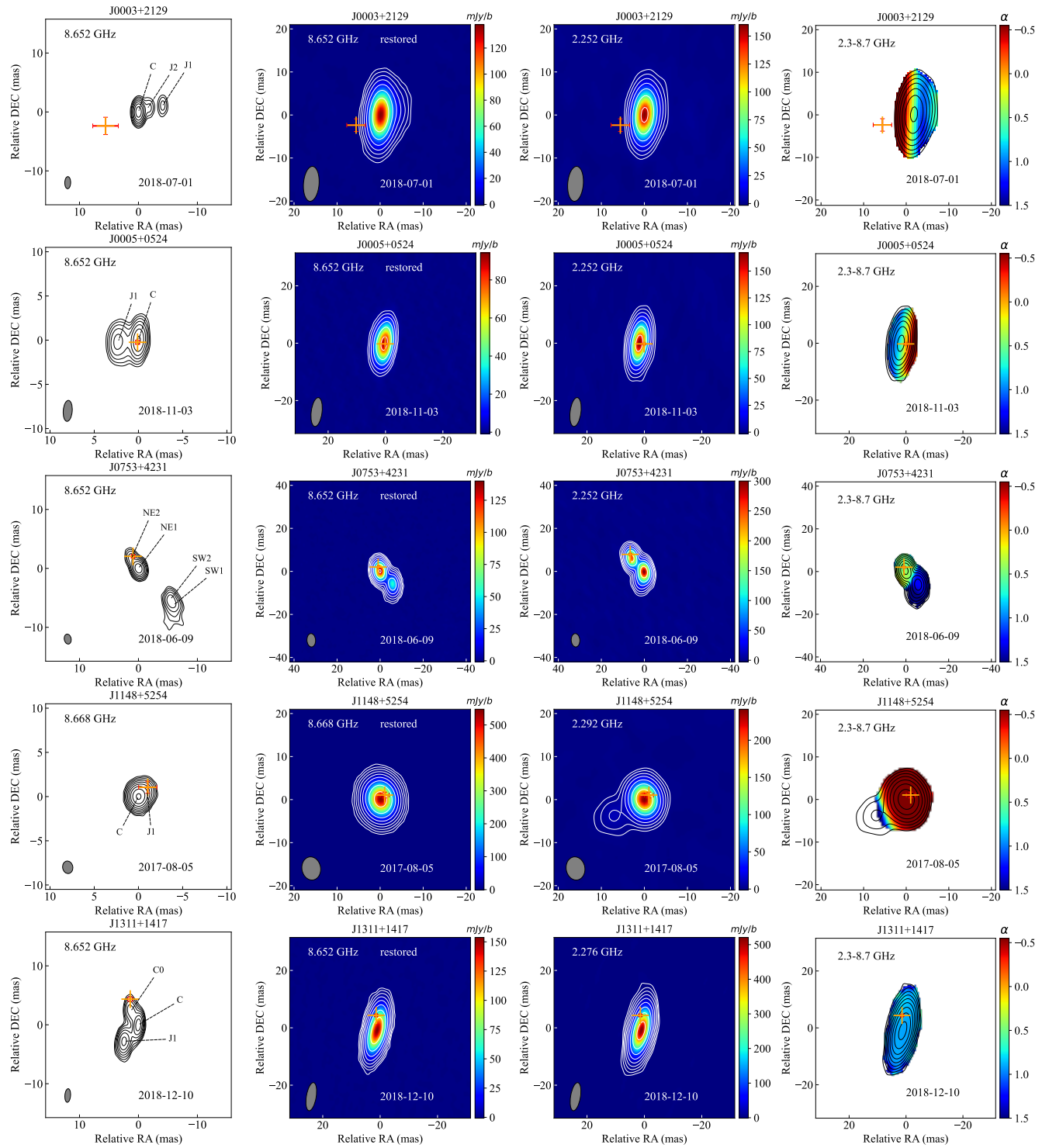
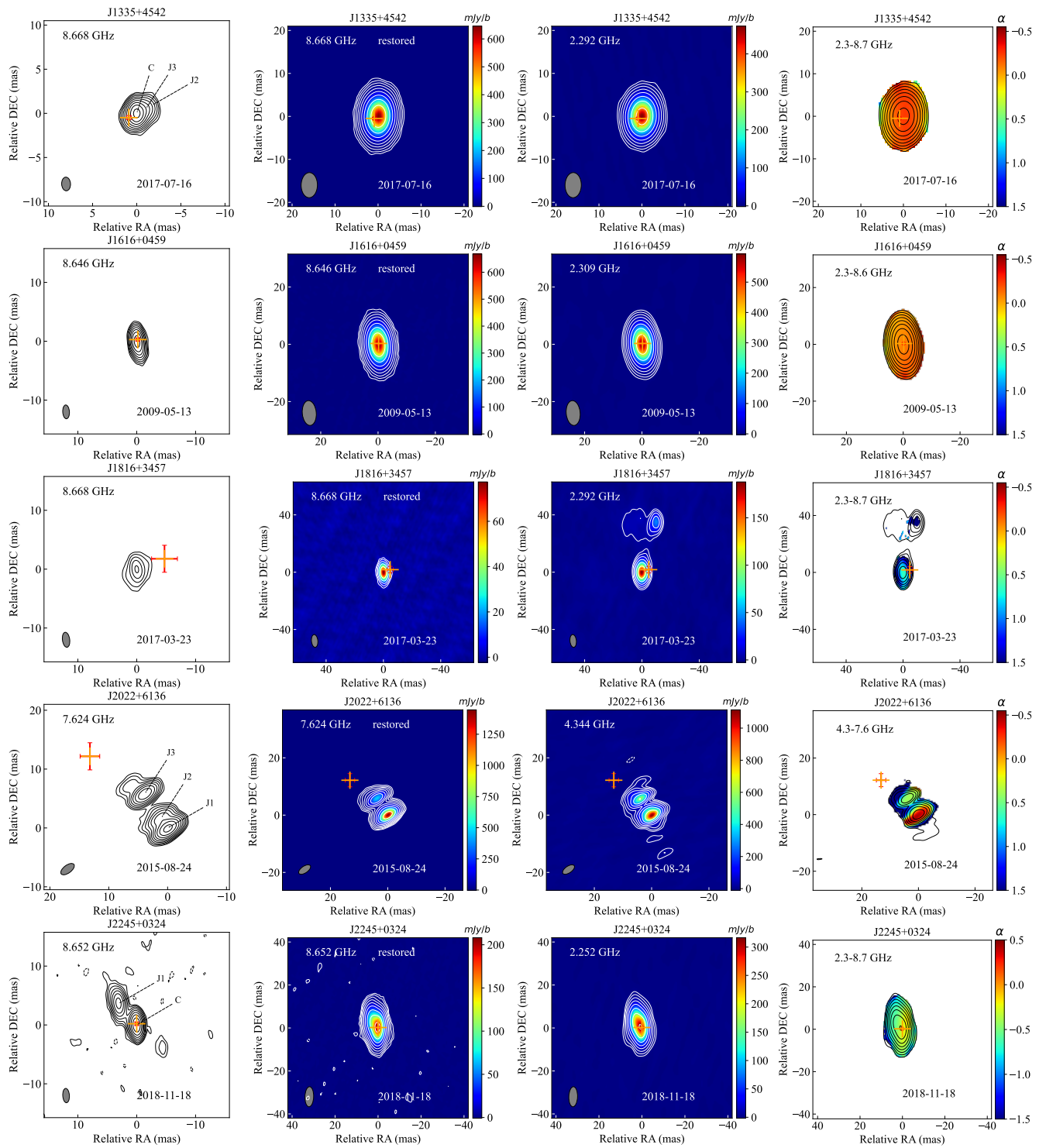


Fig. B.2. Continued.



**Fig. B.3.** VLBI images of confirmed core-jet sources overlaid with their *Gaia* positions located at the presumable jet bases. The red crosses mark the *Gaia* positions and the orange crosses overlaid with caps represent the positional errors of the *Gaia* positions with respect to their VLBI peaks. The spectral index maps are also presented. The *Gaia* position is associated with the brightest component at the end of the jet, which denotes the AGN location.



**Fig. B.3.** Continued.

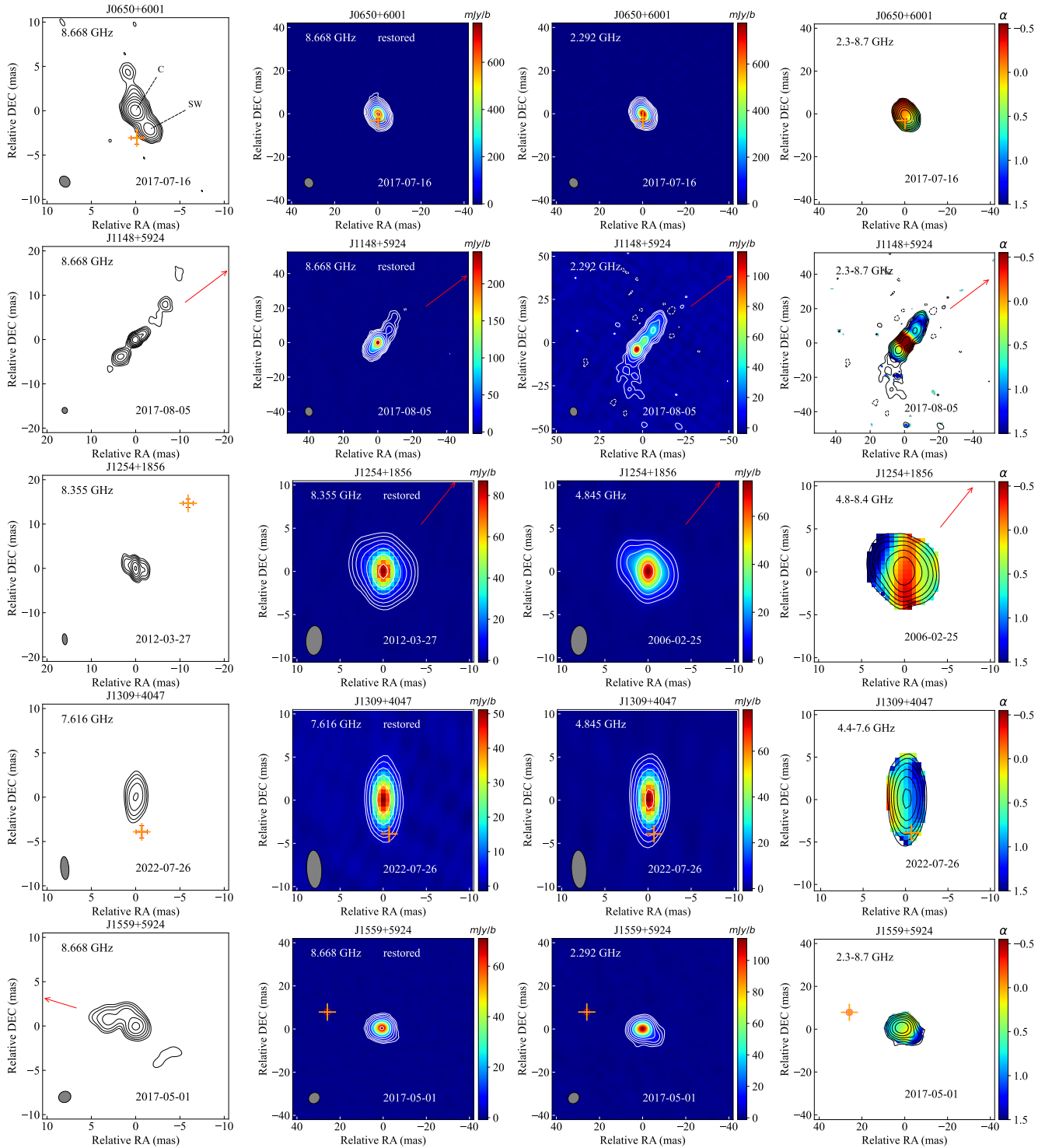


**Fig. B.4.** VLBI images of the 8 remaining candidate CSOs showing a large offset between the peaks of the optical and radio emissions. However, their VLBI images still display the characteristic triple morphology typical of CSOs. For J0119+3210 and J0906+4636, no optically thin components can be found to link the dual-band images, therefore no spectral index maps can be made. For J0831+4608, only one C-band (4.8 GHz) image is available.

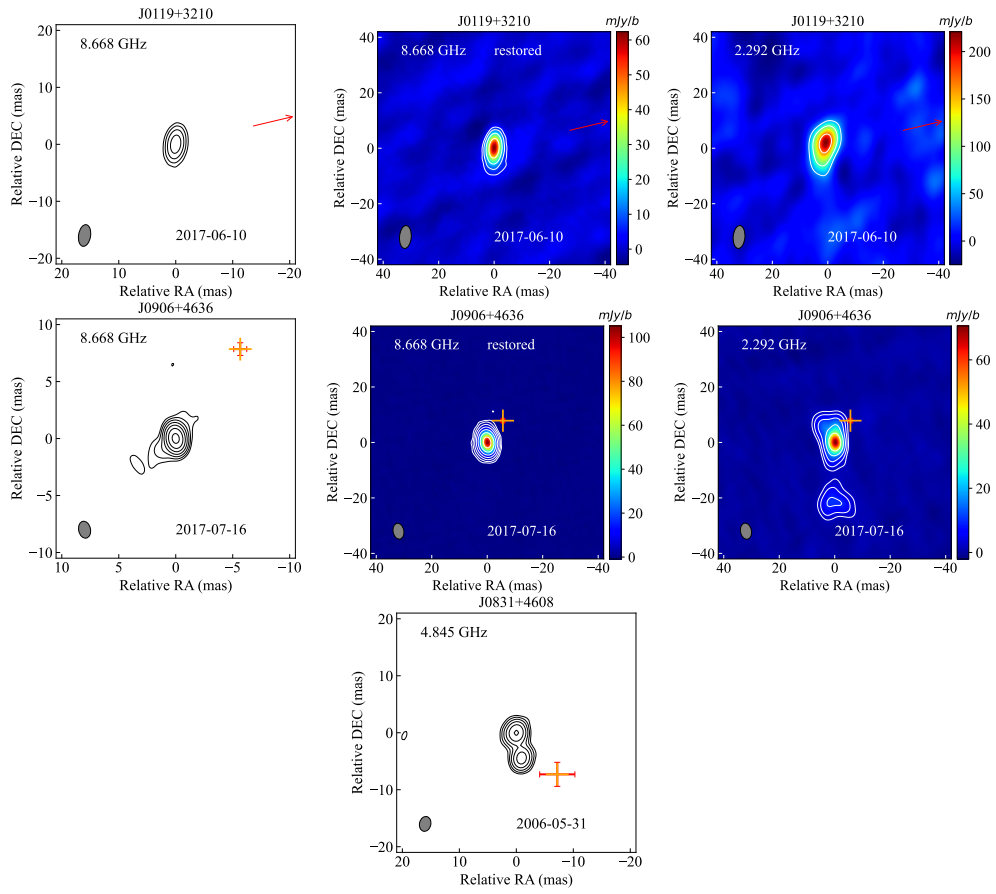


**Fig. B.4.** Continued.

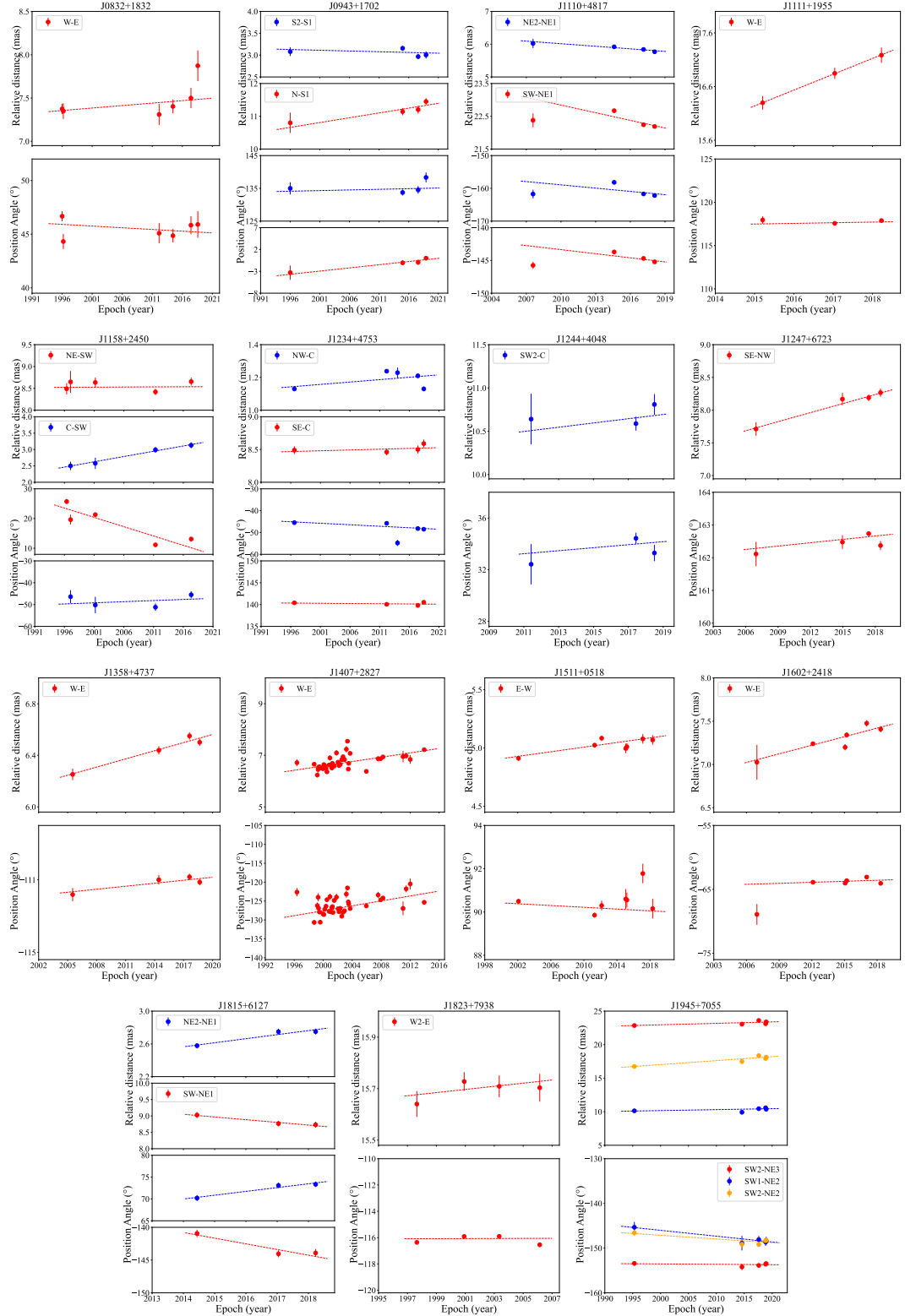


**Fig. B.5.** Proper motion of different components in each confirmed CSO.

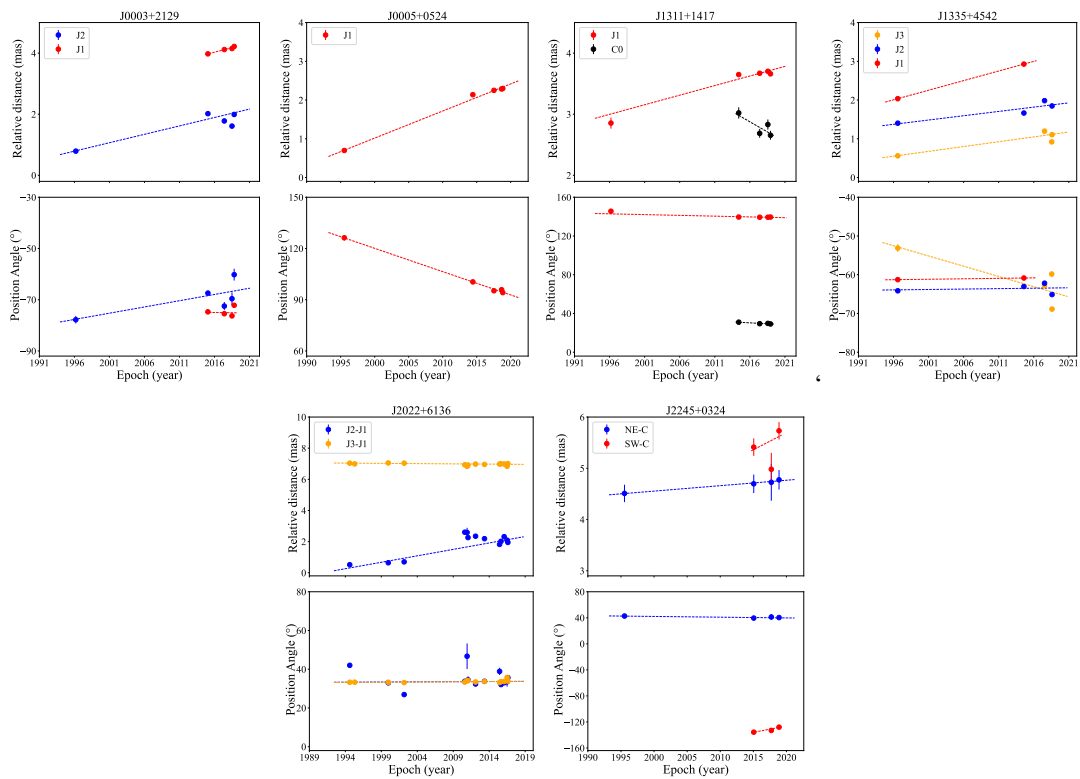


**Fig. B.6.** Proper motion of different components in each core–jet source.

**Table G.1.** Model-fitting parameters of VLBI components for Fig. B.5

Name	Epoch	Label	$S_{\text{int}}$ (mJy)	$R$ (mas)	PA ( $^{\circ}$ )	$\theta_{\text{FWHM}}$ (mas)	$T_b$ (K)
(1)	(2)	(3)	(4)	(5)	(6)	(7)	(8)
J0832+1832	1996/01/02	E	168.6 $\pm$ 8.5	/	/	0.13 $\pm$ 0.01	(2.0 $\pm$ 0.2) $\times$ 10 <sup>11</sup>
		W	86.6 $\pm$ 7.7	7.37 $\pm$ 0.16	46.6 $\pm$ 0.4	2.37 $\pm$ 0.11	(3.1 $\pm$ 0.3) $\times$ 10 <sup>8</sup>
	1996/03/13	E	196.9 $\pm$ 10.1	/	/	0.29 $\pm$ 0.01	(4.7 $\pm$ 0.4) $\times$ 10 <sup>10</sup>
		W	99.9 $\pm$ 12.5	7.35 $\pm$ 0.20	44.2 $\pm$ 0.7	1.83 $\pm$ 0.17	(6.0 $\pm$ 1.1) $\times$ 10 <sup>8</sup>
	2012/02/20	E	140.1 $\pm$ 7.8	/	/	0.46 $\pm$ 0.03	(1.3 $\pm$ 0.2) $\times$ 10 <sup>10</sup>
		W	76.6 $\pm$ 12.0	7.31 $\pm$ 0.24	45.1 $\pm$ 1.0	2.00 $\pm$ 0.25	(3.9 $\pm$ 0.9) $\times$ 10 <sup>8</sup>
	2014/06/09	E	78.7 $\pm$ 4.3	/	/	0.33 $\pm$ 0.03	(1.3 $\pm$ 0.2) $\times$ 10 <sup>10</sup>
		W	36.3 $\pm$ 3.7	7.40 $\pm$ 0.21	44.9 $\pm$ 0.6	2.07 $\pm$ 0.16	(1.6 $\pm$ 0.2) $\times$ 10 <sup>8</sup>
	2017/06/10	E	133.4 $\pm$ 10.1	/	/	0.80 $\pm$ 0.07	(3.9 $\pm$ 0.6) $\times$ 10 <sup>9</sup>
		W	92.5 $\pm$ 14.5	7.50 $\pm$ 0.18	45.8 $\pm$ 0.9	2.24 $\pm$ 0.23	(3.5 $\pm$ 0.7) $\times$ 10 <sup>8</sup>
J0943+1702	1996/01/02	S1	179.6 $\pm$ 9.2	/	/	$\leq$ 0.12	$\geq$ 6.0 $\times$ 10 <sup>11</sup>
		S2	8.2 $\pm$ 1.7	3.08 $\pm$ 0.19	135.1 $\pm$ 1.8	$\leq$ 0.51	$\geq$ 1.4 $\times$ 10 <sup>9</sup>
		N	22.0 $\pm$ 9.4	10.80 $\pm$ 0.23	-3.3 $\pm$ 1.6	2.75 $\pm$ 0.61	(1.3 $\pm$ 0.7) $\times$ 10 <sup>8</sup>
	1996/03/13	S1	203.7 $\pm$ 10.3	/	/	$\leq$ 0.11	$\geq$ 7.2 $\times$ 10 <sup>11</sup>
2014/12/20		S2	8.6 $\pm$ 1.6	3.05 $\pm$ 0.19	132.1 $\pm$ 1.9	$\leq$ 0.54	$\geq$ 1.3 $\times$ 10 <sup>9</sup>
		N	22.4 $\pm$ 3.4	11.44 $\pm$ 0.23	0.0 $\pm$ 0.5	0.91 $\pm$ 0.18	(1.2 $\pm$ 0.4) $\times$ 10 <sup>9</sup>
		S1	158.7 $\pm$ 8.5	/	/	0.28 $\pm$ 0.02	(8.7 $\pm$ 1.1) $\times$ 10 <sup>10</sup>
		S2	13.4 $\pm$ 1.3	3.16 $\pm$ 0.19	133.7 $\pm$ 0.9	0.53 $\pm$ 0.10	(2.0 $\pm$ 0.6) $\times$ 10 <sup>9</sup>
		N	27.2 $\pm$ 4.4	11.14 $\pm$ 0.22	-1.0 $\pm$ 0.6	1.58 $\pm$ 0.22	(4.6 $\pm$ 1.2) $\times$ 10 <sup>8</sup>
2017/08/05		S1	191.7 $\pm$ 10.6	/	/	0.25 $\pm$ 0.03	(1.3 $\pm$ 0.2) $\times$ 10 <sup>11</sup>
		S2	16.9 $\pm$ 1.8	2.97 $\pm$ 0.20	134.6 $\pm$ 1.1	0.66 $\pm$ 0.11	(1.6 $\pm$ 0.4) $\times$ 10 <sup>9</sup>
		N	33.8 $\pm$ 6.1	11.20 $\pm$ 0.23	-0.9 $\pm$ 0.6	1.50 $\pm$ 0.24	(6.3 $\pm$ 1.8) $\times$ 10 <sup>8</sup>
	2018/12/04	S1	173.4 $\pm$ 10.1	/	/	0.31 $\pm$ 0.03	(7.6 $\pm$ 1.1) $\times$ 10 <sup>10</sup>
		S2	15.1 $\pm$ 2.2	3.00 $\pm$ 0.17	138.4 $\pm$ 1.5	0.70 $\pm$ 0.15	(1.3 $\pm$ 0.4) $\times$ 10 <sup>9</sup>
J1110+4817		N	29.8 $\pm$ 5.2	11.44 $\pm$ 0.21	0.0 $\pm$ 0.5	1.26 $\pm$ 0.21	(7.9 $\pm$ 2.3) $\times$ 10 <sup>8</sup>
	2007/08/01	NE1	81.1 $\pm$ 4.2	/	/	$\leq$ 0.32	$\geq$ 2.3 $\times$ 10 <sup>10</sup>
		NE2	14.5 $\pm$ 1.7	6.03 $\pm$ 0.33	-161.8 $\pm$ 1.3	1.15 $\pm$ 0.28	(3.1 $\pm$ 1.1) $\times$ 10 <sup>8</sup>
		SW1	8.3 $\pm$ 1.5	22.38 $\pm$ 0.34	-145.8 $\pm$ 0.5	$\leq$ 1.18	$\geq$ 1.7 $\times$ 10 <sup>8</sup>
	2014/08/09	NE1	44.0 $\pm$ 2.3	/	/	0.36 $\pm$ 0.02	(9.7 $\pm$ 0.9) $\times$ 10 <sup>9</sup>
2017/02/24		NE2	8.8 $\pm$ 0.9	5.93 $\pm$ 0.17	-158.2 $\pm$ 0.6	1.45 $\pm$ 0.12	(1.2 $\pm$ 0.2) $\times$ 10 <sup>8</sup>
		SW1	10.5 $\pm$ 1.0	22.68 $\pm$ 0.16	-143.8 $\pm$ 0.2	1.85 $\pm$ 0.12	(8.7 $\pm$ 1.2) $\times$ 10 <sup>7</sup>
		NE1	47.6 $\pm$ 2.9	/	/	0.39 $\pm$ 0.04	(8.6 $\pm$ 1.2) $\times$ 10 <sup>9</sup>
		NE2	8.3 $\pm$ 0.8	5.85 $\pm$ 0.15	-161.8 $\pm$ 0.4	0.58 $\pm$ 0.09	(6.9 $\pm$ 1.6) $\times$ 10 <sup>8</sup>
		SW1	6.6 $\pm$ 0.5	22.24 $\pm$ 0.15	-144.6 $\pm$ 0.1	1.25 $\pm$ 0.08	(1.2 $\pm$ 0.1) $\times$ 10 <sup>8</sup>
2018/02/09		NE1	39.8 $\pm$ 2.9	/	/	0.68 $\pm$ 0.07	(2.4 $\pm$ 0.4) $\times$ 10 <sup>9</sup>
		NE2	9.0 $\pm$ 0.8	5.78 $\pm$ 0.17	-162.2 $\pm$ 0.5	1.21 $\pm$ 0.10	(1.8 $\pm$ 0.3) $\times$ 10 <sup>8</sup>
		SW1	9.1 $\pm$ 0.7	22.19 $\pm$ 0.16	-145.2 $\pm$ 0.1	0.72 $\pm$ 0.07	(4.9 $\pm$ 0.8) $\times$ 10 <sup>8</sup>
J1111+1955	1996/01/02	W1	148.4 $\pm$ 7.7	/	/	$\leq$ 0.14	$\geq$ 1.9 $\times$ 10 <sup>11</sup>
	1996/03/13	W1	126.0 $\pm$ 7.3	/	/	$\leq$ 0.19	$\geq$ 8.1 $\times$ 10 <sup>10</sup>
	2015/01/22	W1	32.2 $\pm$ 3.0	/	/	$\leq$ 0.43	$\geq$ 3.7 $\times$ 10 <sup>9</sup>
		JX	4.5 $\pm$ 2.3	13.41 $\pm$ 0.27	144.3 $\pm$ 0.9	$\leq$ 0.87	$\geq$ 1.2 $\times$ 10 <sup>8</sup>
	2015/03/17	W1	69.5 $\pm$ 5.1	/	/	$\leq$ 0.38	$\geq$ 1.0 $\times$ 10 <sup>10</sup>
		E1	15.3 $\pm$ 2.8	16.30 $\pm$ 0.21	118.0 $\pm$ 0.4	$\leq$ 0.68	$\geq$ 6.9 $\times$ 10 <sup>8</sup>
	2017/01/16	W1	99.5 $\pm$ 13.2	/	/	1.86 $\pm$ 0.20	(6.0 $\pm$ 1.2) $\times$ 10 <sup>8</sup>
		E1	42.5 $\pm$ 2.9	16.85 $\pm$ 0.14	117.6 $\pm$ 0.1	0.65 $\pm$ 0.06	(2.1 $\pm$ 0.3) $\times$ 10 <sup>9</sup>
2018/03/26		W1	124.0 $\pm$ 21.5	/	/	2.06 $\pm$ 0.27	(6.1 $\pm$ 1.5) $\times$ 10 <sup>8</sup>
		E1	52.9 $\pm$ 5.6	17.19 $\pm$ 0.17	117.9 $\pm$ 0.2	0.84 $\pm$ 0.13	(1.6 $\pm$ 0.4) $\times$ 10 <sup>9</sup>

Note that we have avoided here the archival VLBI data of some epochs of bad quality in terms of signal-to-noise ratio and astrometric positions. Also, the relative positions of the components in J0832+1832 and J1358+4737 are given with respect to their brightest component position. The components are marked in order of either East to West or North to South direction.

**Table G.1.** Continued.

Name	Epoch	Label	$S_{\text{int}}$ (mJy)	R (mas)	PA (°)	$\theta_{\text{FWHM}}$ (mas)	$T_b$ (K)
(1)	(2)	(3)	(4)	(5)	(6)	(7)	(8)
J1158+2450	1996/05/15	SW1	116.2±6.1	/	/	0.24±0.02	(4.3±0.5)×10 <sup>10</sup>
		NE1	24.0±4.5	8.49±0.21	25.8±0.9	0.96±0.25	(5.5±2.3)×10 <sup>8</sup>
	1997/01/10	SW1	107.3±5.6	/	/	0.37±0.02	(1.6±0.1)×10 <sup>10</sup>
		C1	29.4±5.4	2.51±0.16	-46.4±2.9	2.20±0.26	(1.3±0.3)×10 <sup>8</sup>
		NE1	23.7±7.8	8.65±0.19	19.7±1.6	2.74±0.49	(6.7±2.8)×10 <sup>7</sup>
	2001/03/12	SW1	82.0±4.8	/	/	≤0.22	≥3.2×10 <sup>10</sup>
		C1	13.3±4.0	2.58±0.19	-50.3±3.8	≤0.75	≥4.6×10 <sup>8</sup>
		NE1	17.3±3.3	8.64±0.24	21.2±0.8	≤0.60	≥9.5×10 <sup>8</sup>
	2011/04/26	SW1	302.6±16.1	/	/	0.40±0.02	(3.9±0.3)×10 <sup>10</sup>
		C1	103.6±14.6	2.99±0.17	-51.2±1.8	2.54±0.19	(3.4±0.6)×10 <sup>8</sup>
		NE1	85.0±9.3	8.42±0.22	11.1±0.5	3.39±0.14	(1.5±0.2)×10 <sup>8</sup>
J1234+4753	2017/05/01	SW1	324.8±16.6	/	/	0.52±0.01	(2.3±0.1)×10 <sup>10</sup>
		C1	80.7±11.1	3.13±0.16	-45.5±1.7	2.51±0.18	(2.5±0.4)×10 <sup>8</sup>
		NE1	72.2±9.5	8.66±0.19	13.1±0.6	3.25±0.17	(1.3±0.2)×10 <sup>8</sup>
	1996/08/10	C	124.0±6.2	/	/	0.08±0.00	(4.8±0.4)×10 <sup>11</sup>
		NW1	17.4±1.0	1.13±0.16	-45.5±0.6	0.37±0.02	(3.0±0.3)×10 <sup>9</sup>
		SE1	8.1±1.0	8.49±0.17	140.3±0.4	0.59±0.11	(5.6±1.7)×10 <sup>8</sup>
	2012/03/07	C	232.5±11.7	/	/	0.34±0.01	(4.9±0.3)×10 <sup>10</sup>
		NW1	39.4±2.1	1.23±0.14	-45.9±0.5	0.48±0.02	(4.0±0.3)×10 <sup>9</sup>
		SE1	6.9±0.6	8.47±0.15	140.1±0.3	0.56±0.09	(5.3±1.3)×10 <sup>8</sup>
	2014/01/04	C	172.3±8.9	/	/	0.24±0.01	(6.6±0.6)×10 <sup>10</sup>
		NW1	19.6±1.9	1.23±0.11	-54.8±1.5	≤0.27	≥6.1×10 <sup>9</sup>
		NE1	184.0±9.5	/	/	0.30±0.01	(4.5±0.3)×10 <sup>10</sup>
J1244+4048	2017/06/10	NW1	36.1±2.1	1.21±0.13	-48.2±0.5	0.26±0.02	(1.2±0.1)×10 <sup>10</sup>
		SE1	7.5±1.0	8.50±0.14	139.8±0.4	0.75±0.12	(3.0±0.8)×10 <sup>8</sup>
		C	146.4±7.5	/	/	0.30±0.01	(3.5±0.2)×10 <sup>10</sup>
	2018/06/09	NW1	18.6±1.2	1.13±0.13	-48.5±0.7	0.31±0.03	(4.3±0.6)×10 <sup>9</sup>
		SE1	5.9±0.7	8.59±0.13	140.5±0.4	0.66±0.11	(3.0±0.8)×10 <sup>8</sup>
		NE1	30.9±2.5	/	/	≤0.35	≥7.9×10 <sup>9</sup>
	2011/06/03	SW2	20.2±6.7	10.65±0.29	32.4±1.5	3.17±0.57	(6.3±2.7)×10 <sup>7</sup>
		NE1	57.4±3.1	/	/	≤0.15	≥7.2×10 <sup>10</sup>
		NE2	36.4±2.2	1.80±0.14	-141.3±0.5	0.30±0.03	(1.2±0.2)×10 <sup>10</sup>
J1247+6723	2018/07/01	SW1	44.6±6.1	10.59±0.15	34.4±0.5	3.89±0.17	(8.7±1.3)×10 <sup>7</sup>
		SW2	40.8±14.4	10.76±0.15	-153.9±1.2	3.64±0.47	(9.1±3.6)×10 <sup>7</sup>
		SW3	40.4±5.1	18.70±0.15	-152.6±0.2	3.27±0.15	(1.1±0.2)×10 <sup>8</sup>
		NE1	81.9±4.4	/	/	≤0.14	≥1.2×10 <sup>11</sup>
		NE2	25.9±2.1	1.98±0.15	-143.0±0.8	≤0.26	≥1.2×10 <sup>10</sup>
	2006/12/18	SW1	14.2±3.0	9.66±0.16	-155.8±0.6	≤0.49	≥1.7×10 <sup>9</sup>
		SW2	29.9±5.8	10.81±0.15	33.2±0.6	2.74±0.24	(1.2±0.3)×10 <sup>8</sup>
		SW3	54.4±21.6	17.67±0.16	-153.4±0.8	5.85±0.51	(4.7±2.0)×10 <sup>7</sup>
		NW	53.0±7.8	/	/	≤0.55	≥3.2×10 <sup>9</sup>
		SE	24.8±2.3	7.71±0.21	162.1±1.6	≤0.40	≥2.9×10 <sup>9</sup>
J1256+5652	2014/12/20	NW	49.7±8.2	/	/	0.59±0.00	(2.6±0.4)×10 <sup>9</sup>
		SE	32.9±2.5	8.17±0.12	162.5±0.8	0.58±0.30	(1.7±1.3)×10 <sup>9</sup>
		NW	68.2±7.0	/	/	0.71±0.00	(2.5±0.3)×10 <sup>9</sup>
		SE	48.8±2.8	8.19±0.14	162.7±1.0	0.68±0.30	(1.9±1.2)×10 <sup>9</sup>
		NW	57.0±7.0	/	/	0.78±0.00	(1.7±0.2)×10 <sup>9</sup>
	1999/03/08	SE	42.7±2.5	8.27±0.13	162.4±0.9	0.65±0.29	(1.8±1.1)×10 <sup>9</sup>
		C	118.4±6.9	/	/	≤0.20	≥5.6×10 <sup>10</sup>
		E1	27.7±2.2	1.01±0.18	52.5±1.2	≤0.23	≥9.4×10 <sup>9</sup>
		C	52.4±2.6	/	/	0.13±0.00	(5.0±0.3)×10 <sup>10</sup>
		W1	39.5±2.0	0.26±0.09	-93.8±0.3	0.20±0.00	(1.7±0.1)×10 <sup>10</sup>
		E1	46.3±2.3	1.02±0.08	66.0±0.1	0.10±0.00	(7.4±0.6)×10 <sup>10</sup>

**Table G.1.** Continued.

Name	Epoch	Label	$S_{\text{int}}$ (mJy)	R (mas)	PA (°)	$\theta_{\text{FWHM}}$ (mas)	$T_b$ (K)
(1)	(2)	(3)	(4)	(5)	(6)	(7)	(8)
J1358+4737	2014/06/09	C	93.8±4.7	/	/	0.22±0.00	(3.3±0.2)×10 <sup>10</sup>
		W1	18.8±1.0	0.48±0.14	-115.1±0.3	0.24±0.01	(5.7±0.4)×10 <sup>9</sup>
		E1	41.4±2.1	0.91±0.14	65.3±0.3	0.45±0.01	(3.4±0.2)×10 <sup>9</sup>
	2017/01/21	C	56.6±2.9	/	/	0.10±0.00	(10.0±0.6)×10 <sup>10</sup>
		W1	87.7±4.4	0.27±0.10	-90.1±0.4	0.27±0.00	(2.0±0.1)×10 <sup>10</sup>
		E1	105.3±5.3	0.86±0.11	57.1±0.1	0.19±0.00	(5.1±0.3)×10 <sup>10</sup>
	2018/12/04	C	242.7±12.2	/	/	0.29±0.00	(4.8±0.2)×10 <sup>10</sup>
		W1	42.9±2.3	0.33±0.12	-112.1±0.4	≤0.07	≥1.4×10 <sup>11</sup>
		E1	120.5±6.2	0.93±0.12	64.2±0.2	0.30±0.01	(2.3±0.1)×10 <sup>10</sup>
J1407+2827	2005/07/09	E	116.3±7.3	/	/	0.74±0.05	(4.2±0.4)×10 <sup>9</sup>
		W	42.1±3.6	6.25±0.13	-111.8±0.3	0.39±0.08	(5.6±1.6)×10 <sup>9</sup>
		E	161.7±9.1	/	/	0.68±0.03	(7.0±0.6)×10 <sup>9</sup>
	2014/06/09	W	42.1±3.1	6.44±0.13	-111.0±0.2	0.46±0.05	(4.0±0.7)×10 <sup>9</sup>
		E	220.7±14.9	/	/	0.62±0.05	(1.1±0.1)×10 <sup>10</sup>
		W	47.2±3.2	6.55±0.11	-110.9±0.2	0.69±0.05	(2.0±0.2)×10 <sup>9</sup>
	2017/08/12	E	219.8±14.6	/	/	0.64±0.04	(1.1±0.1)×10 <sup>10</sup>
		W	49.5±3.2	6.50±0.12	-111.2±0.2	0.55±0.04	(3.3±0.4)×10 <sup>9</sup>
		C	1166.3±59.1	/	/	0.38±0.01	(1.5±0.1)×10 <sup>11</sup>
	1998/10/01	JX	278.5±15.1	1.20±0.22	-19.8±0.3	0.58±0.01	(1.6±0.1)×10 <sup>10</sup>
		J1	118.5±23.4	6.71±0.14	-122.6±1.2	1.80±0.27	(7.0±2.0)×10 <sup>8</sup>
		C	644.1±34.4	/	/	0.23±0.01	(2.2±0.2)×10 <sup>11</sup>
1999/03/08	1999/04/15	JX	517.4±28.0	0.35±0.21	-38.3±1.2	0.80±0.01	(1.4±0.1)×10 <sup>10</sup>
		J1	80.1±10.3	6.65±0.12	-130.6±0.6	0.96±0.13	(1.5±0.4)×10 <sup>9</sup>
		C	917.5±52.3	/	/	0.47±0.02	(7.4±0.6)×10 <sup>10</sup>
	1999/05/10	JX	252.2±15.7	1.00±0.12	-27.4±0.7	0.82±0.02	(6.7±0.5)×10 <sup>9</sup>
		J1	87.6±17.7	6.23±0.08	-126.2±0.8	1.38±0.17	(8.2±2.2)×10 <sup>8</sup>
		C	1134.0±62.4	/	/	0.47±0.02	(9.1±0.7)×10 <sup>10</sup>
	1999/06/21	JX	226.6±15.2	1.06±0.13	-24.3±0.8	0.77±0.03	(6.8±0.6)×10 <sup>9</sup>
		J1	115.9±28.2	6.45±0.08	-124.0±1.0	1.85±0.24	(6.0±1.8)×10 <sup>8</sup>
		C	1138.4±64.6	/	/	0.48±0.02	(8.8±0.7)×10 <sup>10</sup>
2000/01/31	1999/08/02	JX	297.7±18.2	1.05±0.11	-25.6±0.6	0.87±0.02	(7.0±0.5)×10 <sup>9</sup>
		J1	109.9±9.7	6.53±0.09	-126.9±0.3	1.01±0.06	(1.9±0.2)×10 <sup>9</sup>
		C	1220.1±63.3	/	/	0.50±0.01	(8.7±0.6)×10 <sup>10</sup>
	2000/03/13	JX	192.7±10.4	1.19±0.17	-21.7±0.3	0.57±0.01	(1.1±0.1)×10 <sup>10</sup>
		J1	103.0±9.6	6.56±0.15	-127.9±0.4	1.01±0.10	(1.8±0.3)×10 <sup>9</sup>
		C	1140.7±62.5	/	/	0.44±0.02	(1.0±0.1)×10 <sup>11</sup>
	2000/05/22	JX	220.3±14.0	1.05±0.14	-30.2±0.6	0.73±0.02	(7.3±0.6)×10 <sup>9</sup>
		J1	85.5±12.2	6.51±0.09	-130.6±0.5	1.13±0.12	(1.2±0.2)×10 <sup>9</sup>
		C	1038.7±58.5	/	/	0.49±0.02	(7.7±0.6)×10 <sup>10</sup>
2000/07/06	2000/12/20	JX	245.7±14.2	1.04±0.12	-27.4±0.5	0.77±0.02	(7.4±0.5)×10 <sup>9</sup>
		J1	95.1±8.8	6.48±0.09	-128.4±0.3	0.85±0.07	(2.3±0.3)×10 <sup>9</sup>
		C	1081.6±63.0	/	/	0.46±0.02	(9.1±0.8)×10 <sup>10</sup>
	2000/03/13	JX	231.2±17.8	1.02±0.10	-26.3±1.0	0.68±0.04	(8.9±1.0)×10 <sup>9</sup>
		J1	87.1±9.6	6.64±0.08	-128.6±0.3	0.71±0.07	(3.1±0.5)×10 <sup>9</sup>
		C	1180.5±66.7	/	/	0.47±0.02	(9.5±0.7)×10 <sup>10</sup>
	2000/05/22	JX	317.3±20.2	0.94±0.11	-29.6±0.7	0.80±0.02	(8.8±0.7)×10 <sup>9</sup>
		J1	103.8±12.9	6.60±0.08	-127.2±0.4	0.95±0.09	(2.0±0.4)×10 <sup>9</sup>
		C	1117.4±65.6	/	/	0.47±0.02	(9.0±0.8)×10 <sup>10</sup>
	2000/07/06	JX	243.9±18.2	1.04±0.11	-28.3±0.9	0.61±0.03	(1.2±0.1)×10 <sup>10</sup>
		J1	98.6±15.6	6.49±0.07	-126.4±0.5	0.97±0.11	(1.9±0.4)×10 <sup>9</sup>
		C	1097.7±62.1	/	/	0.47±0.02	(8.8±0.8)×10 <sup>10</sup>
		JX	215.3±13.6	1.04±0.15	-26.9±0.5	0.73±0.02	(7.2±0.5)×10 <sup>9</sup>
		J1	102.7±12.3	6.36±0.10	-124.6±0.5	1.00±0.11	(1.8±0.4)×10 <sup>9</sup>

**Table G.1.** Continued.

Name (1)	Epoch (2)	Label (3)	$S_{\text{int}}$ (mJy) (4)	$R$ (mas) (5)	PA ( $^{\circ}$ ) (6)	$\theta_{\text{FWHM}}$ (mas) (7)	$T_b$ (K) (8)
2000/10/23	C	1192.6 $\pm$ 68.8	/	/	0.49 $\pm$ 0.02	(8.8 $\pm$ 0.7) $\times$ 10 <sup>10</sup>	
	JX	222.5 $\pm$ 14.3	1.03 $\pm$ 0.12	-28.2 $\pm$ 0.6	0.63 $\pm$ 0.02	(10.0 $\pm$ 0.8) $\times$ 10 <sup>9</sup>	
	J1	75.4 $\pm$ 10.5	6.62 $\pm$ 0.08	-127.7 $\pm$ 0.4	0.62 $\pm$ 0.10	(3.5 $\pm$ 0.9) $\times$ 10 <sup>9</sup>	
2000/12/04	C	944.2 $\pm$ 58.4	/	/	0.43 $\pm$ 0.03	(9.1 $\pm$ 1.0) $\times$ 10 <sup>10</sup>	
	JX	382.1 $\pm$ 22.6	0.86 $\pm$ 0.13	-29.0 $\pm$ 0.7	0.84 $\pm$ 0.02	(9.6 $\pm$ 0.7) $\times$ 10 <sup>9</sup>	
	J1	132.8 $\pm$ 30.2	6.90 $\pm$ 0.09	-123.9 $\pm$ 0.9	1.36 $\pm$ 0.21	(1.3 $\pm$ 0.4) $\times$ 10 <sup>9</sup>	
2001/01/29	C	917.1 $\pm$ 53.1	/	/	0.42 $\pm$ 0.02	(9.2 $\pm$ 0.8) $\times$ 10 <sup>10</sup>	
	JX	242.1 $\pm$ 15.4	0.86 $\pm$ 0.12	-30.3 $\pm$ 0.7	0.82 $\pm$ 0.02	(6.4 $\pm$ 0.5) $\times$ 10 <sup>9</sup>	
	J1	68.1 $\pm$ 10.2	6.64 $\pm$ 0.08	-127.9 $\pm$ 0.5	0.50 $\pm$ 0.11	(4.8 $\pm$ 1.7) $\times$ 10 <sup>9</sup>	
2001/03/12	C	1072.7 $\pm$ 61.6	/	/	0.42 $\pm$ 0.02	(1.1 $\pm$ 0.1) $\times$ 10 <sup>11</sup>	
	JX	451.9 $\pm$ 26.1	0.76 $\pm$ 0.16	-30.4 $\pm$ 0.7	0.87 $\pm$ 0.02	(1.1 $\pm$ 0.1) $\times$ 10 <sup>10</sup>	
	J1	111.1 $\pm$ 10.8	6.51 $\pm$ 0.11	-126.8 $\pm$ 0.4	0.81 $\pm$ 0.08	(3.0 $\pm$ 0.5) $\times$ 10 <sup>9</sup>	
2001/04/09	C	1049.3 $\pm$ 62.3	/	/	0.46 $\pm$ 0.02	(8.8 $\pm$ 0.8) $\times$ 10 <sup>10</sup>	
	JX	308.9 $\pm$ 19.9	0.88 $\pm$ 0.11	-31.0 $\pm$ 0.7	0.86 $\pm$ 0.02	(7.4 $\pm$ 0.6) $\times$ 10 <sup>9</sup>	
	J1	104.6 $\pm$ 9.7	6.69 $\pm$ 0.09	-126.5 $\pm$ 0.3	0.72 $\pm$ 0.06	(3.6 $\pm$ 0.6) $\times$ 10 <sup>9</sup>	
2001/05/09	C	1031.5 $\pm$ 59.1	/	/	0.38 $\pm$ 0.02	(1.3 $\pm$ 0.1) $\times$ 10 <sup>11</sup>	
	JX	554.9 $\pm$ 37.6	0.31 $\pm$ 0.10	-78.7 $\pm$ 2.4	1.60 $\pm$ 0.03	(3.8 $\pm$ 0.3) $\times$ 10 <sup>9</sup>	
	J1	109.5 $\pm$ 11.5	6.62 $\pm$ 0.09	-128.0 $\pm$ 0.4	0.63 $\pm$ 0.08	(4.9 $\pm$ 1.0) $\times$ 10 <sup>9</sup>	
2001/07/05	C	1155.9 $\pm$ 68.3	/	/	0.46 $\pm$ 0.02	(9.7 $\pm$ 0.9) $\times$ 10 <sup>10</sup>	
	JX	327.2 $\pm$ 20.2	0.88 $\pm$ 0.12	-31.5 $\pm$ 0.7	0.86 $\pm$ 0.02	(7.9 $\pm$ 0.6) $\times$ 10 <sup>9</sup>	
	J1	133.6 $\pm$ 19.4	6.58 $\pm$ 0.10	-124.8 $\pm$ 0.6	1.24 $\pm$ 0.13	(1.5 $\pm$ 0.3) $\times$ 10 <sup>9</sup>	
2001/10/29	C	770.6 $\pm$ 47.9	/	/	0.28 $\pm$ 0.02	(1.7 $\pm$ 0.2) $\times$ 10 <sup>11</sup>	
	JX	797.5 $\pm$ 48.5	0.35 $\pm$ 0.12	-48.2 $\pm$ 1.8	1.10 $\pm$ 0.02	(1.2 $\pm$ 0.1) $\times$ 10 <sup>10</sup>	
	J1	137.0 $\pm$ 31.1	7.09 $\pm$ 0.08	-124.0 $\pm$ 0.8	1.42 $\pm$ 0.20	(1.2 $\pm$ 0.4) $\times$ 10 <sup>9</sup>	
2002/01/16	C	910.7 $\pm$ 54.5	/	/	0.37 $\pm$ 0.02	(1.2 $\pm$ 0.1) $\times$ 10 <sup>11</sup>	
	JX	616.5 $\pm$ 39.8	0.49 $\pm$ 0.10	-43.6 $\pm$ 1.5	0.84 $\pm$ 0.03	(1.6 $\pm$ 0.1) $\times$ 10 <sup>10</sup>	
	J1	86.7 $\pm$ 9.2	6.73 $\pm$ 0.08	-127.0 $\pm$ 0.3	0.49 $\pm$ 0.07	(6.4 $\pm$ 1.4) $\times$ 10 <sup>9</sup>	
2002/03/06	C	1013.0 $\pm$ 60.1	/	/	0.38 $\pm$ 0.02	(1.2 $\pm$ 0.1) $\times$ 10 <sup>11</sup>	
	JX	643.6 $\pm$ 46.1	0.33 $\pm$ 0.09	-78.0 $\pm$ 3.3	1.68 $\pm$ 0.04	(4.0 $\pm$ 0.3) $\times$ 10 <sup>9</sup>	
	J1	110.0 $\pm$ 8.3	6.60 $\pm$ 0.10	-127.8 $\pm$ 0.2	0.67 $\pm$ 0.05	(4.4 $\pm$ 0.6) $\times$ 10 <sup>9</sup>	
2002/05/08	C	859.9 $\pm$ 55.6	/	/	0.35 $\pm$ 0.03	(1.2 $\pm$ 0.2) $\times$ 10 <sup>11</sup>	
	JX	765.6 $\pm$ 51.7	0.36 $\pm$ 0.11	-52.6 $\pm$ 2.6	1.25 $\pm$ 0.03	(8.7 $\pm$ 0.7) $\times$ 10 <sup>9</sup>	
	J1	130.2 $\pm$ 13.4	6.65 $\pm$ 0.11	-126.9 $\pm$ 0.4	1.01 $\pm$ 0.09	(2.3 $\pm$ 0.4) $\times$ 10 <sup>9</sup>	
2002/07/24	C	1208.1 $\pm$ 71.0	/	/	0.55 $\pm$ 0.03	(7.1 $\pm$ 0.6) $\times$ 10 <sup>10</sup>	
	JX	282.5 $\pm$ 19.9	0.85 $\pm$ 0.13	-23.4 $\pm$ 1.0	0.73 $\pm$ 0.03	(9.4 $\pm$ 0.9) $\times$ 10 <sup>9</sup>	
	J1	119.4 $\pm$ 14.4	6.83 $\pm$ 0.10	-129.0 $\pm$ 0.4	1.11 $\pm$ 0.11	(1.7 $\pm$ 0.3) $\times$ 10 <sup>9</sup>	
2002/09/25	C	1199.0 $\pm$ 67.8	/	/	0.50 $\pm$ 0.02	(8.5 $\pm$ 0.7) $\times$ 10 <sup>10</sup>	
	JX	455.9 $\pm$ 37.0	0.60 $\pm$ 0.08	-96.3 $\pm$ 2.5	1.71 $\pm$ 0.05	(2.8 $\pm$ 0.3) $\times$ 10 <sup>9</sup>	
	J1	98.4 $\pm$ 13.7	6.94 $\pm$ 0.11	-128.0 $\pm$ 0.5	0.57 $\pm$ 0.11	(5.4 $\pm$ 1.7) $\times$ 10 <sup>9</sup>	
2002/12/11	C	699.7 $\pm$ 46.7	/	/	0.30 $\pm$ 0.02	(1.4 $\pm$ 0.2) $\times$ 10 <sup>11</sup>	
	JX	805.7 $\pm$ 54.9	0.30 $\pm$ 0.08	-80.9 $\pm$ 2.8	1.20 $\pm$ 0.03	(9.9 $\pm$ 0.8) $\times$ 10 <sup>9</sup>	
	J1	94.6 $\pm$ 10.1	6.83 $\pm$ 0.08	-127.6 $\pm$ 0.3	0.59 $\pm$ 0.07	(4.8 $\pm$ 1.0) $\times$ 10 <sup>9</sup>	
2003/03/12	C	1054.5 $\pm$ 63.8	/	/	0.50 $\pm$ 0.03	(7.5 $\pm$ 0.7) $\times$ 10 <sup>10</sup>	
	JX	641.7 $\pm$ 46.9	0.44 $\pm$ 0.08	-89.7 $\pm$ 2.7	2.06 $\pm$ 0.04	(2.7 $\pm$ 0.2) $\times$ 10 <sup>9</sup>	
	J1	131.6 $\pm$ 31.6	7.23 $\pm$ 0.10	-123.2 $\pm$ 1.0	1.52 $\pm$ 0.25	(1.0 $\pm$ 0.3) $\times$ 10 <sup>9</sup>	
2003/05/07	C	1070.6 $\pm$ 56.9	/	/	0.65 $\pm$ 0.02	(4.5 $\pm$ 0.3) $\times$ 10 <sup>10</sup>	
	JX	62.2 $\pm$ 15.6	2.11 $\pm$ 0.11	-115.8 $\pm$ 2.2	$\leq$ 0.40	$\geq$ 6.9 $\times$ 10 <sup>9</sup>	
	J1	62.1 $\pm$ 10.2	7.55 $\pm$ 0.12	-121.5 $\pm$ 0.5	$\leq$ 0.34	$\geq$ 9.7 $\times$ 10 <sup>9</sup>	
2003/06/18	C	958.3 $\pm$ 49.3	/	/	0.41 $\pm$ 0.01	(1.0 $\pm$ 0.1) $\times$ 10 <sup>11</sup>	
	JX	154.4 $\pm$ 8.9	0.83 $\pm$ 0.15	-41.5 $\pm$ 0.5	0.44 $\pm$ 0.01	(1.4 $\pm$ 0.1) $\times$ 10 <sup>10</sup>	
	J1	80.6 $\pm$ 9.6	6.46 $\pm$ 0.13	-125.2 $\pm$ 0.5	0.50 $\pm$ 0.11	(5.7 $\pm$ 1.9) $\times$ 10 <sup>9</sup>	
2003/07/09	C	1229.1 $\pm$ 72.2	/	/	0.55 $\pm$ 0.02	(7.2 $\pm$ 0.6) $\times$ 10 <sup>10</sup>	
	JX	288.4 $\pm$ 18.3	0.95 $\pm$ 0.12	-18.7 $\pm$ 0.8	0.90 $\pm$ 0.03	(6.3 $\pm$ 0.5) $\times$ 10 <sup>9</sup>	
	J1	120.3 $\pm$ 9.9	6.69 $\pm$ 0.10	-125.8 $\pm$ 0.3	1.06 $\pm$ 0.06	(1.9 $\pm$ 0.2) $\times$ 10 <sup>9</sup>	

**Table G.1.** Continued.

Name	Epoch	Label	$S_{\text{int}}$ (mJy)	R (mas)	PA (°)	$\theta_{\text{FWHM}}$ (mas)	$T_b$ (K)
(1)	(2)	(3)	(4)	(5)	(6)	(7)	(8)
2003/09/17	C	756.7±51.8	/	/	0.36±0.03	(1.0±0.1)×10 <sup>11</sup>	
	JX	689.6±45.4	0.40±0.09	-44.5±1.8	1.12±0.02	(9.8±0.7)×10 <sup>9</sup>	
	J1	84.5±13.0	7.08±0.08	-127.0±0.4	0.34±0.09	(1.3±0.5)×10 <sup>10</sup>	
	C	1217.1±74.4	/	/	0.79±0.03	(3.5±0.3)×10 <sup>10</sup>	
	JX	105.8±17.3	1.17±0.12	-24.9±1.8	≤0.26	≥2.8×10 <sup>10</sup>	
	J1	110.9±13.4	6.38±0.10	-126.3±0.4	0.88±0.10	(2.5±0.5)×10 <sup>9</sup>	
2005/12/14	C	1682.6±86.5	/	/	0.80±0.02	(4.7±0.3)×10 <sup>10</sup>	
	JX	22.3±8.7	2.14±0.34	-9.6±0.5	≤0.27	≥5.4×10 <sup>9</sup>	
	J1	160.7±19.4	6.87±0.18	-123.4±0.9	1.65±0.21	(1.0±0.2)×10 <sup>9</sup>	
2007/08/01	C	1094.6±81.0	/	/	0.93±0.04	(2.2±0.2)×10 <sup>10</sup>	
	JX	71.7±22.0	1.79±0.09	-18.8±2.6	≤0.36	≥1.0×10 <sup>10</sup>	
	J1	90.4±10.2	6.87±0.07	-124.7±0.3	1.06±0.08	(1.4±0.2)×10 <sup>9</sup>	
2007/12/05	C	1016.8±63.5	/	/	0.77±0.04	(3.0±0.3)×10 <sup>10</sup>	
	JX	181.2±19.9	1.09±0.13	-13.9±1.8	0.46±0.07	(1.5±0.4)×10 <sup>10</sup>	
	J1	122.0±13.1	6.94±0.18	-124.2±0.5	1.36±0.13	(1.2±0.2)×10 <sup>9</sup>	
2011/01/09	C	587.6±40.0	/	/	≤0.30	≥1.2×10 <sup>11</sup>	
	JX	250.8±23.5	0.37±0.24	11.7±4.1	2.17±0.05	(9.5±0.9)×10 <sup>8</sup>	
	J1	33.7±13.0	6.95±0.18	-126.9±1.9	≤0.91	≥7.2×10 <sup>8</sup>	
2011/06/14	C	1011.9±56.0	/	/	0.82±0.03	(2.8±0.2)×10 <sup>10</sup>	
	JX	174.8±11.9	1.68±0.22	-8.1±0.6	0.84±0.03	(4.6±0.4)×10 <sup>9</sup>	
	J1	145.7±24.2	6.98±0.14	-121.8±0.9	1.92±0.22	(7.4±1.7)×10 <sup>8</sup>	
2012/01/08	C	754.3±40.3	/	/	0.53±0.02	(5.0±0.4)×10 <sup>10</sup>	
	JX	413.9±23.4	1.16±0.22	-3.2±0.6	1.37±0.03	(4.1±0.3)×10 <sup>9</sup>	
	J1	150.3±35.2	6.84±0.18	-120.5±1.4	2.02±0.33	(6.9±2.3)×10 <sup>8</sup>	
2013/12/11	C	396.1±20.3	/	/	0.41±0.01	(4.2±0.3)×10 <sup>10</sup>	
	JX	256.6±13.4	0.84±0.13	-146.8±0.4	0.13±0.01	(2.7±0.4)×10 <sup>11</sup>	
	JX	132.6±8.1	0.84±0.13	-146.8±1.0	0.64±0.03	(5.7±0.5)×10 <sup>9</sup>	
J1511+0518	J1	30.2±5.4	7.22±0.13	-125.3±0.6	≤0.40	≥3.3×10 <sup>9</sup>	
	2002/01/31	W	218.2±13.5	/	/	0.42±0.00	(2.2±0.1)×10 <sup>10</sup>
	E	168.0±8.9	4.91±0.11	90.5±1.3	≤0.17	≥1.0×10 <sup>11</sup>	
	2011/04/19	W	548.7±29.2	/	/	1.00±0.00	(1.0±0.1)×10 <sup>10</sup>
	E	125.9±7.1	5.02±0.09	89.9±1.0	0.37±0.18	(1.7±1.2)×10 <sup>10</sup>	
	2012/02/25	W	485.1±25.9	/	/	0.87±0.00	(1.2±0.1)×10 <sup>10</sup>
2015/01/22	E	91.6±5.6	5.08±0.12	90.3±1.4	≤0.25	≥2.7×10 <sup>9</sup>	
	W	423.9±23.0	/	/	0.90±0.00	(9.3±0.5)×10 <sup>9</sup>	
	E	42.0±3.8	5.00±0.10	90.6±1.1	≤0.33	≥7.0×10 <sup>9</sup>	
2015/03/17	W	579.5±30.2	/	/	0.85±0.00	(1.4±0.1)×10 <sup>10</sup>	
	E	60.1±4.4	5.01±0.10	90.6±1.1	0.42±0.20	(6.0±4.1)×10 <sup>9</sup>	
	2017/02/19	W	491.3±26.1	/	/	0.78±0.00	(1.4±0.1)×10 <sup>10</sup>
2018/04/29	E	42.6±3.9	5.08±0.09	91.8±1.0	≤0.31	≥8.0×10 <sup>9</sup>	
	W	540.3±28.3	/	/	0.75±0.00	(1.7±0.1)×10 <sup>10</sup>	
	E	37.7±3.7	5.07±0.09	90.2±1.0	0.34±0.18	(5.9±4.5)×10 <sup>9</sup>	
J1602+2418	2006/12/18	E	92.4±5.5	/	/	0.55±0.04	(1.4±0.2)×10 <sup>10</sup>
	W	9.1±3.1	7.03±0.13	-68.9±1.7	≤0.81	≥6.3×10 <sup>8</sup>	
	2012/02/08	E	67.2±4.1	/	/	0.89±0.05	(4.2±0.4)×10 <sup>9</sup>
	W	46.8±2.6	7.24±0.15	-63.8±0.1	0.65±0.03	(5.5±0.5)×10 <sup>9</sup>	
	2015/01/22	E	44.4±2.7	/	/	0.45±0.04	(9.8±1.3)×10 <sup>9</sup>
	W	14.7±1.0	7.20±0.11	-64.0±0.2	0.32±0.05	(6.7±1.6)×10 <sup>9</sup>	
2015/03/17	E	72.3±4.1	/	/	0.68±0.04	(7.1±0.7)×10 <sup>9</sup>	
	W	37.2±2.2	7.35±0.19	-63.6±0.2	0.78±0.05	(2.8±0.3)×10 <sup>9</sup>	
	2017/01/16	E	64.1±3.5	/	/	0.73±0.03	(5.4±0.4)×10 <sup>9</sup>
2018/04/29	W	23.9±1.6	7.47±0.14	-63.0±0.2	0.65±0.06	(2.5±0.3)×10 <sup>9</sup>	
	E	71.2±4.5	/	/	0.90±0.04	(4.0±0.4)×10 <sup>9</sup>	
	W	28.1±2.1	7.41±0.12	-64.1±0.2	0.91±0.06	(1.5±0.2)×10 <sup>9</sup>	

**Table G.1.** Continued.

Name	Epoch	Label	$S_{\text{int}}$ (mJy)	R (mas)	PA (°)	$\theta_{\text{FWHM}}$ (mas)	$T_b$ (K)
(1)	(2)	(3)	(4)	(5)	(6)	(7)	(8)
J1815+6127	1994/08/12	NE1	113.8±5.9	/	/	≤0.11	≥2.4×10 <sup>11</sup>
	1995/04/19	NE1	96.9±5.0	/	/	≤0.13	≥1.6×10 <sup>11</sup>
	2014/06/09	JX	15.2±2.1	10.60±0.19	-134.0±0.4	1.16±0.16	(3.2±0.8)×10 <sup>8</sup>
		NE1	98.1±5.1	/	/	0.30±0.02	(2.8±0.3)×10 <sup>10</sup>
		NE2	34.0±2.5	2.58±0.23	70.2±0.7	≤0.32	≥8.6×10 <sup>9</sup>
	2017/01/16	SW1	27.9±3.4	9.03±0.22	-140.9±0.6	1.82±0.18	(2.2±0.4)×10 <sup>8</sup>
		NE1	90.6±5.7	/	/	0.43±0.04	(1.3±0.2)×10 <sup>10</sup>
		NE2	57.3±4.1	2.75±0.16	73.1±0.6	0.92±0.06	(1.7±0.2)×10 <sup>9</sup>
	2018/03/26	SW1	29.8±3.7	8.77±0.17	-144.0±0.5	1.88±0.16	(2.2±0.4)×10 <sup>8</sup>
		NE1	122.9±8.0	/	/	0.40±0.04	(2.0±0.3)×10 <sup>10</sup>
		NE2	75.9±5.9	2.75±0.13	73.3±0.7	0.95±0.07	(2.2±0.3)×10 <sup>9</sup>
J1823+7938	2018/06/13	SW1	43.8±6.6	8.73±0.14	-143.9±0.6	2.10±0.19	(2.6±0.5)×10 <sup>8</sup>
		NE1	86.6±5.4	/	/	≤0.28	≥2.9×10 <sup>10</sup>
		NE1	87.8±5.0	/	/	≤0.20	≥5.6×10 <sup>10</sup>
	2018/07/30	JX	23.4±3.3	3.08±0.17	75.6±1.3	≤0.44	≥3.1×10 <sup>9</sup>
		JX	12.3±1.8	8.32±0.25	-144.1±0.5	≤0.47	≥1.5×10 <sup>9</sup>
	1997/08/27	E0	272.1±18.4	/	/	0.88±0.06	(7.6±0.9)×10 <sup>9</sup>
		W2	95.7±7.6	15.64±0.22	-116.4±0.1	0.79±0.08	(3.3±0.5)×10 <sup>9</sup>
		E0	226.9±17.8	/	/	0.60±0.04	(1.2±0.2)×10 <sup>10</sup>
	2000/12/04	W2	88.3±8.4	15.73±0.07	-116.0±0.1	0.62±0.05	(4.6±0.7)×10 <sup>9</sup>
		E0	242.9±24.3	/	/	0.56±0.06	(1.5±0.3)×10 <sup>10</sup>
		W2	96.3±9.6	15.71±0.09	-115.9±0.1	0.83±0.06	(2.8±0.4)×10 <sup>9</sup>
J1945+7055	2006/02/23	E0	189.1±10.3	/	/	0.37±0.03	(2.7±0.3)×10 <sup>10</sup>
		W2	70.8±5.9	15.70±0.18	-116.6±0.2	≤0.42	≥8.2×10 <sup>9</sup>
		NE3	101.2±9.2	/	/	≤0.33	≥2.0×10 <sup>10</sup>
	1995/04/19	NE2	19.1±2.2	6.53±0.21	-171.2±1.8	0.57±0.43	(1.3±1.3)×10 <sup>9</sup>
		SW1	32.3±3.1	16.26±0.21	-155.4±0.7	0.88±0.43	(8.9±6.2)×10 <sup>8</sup>
		SW2	12.2±2.2	22.85±0.21	-153.4±0.5	0.87±0.43	(3.4±2.5)×10 <sup>8</sup>
	2014/08/05	NE3	64.0±7.9	/	/	≤0.75	≥2.3×10 <sup>9</sup>
		NE2	22.8±4.3	5.86±0.23	-169.5±2.2	1.47±0.51	(2.1±1.1)×10 <sup>8</sup>
		SW1	46.3±3.3	15.55±0.28	-156.5±1.0	≤0.49	≥3.8×10 <sup>9</sup>
	2017/08/12	SW2	7.1±2.3	23.07±0.29	-154.2±0.7	≤1.30	≥8.4×10 <sup>7</sup>
		NE3	106.3±10.6	/	/	1.09±0.00	(1.8±0.2)×10 <sup>9</sup>
		NE2	35.0±4.5	5.52±0.16	-169.6±1.7	1.11±0.35	(5.7±2.6)×10 <sup>8</sup>
J1945+7055	2018/11/03	SW1	50.1±3.4	15.72±0.15	-155.5±0.5	1.03±0.33	(9.4±4.3)×10 <sup>8</sup>
		SW2	11.7±2.9	23.61±0.15	-153.9±0.4	1.10±0.33	(1.9±0.9)×10 <sup>8</sup>
		NE3	99.9±10.7	/	/	1.16±0.00	(1.5±0.2)×10 <sup>9</sup>
	2018/12/10	NE2	34.5±4.9	5.50±0.16	-171.0±1.7	1.21±0.34	(4.7±2.0)×10 <sup>8</sup>
		SW1	51.3±3.0	15.81±0.16	-156.2±0.6	0.80±0.34	(1.6±1.0)×10 <sup>9</sup>
		SW2	8.9±1.9	23.12±0.16	-153.6±0.4	≤0.64	≥4.4×10 <sup>8</sup>
	2018/12/10	NE3	133.4±14.2	/	/	1.41±0.00	(1.4±0.1)×10 <sup>9</sup>
		NE2	34.5±4.3	5.60±0.16	-170.7±1.6	0.93±0.34	(8.0±4.3)×10 <sup>8</sup>
		SW1	59.5±3.3	15.70±0.16	-156.1±0.6	0.45±0.34	(5.8±6.2)×10 <sup>9</sup>
		SW2	18.7±2.5	23.40±0.16	-153.5±0.4	1.07±0.34	(3.3±1.5)×10 <sup>8</sup>

**Table G.2.** Model-fitting parameters of VLBI components for Fig. B.6

Name	Epoch	Label	$S_{\text{int}}$ (mJy)	$R$ (mas)	PA (°)	$\theta_{\text{FWHM}}$ (mas)	$T_b$ (K)
(1)	(2)	(3)	(4)	(5)	(6)	(7)	(8)
J0003+2129	1996/01/02	C	172.0±8.8	/	/	≤0.12	≥3.0×10 <sup>11</sup>
	1996/03/13	C	187.3±9.4	/	/	≤0.08	≥9.0×10 <sup>11</sup>
	2015/01/23	J2	7.7±1.0	0.79±0.02	-77.8±1.5	≤0.22	≥4.2×10 <sup>9</sup>
		C	105.9±5.3	/	/	0.32±0.00	(2.4±0.1)×10 <sup>10</sup>
		J2	7.8±0.6	2.02±0.03	-67.4±0.9	0.81±0.07	(2.8±0.4)×10 <sup>8</sup>
	2017/05/27	J1	6.3±0.4	3.98±0.02	-74.7±0.3	≤0.26	≥2.1×10 <sup>9</sup>
		C	132.8±6.7	/	/	0.30±0.01	(3.4±0.2)×10 <sup>10</sup>
		J2	10.6±1.1	1.78±0.05	-72.5±1.6	1.15±0.11	(1.9±0.3)×10 <sup>8</sup>
	2018/07/01	J1	7.0±0.5	4.12±0.02	-75.5±0.3	≤0.24	≥2.8×10 <sup>9</sup>
		C	128.1±6.5	/	/	0.31±0.01	(3.1±0.2)×10 <sup>10</sup>
		J2	8.2±1.1	1.61±0.07	-69.6±2.5	0.99±0.14	(2.0±0.5)×10 <sup>8</sup>
J0005+0524	2018/10/23	J1	6.8±0.6	4.15±0.03	-76.3±0.4	≤0.28	≥1.9×10 <sup>9</sup>
		C	144.5±7.3	/	/	0.22±0.01	(9.1±0.7)×10 <sup>10</sup>
		J2	6.8±0.9	1.99±0.08	-60.2±2.3	0.78±0.16	(3.4±1.1)×10 <sup>8</sup>
	2019/07/15	J1	7.5±0.7	4.22±0.04	-72.2±0.5	≤0.36	≥1.8×10 <sup>9</sup>
		C	144.6±7.7	/	/	≤0.17	≥2.7×10 <sup>11</sup>
		J1	9.1±1.7	0.70±0.02	126.3±1.6	2.50±0.04	(7.4±1.4)×10 <sup>7</sup>
	2014/06/09	C	52.2±2.7	/	/	0.30±0.02	(2.7±0.3)×10 <sup>10</sup>
		J1	24.0±1.6	2.14±0.04	100.5±1.1	0.60±0.07	(3.1±0.6)×10 <sup>9</sup>
		C	69.1±3.9	/	/	0.21±0.02	(7.3±1.3)×10 <sup>10</sup>
J1311+1417	2017/07/16	J1	33.6±2.9	2.25±0.04	95.2±1.0	0.86±0.08	(2.1±0.3)×10 <sup>9</sup>
		C	76.5±4.0	/	/	0.32±0.02	(3.5±0.4)×10 <sup>10</sup>
		J1	34.7±2.7	2.29±0.04	95.9±1.0	0.95±0.08	(1.8±0.2)×10 <sup>9</sup>
	2018/09/01	C	75.3±4.0	/	/	0.29±0.02	(4.2±0.4)×10 <sup>10</sup>
		J1	33.3±2.5	2.30±0.03	94.2±0.7	0.93±0.07	(1.8±0.2)×10 <sup>9</sup>
		C	131.4±6.6	/	/	≤0.09	≥8.2×10 <sup>11</sup>
	2014/05/31	C	134.6±7.1	/	/	≤0.15	≥2.8×10 <sup>11</sup>
		J1	10.6±2.0	2.85±0.09	145.6±1.8	≤0.52	≥1.9×10 <sup>9</sup>
		C	79.6±4.6	/	/	≤0.21	≥8.8×10 <sup>10</sup>
J1335+4542	2017/05/27	C0	17.4±2.9	3.02±0.09	31.0±1.7	0.60±0.19	(2.3±1.1)×10 <sup>9</sup>
		J1	74.4±4.2	3.65±0.03	139.6±0.3	0.76±0.03	(6.1±0.5)×10 <sup>9</sup>
		C	80.9±4.9	/	/	0.28±0.04	(4.9±0.9)×10 <sup>10</sup>
	2018/07/27	C0	22.4±2.9	2.69±0.07	29.5±1.5	0.91±0.14	(1.3±0.3)×10 <sup>9</sup>
		J1	81.6±5.0	3.67±0.03	139.4±0.3	0.83±0.04	(5.6±0.5)×10 <sup>9</sup>
		C	57.1±3.7	/	/	≤0.24	≥4.8×10 <sup>10</sup>
	2018/12/10	C0	17.9±2.7	2.83±0.08	29.8±1.6	0.66±0.16	(2.0±0.7)×10 <sup>9</sup>
		J1	57.5±4.0	3.70±0.04	139.4±0.5	0.70±0.06	(5.6±0.7)×10 <sup>9</sup>
		C	79.7±5.0	/	/	0.35±0.04	(3.1±0.5)×10 <sup>10</sup>
	1996/08/10	C0	29.8±3.7	2.66±0.07	29.2±1.5	1.01±0.14	(1.4±0.3)×10 <sup>9</sup>
		J1	85.5±5.5	3.66±0.03	139.6±0.3	0.88±0.05	(5.3±0.5)×10 <sup>9</sup>
		C	229.2±11.6	/	/	0.11±0.01	(1.2±0.1)×10 <sup>12</sup>
J1335+4542	2014/08/05	J3	157.0±7.9	0.56±0.01	-53.1±1.0	0.29±0.00	(1.1±0.1)×10 <sup>11</sup>
		J2	110.4±5.6	1.40±0.01	-64.1±0.4	0.24±0.01	(1.2±0.1)×10 <sup>11</sup>
		J1	58.8±3.1	2.04±0.01	-61.3±0.3	0.77±0.01	(6.1±0.3)×10 <sup>9</sup>
	2017/07/16	JX	540.6±27.0	0.67±0.01	-56.6±0.9	0.22±0.00	(6.2±0.3)×10 <sup>11</sup>
		C	155.6±7.8	/	/	0.38±0.00	(6.0±0.3)×10 <sup>10</sup>
		J2	93.5±4.8	1.66±0.01	-63.0±0.3	0.51±0.01	(2.0±0.1)×10 <sup>10</sup>
	2017/07/16	J1	3.2±0.8	2.93±0.02	-60.8±0.4	≤0.30	≥2.0×10 <sup>9</sup>
		JX	440.5±22.0	0.70±0.01	-54.8±0.8	0.13±0.00	(1.5±0.1)×10 <sup>12</sup>
		J3	106.1±5.3	1.20±0.01	-62.8±0.5	0.34±0.00	(5.1±0.3)×10 <sup>10</sup>
	2017/07/16	C	60.0±3.2	/	/	0.36±0.01	(2.6±0.1)×10 <sup>10</sup>
		J2	56.4±3.2	1.98±0.01	-62.2±0.3	0.55±0.02	(1.0±0.1)×10 <sup>10</sup>

Note that we have avoided here the archival VLBI data of some epochs of bad quality in terms of signal-to-noise ratio and astrometric positions. The components are marked in order of either East to West or North to South direction.

**Table G.2.** Continued.

Name	Epoch	Label	$S_{\text{int}}$ (mJy)	R (mas)	PA (°)	$\theta_{\text{FWHM}}$ (mas)	$T_b$ (K)
(1)	(2)	(3)	(4)	(5)	(6)	(7)	(8)
J2022+6136	2018/07/24	J3	503.4±25.3	0.92±0.01	-59.8±0.6	0.38±0.01	(2.5±0.1)×10 <sup>11</sup>
		JX	107.9±5.7	1.85±0.01	-65.4±0.3	0.89±0.02	(9.9±0.6)×10 <sup>9</sup>
		C	20.4±1.6	/	/	≤0.16	≥5.7×10 <sup>10</sup>
	2018/08/10	JX	351.5±17.6	0.63±0.01	-59.1±0.9	≤0.03	≥1.8×10 <sup>13</sup>
		J3	74.5±3.7	1.10±0.01	-68.9±0.5	0.14±0.00	(2.1±0.1)×10 <sup>11</sup>
		C	42.0±2.2	/	/	0.34±0.00	(2.0±0.1)×10 <sup>10</sup>
	1994/08/12	J2	48.2±2.5	1.85±0.01	-65.1±0.3	0.53±0.01	(9.6±0.5)×10 <sup>9</sup>
		C	1415.0±71.3	/	/	0.29±0.01	(3.7±0.2)×10 <sup>11</sup>
		J2	521.9±27.8	0.51±0.01	42.0±1.1	0.68±0.01	(2.5±0.1)×10 <sup>10</sup>
J2245+0324	1995/04/19	J3	759.0±40.4	7.04±0.01	33.3±0.1	0.61±0.02	(4.4±0.3)×10 <sup>10</sup>
		C	1802.8±93.7	/	/	0.40±0.01	(2.4±0.2)×10 <sup>11</sup>
		JX	179.3±19.8	1.73±0.04	34.4±1.3	1.12±0.08	(3.1±0.5)×10 <sup>9</sup>
	1999/12/20	J3	754.4±41.6	6.99±0.01	33.3±0.1	0.53±0.02	(5.8±0.5)×10 <sup>10</sup>
		C	1347.7±69.5	/	/	0.39±0.01	(1.8±0.1)×10 <sup>11</sup>
		J2	329.8±21.0	0.64±0.01	33.0±0.9	0.54±0.02	(2.3±0.2)×10 <sup>10</sup>
	2002/03/06	J3	557.0±30.7	7.05±0.01	33.3±0.1	0.61±0.01	(3.0±0.2)×10 <sup>10</sup>
		C	1643.1±83.3	/	/	0.46±0.01	(1.6±0.1)×10 <sup>11</sup>
		J2	344.6±21.4	0.70±0.01	26.9±0.8	0.45±0.02	(3.4±0.3)×10 <sup>10</sup>
J2245+0324	2010/08/10	J3	655.9±34.0	7.04±0.01	33.1±0.1	0.61±0.01	(3.6±0.2)×10 <sup>10</sup>
		C	1628.2±87.4	/	/	0.48±0.02	(1.4±0.1)×10 <sup>11</sup>
		J2	218.1±25.6	2.61±0.05	33.8±1.1	0.54±0.11	(1.5±0.5)×10 <sup>10</sup>
	2010/12/05	J3	497.1±27.2	6.94±0.01	33.4±0.1	0.40±0.02	(6.3±0.6)×10 <sup>10</sup>
		C	732.0±38.5	/	/	≤0.22	≥3.1×10 <sup>11</sup>
		J2	41.8±15.8	2.59±0.30	46.7±6.6	≤1.17	≥6.3×10 <sup>8</sup>
	2011/01/21	J3	220.4±23.8	6.83±0.07	34.2±0.6	≤0.53	≥1.6×10 <sup>10</sup>
		C	1683.0±90.0	/	/	0.60±0.02	(9.9±0.8)×10 <sup>10</sup>
		J2	271.5±28.3	2.26±0.07	34.5±1.8	1.24±0.13	(3.7±0.7)×10 <sup>9</sup>
J2245+0324	2012/02/08	J3	541.8±28.9	6.92±0.01	34.1±0.1	0.62±0.02	(3.0±0.2)×10 <sup>10</sup>
		C	1830.9±93.1	/	/	0.53±0.01	(1.4±0.1)×10 <sup>11</sup>
		J2	289.0±20.8	2.35±0.03	32.4±0.7	0.43±0.06	(3.3±0.7)×10 <sup>10</sup>
	2013/05/07	J3	578.0±30.0	6.98±0.01	33.4±0.1	0.63±0.02	(3.1±0.2)×10 <sup>10</sup>
		C	1774.2±91.2	/	/	0.47±0.02	(2.1±0.1)×10 <sup>11</sup>
		J2	279.8±17.5	2.19±0.02	33.8±0.5	0.32±0.04	(7.1±1.4)×10 <sup>10</sup>
	2015/06/12	J3	631.9±32.4	6.96±0.01	33.7±0.1	0.57±0.02	(5.0±0.3)×10 <sup>10</sup>
		C	1195.6±61.9	/	/	0.33±0.02	(2.8±0.3)×10 <sup>11</sup>
		J2	139.0±13.8	1.82±0.06	38.9±1.9	≤0.44	≥1.8×10 <sup>10</sup>
J2245+0324	2015/08/24	J3	425.5±26.2	6.98±0.02	33.2±0.2	0.37±0.05	(8.1±1.6)×10 <sup>10</sup>
		C	1385.4±70.9	/	/	0.63±0.02	(9.0±0.6)×10 <sup>10</sup>
		J2	251.3±17.6	2.02±0.03	32.1±0.9	0.86±0.07	(8.8±1.2)×10 <sup>9</sup>
	2016/01/29	J3	487.6±24.6	7.00±0.01	33.6±0.1	0.66±0.01	(2.9±0.2)×10 <sup>10</sup>
		C	1354.5±70.9	/	/	0.43±0.02	(1.9±0.1)×10 <sup>11</sup>
		J2	217.0±19.4	2.32±0.04	33.0±1.0	≤0.34	≥4.9×10 <sup>10</sup>
	2016/06/27	J3	455.3±24.2	6.99±0.01	33.7±0.1	0.52±0.02	(4.4±0.3)×10 <sup>10</sup>
		C	1009.7±54.2	/	/	0.42±0.04	(1.5±0.2)×10 <sup>11</sup>
		J2	161.9±17.0	2.09±0.09	33.5±2.5	≤0.67	≥9.4×10 <sup>9</sup>
J2245+0324	2016/08/07	J3	170.3±23.0	6.84±0.12	35.8±1.0	≤0.78	≥7.3×10 <sup>9</sup>
		C	1303.6±66.4	/	/	0.59±0.01	(9.7±0.6)×10 <sup>10</sup>
		J2	253.3±15.8	1.95±0.02	35.6±0.6	0.56±0.05	(2.1±0.3)×10 <sup>10</sup>
	1995/07/15	J3	440.7±23.1	7.01±0.01	33.9±0.1	0.58±0.02	(3.4±0.2)×10 <sup>10</sup>
		C	436.7±21.9	/	/	0.23±0.00	(3.4±0.2)×10 <sup>11</sup>
		J1	107.1±5.7	4.51±0.01	42.7±0.1	0.56±0.02	(1.4±0.1)×10 <sup>10</sup>
J2245+0324	2015/01/23	C	168.5±8.6	/	/	0.33±0.01	(5.9±0.4)×10 <sup>10</sup>
		J1	58.4±3.1	4.70±0.01	39.6±0.1	0.46±0.02	(1.0±0.1)×10 <sup>10</sup>
		JX	5.9±1.7	5.41±0.19	-135.7±2.0	1.14±0.38	(1.7±0.9)×10 <sup>8</sup>
	2017/09/18	C	213.0±10.8	/	/	0.25±0.02	(1.3±0.1)×10 <sup>11</sup>
		J1	60.1±3.9	4.73±0.05	41.2±0.6	0.81±0.10	(3.5±0.6)×10 <sup>9</sup>
		JX	10.6±1.5	4.98±0.14	-133.0±1.6	≤0.92	≥4.8×10 <sup>8</sup>
J2245+0324	2018/11/18	C	163.5±8.3	/	/	0.18±0.01	At(1.9±0.2)×10 <sup>11</sup> page 39 of 40
		JX	25.5±1.8	0.61±0.01	76.3±0.9	≤0.17	≥3.3×10 <sup>10</sup>
		J1	73.0±4.3	4.78±0.02	40.4±0.2	0.68±0.04	(6.0±0.6)×10 <sup>9</sup>
	2018/11/18	JX	25.5±1.8	0.61±0.01	76.3±0.9	≤0.17	≥2.4×10 <sup>8</sup>

**Table G.2.** Continued.

Name (1)	Epoch (2)	Label (3)	$S_{\text{int}}$ (mJy) (4)	$R$ (mas) (5)	PA ( $^{\circ}$ ) (6)	$\theta_{\text{FWHM}}$ (mas) (7)	$T_b$ (K) (8)
J2245+0324	1995/07/15	C	436.7 $\pm$ 21.9	/	/	0.23 $\pm$ 0.00	(3.4 $\pm$ 0.2) $\times$ 10 <sup>11</sup>
		NE	107.1 $\pm$ 5.7	4.51 $\pm$ 0.17	42.7 $\pm$ 0.1	0.56 $\pm$ 0.02	(1.4 $\pm$ 0.1) $\times$ 10 <sup>10</sup>
	2015/01/23	C	168.5 $\pm$ 8.6	/	/	0.33 $\pm$ 0.01	(5.9 $\pm$ 0.4) $\times$ 10 <sup>10</sup>
		NE	58.4 $\pm$ 3.1	4.70 $\pm$ 0.18	39.6 $\pm$ 0.1	0.46 $\pm$ 0.02	(1.0 $\pm$ 0.1) $\times$ 10 <sup>10</sup>
		SW	5.9 $\pm$ 1.7	5.41 $\pm$ 0.17	-135.7 $\pm$ 2.0	1.14 $\pm$ 0.37	(1.7 $\pm$ 0.9) $\times$ 10 <sup>8</sup>
		C	213.0 $\pm$ 10.8	/	/	0.25 $\pm$ 0.02	(1.3 $\pm$ 0.1) $\times$ 10 <sup>11</sup>
	2017/09/18	NE	60.1 $\pm$ 3.9	4.73 $\pm$ 0.36	41.2 $\pm$ 0.6	0.81 $\pm$ 0.10	(3.5 $\pm$ 0.6) $\times$ 10 <sup>9</sup>
		SW	10.6 $\pm$ 1.5	4.98 $\pm$ 0.32	-133.0 $\pm$ 1.6	$\leq$ 0.92	$\geq$ 4.8 $\times$ 10 <sup>8</sup>
		C	163.5 $\pm$ 8.3	/	/	0.18 $\pm$ 0.01	(1.9 $\pm$ 0.2) $\times$ 10 <sup>11</sup>
	2018/11/18	JX	25.5 $\pm$ 1.8	0.61 $\pm$ 0.11	76.3 $\pm$ 1.0	$\leq$ 0.17	$\geq$ 3.3 $\times$ 10 <sup>10</sup>
		NE	73.0 $\pm$ 4.3	4.78 $\pm$ 0.19	40.4 $\pm$ 0.2	0.68 $\pm$ 0.04	(6.0 $\pm$ 0.6) $\times$ 10 <sup>9</sup>
		SW	2.5 $\pm$ 0.7	5.73 $\pm$ 0.17	-128.0 $\pm$ 1.3	$\leq$ 0.63	$\geq$ 2.4 $\times$ 10 <sup>8</sup>